DEPENDENCE OF THE NORMALIZED RADAR CROSS SECTION OF OCEAN WAVES ON BRAGG WAVELENGTH–WIND SPEED AND DIRECTION SENSITIVITY

A Thesis

Submitted to the

Department of Electrical and Computer Engineering

Brigham Young University

In Partial Fulfillment

of the Requirements for the Degree

Master of Science

by

R. Scott Collyer

September 29, 1994

DEPENDENCE OF THE NORMALIZED RADAR CROSS SECTION OF OCEAN WAVES ON BRAGG WAVELENGTH–WIND SPEED AND DIRECTION SENSITIVITY
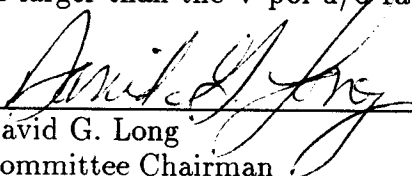
R. Scott Collyer

Department of Electrical and Computer Engineering

M. S. Degree, October 1994

ABSTRACT

An ultra-wideband scatterometer, Y-Scat, was deployed on the Canada Centre for Inland Waters (CCIW) Research Tower located at Lake Ontario. While measurements of the normalized radar cross section (σ^o) of sea waves at at a variety of frequencies and incidence angles were collected, only frequencies of 2.0, 3.05, 5.30, 10.02, and 14.0 GHz, and 30°, 40°, and 50° incidence angles were analyzed. The measurements were binned according to relative azimuth (in 20° increments) and wind speed. Only measurements corresponding to upwind or downwind and wind speeds greater than 4.5 m/s were used. From these data, the sensitivity of σ^o to both wind speed and direction as a function of Bragg wavelength was investigated. Adopting a power law model to describe the relationship between σ^o and wind speed, both wind speed exponents and upwind/downwind (u/d) ratios of σ^o were found using least squares linear regression. The analysis of the wind speed exponents and u/d ratios showed that shorter Bragg wavelengths ($\Lambda < 4cm$) are most sensitive to wind speed and direction. Additionally, vertical polarization (V-pol) σ^o was shown to be more sensitive to wind speed than horizontal polarization (H-pol) σ^o, while the H-pol u/d ratio was larger than the V-pol u/d ratio.
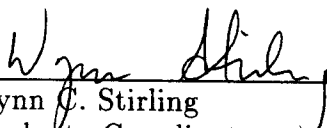
COMMITTEE APPROVAL:

David G. Long
Committee Chairman

David V. Arnold
Committee Member

Wynn C. Stirling
Graduate Coordinator

ACKNOWLEDGMENTS

CONTENTS

LIST OF TABLES

LIST OF FIGURES

CHAPTER 1

INTRODUCTION

For years meteorologists have relied on weather prediction models to make forecasts. In general, these models require initial values of various environmental parameters including wind speed and direction [1, 2]. The results of the weather prediction models are heavily dependent upon the accuracy of the initial parameters. To obtain initial values of winds both ship measurements and data buoys are used. Ship measurements, however, suffer from poor quality and, although data buoys are very accurate, obtaining global coverage with buoys is not feasible [2]. Currently, spaceborne scatterometers offer the best solution to the problem of obtaining accurate global wind measurements.

Scatterometers are active microwave radars that transmit a radar pulse towards a target and then measure the energy reflected or scattered back to the sensor. The scattered power measurements are converted into a parameter called the normalized radar cross section (σ^o). For the water surface, σ^o is a function of both wind speed and direction. Given scattered power measurements at several azimuth angles, it is possible to infer the corresponding wind vector [3]. Geophysical model functions attempt to describe the relationship between wind vectors and backscatter. A variety of model functions have been proposed. Some are based solely on empirical data, while others use a combination of theory and empiricism. However, none of the model functions have been able to completely describe the relationship between wind vectors and backscatter.

The first scatterometer capable of global coverage was onboard Seasat, a remote sensing satellite launched by NASA in 1978. Because of a power failure Seasat was only in operation for three months, but in that short time it provided researchers with a valuable data set to both develop and test the concept of scatterometer anemometry. The Seasat data demonstrated the possibility of obtaining global wind measurements with scatterometers. However, it also pointed out deficiencies in the understanding of complex air-sea interactions which affect microwave backscatter from the ocean surface.

1

To increase understanding of the air-sea interface and determine which parameters affect radar returns off the sea surface, various scatterometer experiments have been conducted including airplane circle flights, ocean platform, and water wave tank experiments. Nearly all the scatterometers have operated at Ku-band (14 Ghz), C-band (5 Ghz), or X-band (10 Ghz) microwave frequencies [4, 5, 6, 7, 8, 9]. Some experiments have also been conducted at L-band (1-2 GHz) and Ka-band (35 GHz) [10, 11]. Therefore, scatterometer measurements exist over a wide range of frequencies. However, since the experiments were conducted at different locations, with different radar systems, and most likely used different environmental parameter measurement schemes, it is difficult to use these previous experimental results to thoroughly understand the relationship between microwave frequency and radar backscatter.

The Microwave Earth Remote Sensing (MERS) group at Brigham Young University has developed and built an ultra-wide band scatterometer called Y-Scat. Y-Scat has the unique ability to be operated at any frequency from 2-18 GHz, and can make measurements at a variety of incidence and azimuth angles. This system is currently deployed on the Canada Center for Inland Waters (CCIW)Research Tower at Lake Ontario [12, 13]. The multi-frequency capability of Y-Scat provides an excellent opportunity to study the dependence of σ^o on frequency at different incidence angles. In addition, accurate in-situ weather data are available. Y-Scat is intended to be deployed for approximately 6 months. The length of the deployment will provide a large data set for model function studies since measurements will be taken during a variety of environmental conditions.

This thesis studies the dependence of σ^o on frequency and incidence angle. In addition, the sensitivity of σ^o to wind speed and direction is investigated. Approximately 3 months of Y-Scat data, all that is currently available, are analyzed in this research. The research presented here is not an attempt to develop a new model function or to provide extensive theoretical justifications of the frequency dependence of σ^o. Instead, it is a careful and comprehensive analysis of empirical results. Conclusions regarding the characteristics of σ^o are based on these empirical results and compared to results found by other researchers. The main contributions of my research are:

1. Development, optimization, and deployment of the Y-Scat radar system.

2. Generation of a reliable edited data set.

3. Empirical observations of the sensitivity of σ^o to wind speed and direction at multiple frequencies and incidence angles.

4. Careful analysis of the behavior of σ^o as a function of Bragg wavelength.

5. Conclusions regarding an "optimum" operational frequency of a scatterometer system based on Bragg wavelength analysis.

The remainder of this thesis is organized as follows: Chapter 2 contains a brief description of relevant ocean scattering principles. Chapter 3 discusses the experiment deployment, while Chapter 4 explains the data analysis techniques used in this research, and Chapter 5 presents and discusses the results of the data analysis. Lastly, Chapter 6 contains conclusions and suggestions for further research.

CHAPTER 2

BACKGROUND

2.1 Introduction

As mentioned in the previous chapter, scatterometers transmit electro-magnetic energy and measure the amount of power scattered off the surface. At microwave frequencies, sea surface scattering is dependent on small scale (1-15 cm) gravity/capillary waves. These waves are generated through energy input from the wind. The amount of coupling between the wind field and waves is defined by the drag coefficient (C_{DN}). Normalized by wind speed at some reference height (e.g. 10 m), the drag coefficent can be defined in terms of wind friction velocity, where the friction velocity describes the momentum transfer between the wind and waves. The complete specification of the momentum transfer between the surface wind and ocean waves and the EM scattering from these waves is a very complex problem. The background presented here is not meant to be a detailed discussion of these interactions, but rather, it is intended to familiarize the reader with terminology and basic scattering principles used in this research.

The first section will discuss the normalized radar cross section (σ^o). The next section describes Bragg scattering, while the third section explains power law model functions. Finally, the last section examines previous experiments which are relevant to this research.

2.2 Normalized Radar Cross Section

The manner in which an incident EM wave scatters off an object is a function of both the object's geometry and its material properties (i.e., dielectric constant and conductivity). The scattering properties of an object can be characterized by the object's radar cross section. The radar cross section of an object is defined as the equivalent area intercepting an amount of power that, when scattered isotropically, produces at the receiver a power density that is equal to the density scattered by the actual target [14]. The normalized radar cross section

4

(σ^o) is equal to the radar cross section divided by the effective target area, and is therefore unitless. In ocean scatterometery, the normalized radar cross section varies several orders of magnitude and as a result is usually expressed in decibels. All σ^o values in this study are given in dB.

The normalized radar cross section is related to the amount of received power by the well known radar equation

$$P_r = \int_A \int \frac{P_t(\theta,\phi)G_t(\theta,\phi)G_r(\theta,\phi)\sigma^o(\theta,\phi)\lambda^2}{(4\pi)^3 R^4(\theta,\phi)} dA \qquad (2.1)$$

where P_r is the received power, G_t and G_r are the transmitter and receiver gains, λ is the EM wavelength, and R is the distance to the target. Notice that the integral is done over the area of the antenna pattern. As shown by Reed (R. Reed, Calibration Report Draft-July, 1994), using the mean value theorem of calculus, the above formula can be simplified to the following form

$$P_r = \frac{K_{sys}\sigma^o 4\pi A_{eff}}{(4\pi r^2)^2} \qquad (2.2)$$

where A_{eff} is the effective target area, r is the mean distance to the target, and K_{sys} is given by

$$K_{sys} = \frac{P_t(G_r G_t)_{peak}\lambda^2}{(4\pi)^2}. \qquad (2.3)$$

The appropriate values of K_{sys} and A_{eff} at a given frequency and polarization are determined from radar calibration. For calibration, power measurements are made using a target of known cross section at a variety of elevation and azimuth angles. Y-Scat was calibrated at the BYU antenna range using a 4 inch diameter aluminum sphere, which was mounted on a pivot arm driven by a small motor. The pivot arm was mounted on a moveable tower so that calibration could be accomplished at different range distances.

The accuracy of σ^o depends on both the radar system and calibration procedures used. However, the change in σ^o as a function of wind speed at a given frequency and polarization depends only on the radar measurements and is independent of calibration accuracy. Therefore, the Y-Scat calibration does not affect the results and further discussion of the calibration procedures is not included here.

2.3 Bragg Scattering

The primary scattering mechanisms off the sea surface vary according to the incidence angle of the transmitted radar pulse. At near nadir ($0°$ - $20°$) the scatter, termed quasi-specular, is caused by direct reflections. Quasi-specular scattering decreases with increasing wind speed and surface roughness. For moderate incidence angles ($20°$ - $60°$) the predominant scattering mechanism is Bragg scatter. At larger incidence (grazing) angles, breaking waves and wedge scattering are dominant. This study only considers moderate incidence angles or Bragg scattering.

In Bragg scattering theory, the random sea surface is decomposed into its spectral components, and the backscatter return is assumed to be caused from the component which is in resonance with the incident radiation (see Fig. 2.1). In first order Bragg theory, the ocean wavelengths are related to electromagnetic
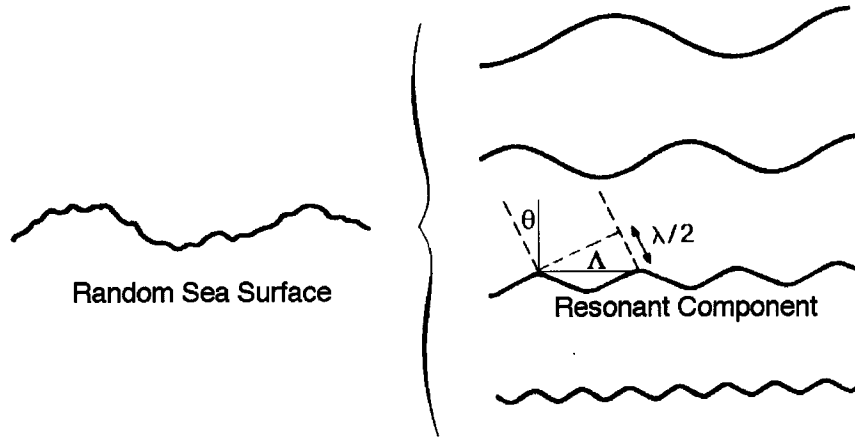
Figure 2.1: Decomposition of a wave into its spectral components.

wavelengths by the following equation

$$\Lambda = \frac{\lambda}{2\sin(\theta)} \qquad (2.4)$$

where Λ is the Bragg wavelength, λ is the EM wavelength, and θ is the incidence angle. For microwave frequencies of 2 - 18 GHz, and moderate incidence angles, the Bragg wavelengths vary from approximately 1 cm to 20 cm, which includes

capillary and short gravity waves. In the Bragg scattering regime σ^o is given by [15]

$$\sigma^{\circ}(\theta) = 16\pi k^4 \cos^4(\theta) |g_{ii}| \Psi(2k\sin(\theta), 0) \tag{2.5}$$

where k is the electromagnetic wave number, Ψ is the two dimensional ocean wavenumber spectrum, and θ is the incidence angle. The $|g_{ii}|$ coefficients depend on polarization and are

$$g_{HH} = \frac{\epsilon_r - 1}{[\cos(\theta) + (\epsilon_r - \sin(\theta))^{1/2}]^2} \tag{2.6}$$

$$g_{VV} = (\epsilon_r - 1)\frac{\epsilon_r(1 + \sin(\theta))^2 - \sin^2(\theta)}{[\epsilon_r \cos(\theta) + (\epsilon_r - \sin(\theta))^{1/2}]^2} \tag{2.7}$$

where ϵ_r is the relative permittivity of sea water. The subscripts (HH, VV) refer to the transmit and receive polarization, respectively.

On the ocean's surface small scale (capillary/small gravity) waves. are tilted by larger gravity waves. To account for the tilting effect on σ^o, a quasi-specular term, which is dependent on the mean squared slope of the surface. is added to equation 2.5. The backscatter power increases when the Bragg waves are tilted towards the radar. As the Bragg waves are tilted away from the radar. the backscatter power decreases. However, the increase in power is higher than the corresponding decrease. This modulation of σ^o by large gravity waves is described by the modulation transfer function [10].

2.4 Model Functions

As mentioned in the introduction, geophysical model functions relate backscatter power (σ^o) to wind vectors. σ^o is a function of polarization (p), EM frequency (f), incidence angle (θ), relative azimuth angle, and wind speed (U). The relative azimuth angle (χ) is defined as the difference between the wind direction and radar azimuth angle. A simple model function assumes a power law relationship between σ^o and wind speed (U) (e.g., [12, 16]) or

$$\sigma^{\circ}(f, \theta, \chi, p) = A(f, \theta, \chi, p)U^{\gamma(f, \theta, \chi, p)}. \tag{2.8}$$

In this equation A is some constant and γ is referred as to as the wind exponent where the γ function arguments (f, θ, χ, p) emphasize that this relationship depends on frequency, incidence angle, relative azimuth angle, and polarization. The

wind exponent gives a measure of how sensitive σ^o is to wind speed.

A power law model was used to analyze Seasat data and gave reasonable results [17]. However, since then researchers [18, 19] have questioned the validity of this simple model. There is no theoretical justification of this model; however it reasonably describes experimental results. The power law form does not hold at all wind speeds, as σ^o falls off more rapidly for low wind speeds and may saturate or even decrease at high wind speeds. However, for midrange wind speeds (5 - 16 m/s) experiments have shown good agreement with the power law model [8, 18]. While additional model functions, based on principles of ocean scattering and hydrodynamics exist [18, 20, 21], this thesis only considers mid-range wind speeds, and therefore a power law model is adequate for this study.

Previous experiments have shown that σ^o varies with relative azimuth as approximately $\cos(2\chi)$. The azimuth modulation can be included as [16]

$$\sigma^o = A_0 + A_1 \cos(\chi) + A_2 \cos(2\chi). \qquad (2.9)$$

The coefficients A_0, A_1, A_2 are power law relationships with wind speed. This model predicts both wind speed and wind direction. Note that this model demonstrates a small asymmetry between the value of σ^o at upwind ($\chi = 0°$) and downwind ($\chi = 180°$) with σ^o at upwind being slightly larger than σ^o at downwind [3]. The difference between σ^o at upwind and downwind (upwind/downwind ratio) is used to remove the 180° directional ambiguity from the wind direction inherent in the wind retrieval problem. Therefore, the upwind/downwind ratio is an important parameter. Since in this study only σ^o values at upwind and downwind are used, the form given in Eq. (2.8) is sufficient.

2.5 Previous Work

Over the past two decades many scatterometer experiments have been conducted by various researchers. However, the emphasis of this study is on the wind speed exponent. There are only a limited number of studies which give numerical values for the wind speed exponent. With this constraint, the following papers are used for comparison: Unal et al. [22], Masako et al. [11], Chaudhry and Moore [4], Feindt et al. [5], and Weissman et al. [9]. A brief description of these experiments is given next.

8

Unal et al. conducted an airplane flight experiment using a dual-pol multi-frequency scatterometer (DUTSCAT). They made σ^o measurements at 1.2, 3.2, 5.3, 13.7, and 17.25 GHz and at 20°, 30°, and 45° incidence angles. They reported values of wind exponents for upwind and upwind/downwind ratios for 10 m/s winds. They also examined differences between V-pol and H-pol σ^o. Their results showed that the wind exponent generally increased with increasing incidence angle and frequency, and that for H-pol the upwind/downwind ratio increased with incidence angle.

Masako et al. [11] used a dual-frequency (10, 34.35 GHz), dual-pol scatterometer mounted on an airplane. In their paper, wind exponents at both upwind and downwind, and upwind/downwind ratios averaged over 3 - 17 m/s are given. Also, they report wind exponents found by other researchers. Masako et al. found that the upwind/downwind ratio was larger for H-pol and suggested that it decreased as a function of increasing wind speed past 7-9 m/s.

Chaudhry and Moore [4] conducted a tower based experiment in conjunction with the HELOSCAT system and obtained measurements at H-pol, Vpol, 10 and 15 GHz. Using an orthogonal regression technique they reported values of wind speed exponents for upwind, downwind, and crosswind over incidence angles (θ) from 20° to 70°. The found that the wind speed exponent increased rapidly at low incidence angles and varied little for $\theta > 30°$. They calculated the wind exponents for measured winds at 26 m, neutral winds at 19.5 m, and for friction velocity. The results varied slightly between the three cases and they state that neutral winds at 19.5 m gave the best results.

Feindt et al. [5] used an airborne C-band (5.3 GHz) V-pol scatterometer to conduct circle flights over the Atlantic Ocean. They found that wind speed exponents at C-band were typically 20% less than at Ku-band. They also found that the upwind/downwind ratio was typically 30% less at C-band than at Ku-band.

Weissman et al. [9] analyzed data collected by AMSCAT (Ku-band) during the Fasinex experiment. The emphasis of their research was to develop new alogorithims to relate σ^o to both wind speed and wind friction velocity. They reported values of wind speed exponents for both V-pol and H-pol for incidence angles of 30°, 40°, and 50°. They found that wind exponents and their 90%

confidence levels calculated for wind speed at 10 m height were typically higher than those found for friction velocity. The regression against friction velocity resulted in a better data fit than that for wind speed, and as a result they claim that σ^o is more correlated with friction velocity than with wind speed.

2.6 Summary

This chapter has introduced and defined the normalized radar cross section (σ^o) and Bragg scattering. In addition, a power law form of the geophysical model function is described. Lastly, previous scatterometer experiments, which are used for comparison, are briefly described.

CHAPTER 3

EXPERIMENT DEPLOYMENT Y-SCAT 94

3.1 Introduction

Y-Scat was deployed in May 1994 on the CCIW Research Tower located in Lake Ontario (see Fig. 3.1). The deployment, called Y-Scat 94, is scheduled to last until November of this year. The purpose of this experiment is to expand current studies of ocean scattering [23]. The tower location has the advantage of being in well understood conditions. All experimental data presented in this thesis has been obtained during this deployment.

This chapter explains the experimental set-up of Y-Scat 94 and the data collection scheme used. The rest of the chapter contains descriptions of 1) the Y-Scat radar system, 2) the location of the deployment site, 3) the Y-Scat measurement scheme, and 4) the environmental system details.

Figure 3.1: Picture of Y-Scat mounted on the CCIW Research Tower.

3.2 Y-Scat Details

Y-SCAT is an ultra-wideband CW radar that can be operated at any frequency from 2-18 GHz (see Fig. 3.2). It transmits either a V or H polarization signal, with a maximum output power of 23 dBm. The transmit antenna is a
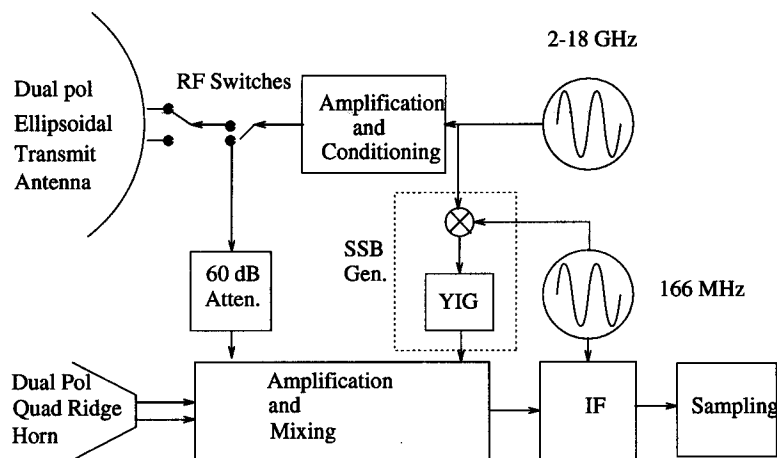
Figure 3.2: Y-Scat block diagram.

specially designed 3 ft ellipsoidal figure antenna which provides a nearly constant beamwidth of 5° from 4 - 18 GHz. At 2 GHz the beamwidth approaches 8°. The receive antenna is a conventional quad-ridge horn with a beamwidth which varies from 45° to 7.5° over the 2-18 GHz frequency range.

The dual-pol receiver simultaneously receives V-pol and H-pol channels. Both channels provide 60 dB gain for the received signals which, after amplification, are mixed down to a 166 MHz IF single side band signal. The IF signal is split into in phase and quadrature (I/Q) components which are mixed down to baseband and then low pass filtered at 900 Hz using a computer-controlled filter. The filter provides up to 60 dB of gain as well as filtering out the returns from stationary targets. The filtered baseband I/Q signals are sampled at 2 kHz via an 8 bit A/D card, and after preprocessing, are stored by a 486 PC. The PC contains a SCSI 1.2 Gbyte hard drive and a 4 mm tape backup system which can hold an additional 2 Gbytes of data.

The main noise in the system, caused by the motor indexers, is injected at the sample and hold board. The motor noise results in a noise floor of approximately -35 dB, while the A/D card has an upper saturation limit of +10 dB.

12

However, the effective SNR of the system can be optimized by adjusting the gain of the programmable filters which are before the sample and hold board.

The incidence and azimuth angles of the antennas are controlled using stepping motors, which are controlled via the 486 PC. Deployed on the tower, the incidence angle can be adjusted from nadir (0°) to greater than 90°. The azimuth angle can be set to +/- 80° from looking straight out from the platform (see Fig. 3.4).

As part of the MERS research group, I was closely involved in developing and testing of the Y-Scat system. Prior to the present deployment, a series of test deployments were conducted at Utah Lake, a freshwater lake in Provo, Utah. The longest of the deployments lasted approximately 2 months. From these test deployments we were able to determine a reliable configuration and measurement scheme which is being used in the current deployment. During the testing period, I was responsible for designing and implementing most of the hardware changes.

3.3 Deployment Location

The CCIW Research Tower is located approximately 1.1 km from the shore near Hamilton Harbor, at the west end of Lake Ontario (see Fig. 3.3). The water depth at the tower location is approximately 12 m. The location provides both long and short fetch wind directions, where the fetch varies from 1 km to 100 km. The long fetch directions are from 50° to 90°T. The fetch is defined as the distance the wind travels over the water surface. Larger waves are generated if the wind blows over a long fetch length than if it blows over a short fetch length. Y-Scat is mounted on the north side of the tower (see Fig. 3.4). Looking straight out from the edge corresponds to 340°. Y-Scat is mounted 6.26 m above the water surface. Shown here for completeness, the X-band radars are being used for another study.

An important aspect of the deployment location is that Lake Ontario is a fresh water lake and the tower is located near the shore. These are both different than the open ocean and as a result the air-sea interactions can expected to be somewhat different as well. To date most significant winds have come from short fetch directions (1-10 km). As a result a significant long wave field is rarely
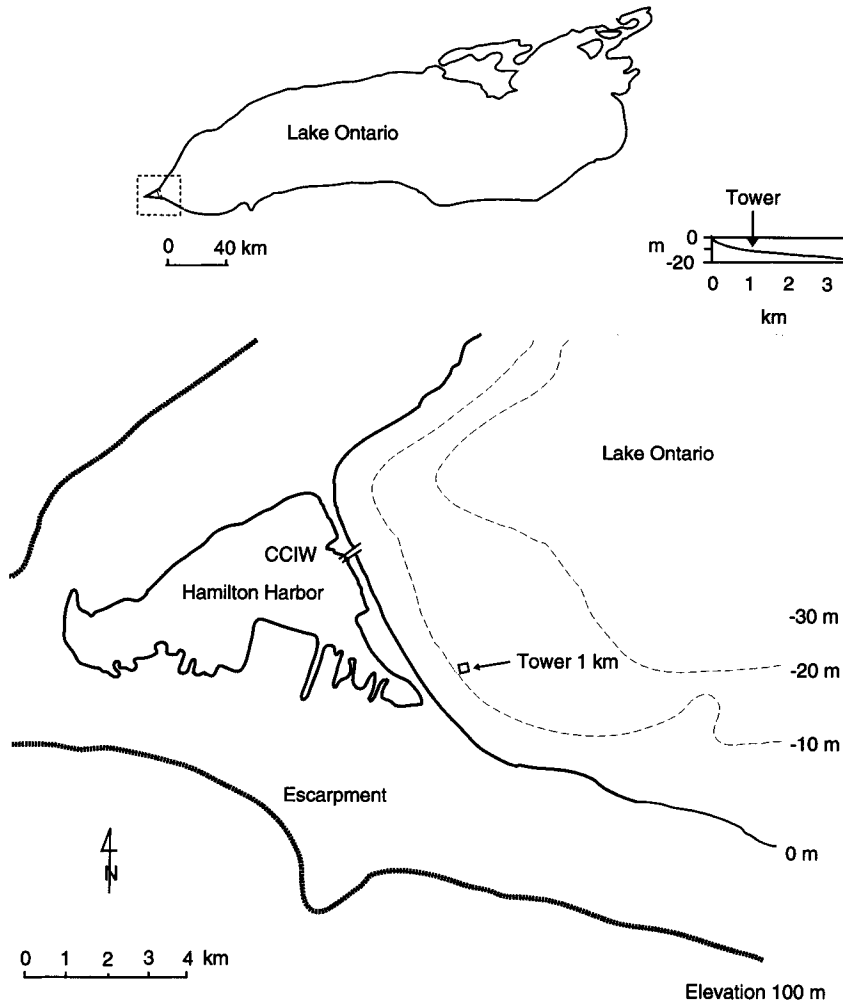
Figure 3.3: Map showing the location of the CCIW Research Tower.

present. For example during the deployment the significant wave height is typically less than 0.5 m, while the maximum significant wave height encountered was 2 m. However, this only occured during two days for which data is available. In the open ocean 2 m wave heights are very common. Therefore, σ^o measurements from Lake Ontario will be different than those on the open ocean with respect to the long wave field.

The wave field on Lake Ontario is typically shorter and steeper than in the open ocean resulting in a higher drag coefficient [12]. For instance, the most commonly used drag coefficient (C_{DN}) for the open ocean is the Large and Pond

model

$$C_{DN} = \begin{cases} 0.114 & U < 10m/s \\ 0.001(0.49 + .065U) & U > 10m/s \end{cases}$$

As shown in [12] the drag coefficient on Lake Ontario is given by

$$C_{DN} = 0.001(0.37 + 0.137U). \tag{3.1}$$

Notice the higher wind speed dependence for the Lake Ontario drag coefficient. This means that for a given wind speed the wind stress (momentum transfer between the wind and the water) over the lake will be higher than that of the ocean. This results in a stronger wind speed sensitivity of σ^o. Therefore, the results obtained from this deployment may be different than those found by other researchers in the open ocean and the results should be interpreted accordingly.
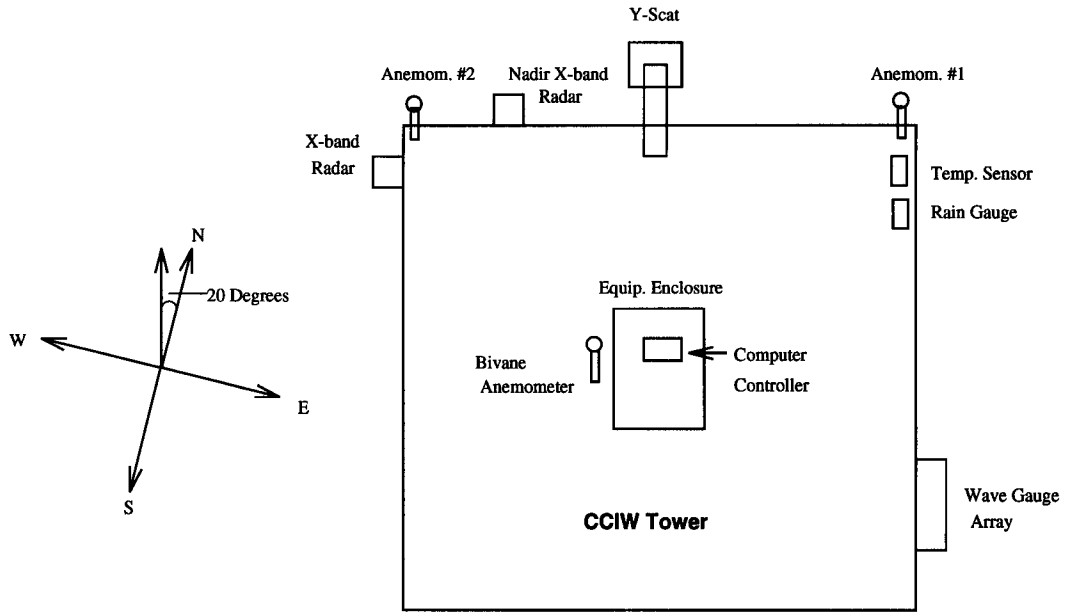
Figure 3.4: Diagram of Y-Scat location on the CCIW Tower.

3.4 Measurement Collection

This thesis is only one of many studies that Y-Scat data is intended to support. Some of these are modulation transfer function, azimuth modulation, near-nadir scattering, and determining the Bragg scattering regimes. As a result, Y-Scat's experiment plan represents a compromise between these various modes.

As stated in the first chapter, a primary objective of this thesis is to investigate the wind speed sensitivity of σ^o as a function of Bragg wavelength. Donlean and Pierson [18] have suggested that short gravity waves ($\lambda < 30cm$) and capillary waves receive energy from the wind. Plant and Keller [24] proposed that waves with wavelengths greater than 10 cm grew primarily by non-linear interactions with shorter waves, rather than from direct wind energy input. With these considerations, it was decided to probe Bragg wavelengths from 1 to 15 cm. Fortunately, these are accessible from the available frequencies and incident angles of Y-Scat. The power measurement methods used and the details of the experiment plan are explained next.

3.4.1 Measuring the Received Power

The received I/Q signals, sampled by the A/D card at 2 kHz over a nominally 1 minute period, constitute the raw data. To conserve on disk storage space, the raw data is processed into 10 Hz, or 0.1 second, measurement records consisting of a power measurement in dB, the Doppler centroid, and the Doppler bandwidth in Hz. The power is calculated by first finding the average of the squares of the individual voltage measurements, and then converting the value to decibels. The Doppler centroids and bandwidths are found using first and second moment estimation techniques (see [25]). Two operational modes are used. The first mode (normal mode) consists of 600 consecutive 0.1 sec measurements for a given polarization, frequency, incidence, and azimuth angle. The second (Doppler mode), takes measurements for 20 minutes at a given polarization, frequency, incidence, and azimuth angle, resulting in 12,000 .1 sec or 4,800 .25 sec[1] measurements. The shortest measurement time is 60 seconds. This length was chosen to allow for at least 10 long waves (assuming a maximum period of 6 seconds) to pass through the measurement area, and thus provide the equivalent of spatial averaging. In addition to the time required to gather actual measurements, time for positioning, calibration, and processing is required, resulting in a maximum of approximately 45 normal measurements per hour.

---

[1]The measurement time was changed from 0.1 sec to 0.25 mid-way through the deployment.

Another important part of each measurement is the internal calibration of the radar. This is accomplished by routing a portion of the transmitted signal through the receive chain and then measuring the power. Each power measurement is accompanied with an internal calibration measurement, and thereby, the RF component drift due to temperature can be accounted for. Each data record contains the elevation angle, azimuth angle, frequency, internal calibration measurement, gain settings of programmable filters, and 600 or 12,000 0.1 second power, centroid, and bandwidth measurements.

3.4.2 Experiment Plan

Recall that the Bragg resonance wavelength (Λ) is a function of both the operating frequency and incidence angle. Since Y-Scat can operate at any frequency between 2-18 GHz and incidence angle between 0°-90°, the 1-15 cm range of Bragg wavelengths can easily be covered. However, two additional considerations are: 1) excessive time required for many measurements, 2) and whether, at a given incidence angle, Bragg scattering can be assumed.

At incident angles from 20-70° Bragg scattering is typically assumed to be the dominant scattering effect [18]. However, it is likely that near 20° part of the scattering will be quasi specular, while near 70° wedge scattering becomes non-negligible [18]. Therefore to avoid these problems, it was decided to use incidence angles from 30° to 50° where Bragg scattering can be safely assumed. Also to compare Y-Scat results with experiments conducted by other researchers, it is desirable to have measurements at C, X, and Ku band. Combining all the constraints it was decided to make power measurements at 2.0, 3.05, 5.30, 10.02, and 14.0 GHz and, at incidence angles of 30°, 40°, and 50°. Table 3.1 shows the resulting range of Bragg wavelengths. Note that this essentially covers the 1-15 cm range desired.

3.5 Environmental System

Y-Scat 94 is equipped with an array of environmental sensors. Some of these include 2 separate anemometers, an aspirated temperature sensor, a humidity gauge and a rain gauge. The data from these sensors are collected and averaged

Bragg Wavelength in cm

Frequency	30°	40°	50°
2.00	15.00	11.67	9.79
3.05	9.84	7.65	6.42
5.30	5.66	4.40	3.69
10.02	3.00	2.33	1.96
14.00	2.14	1.67	1.40

Table 3.1: Bragg Wavelength as a function of frequency and incidence angle.

into 30 second measurements which are then recorded in the radar files. The anemometers are mounted at a height of approximately 10 m above the water surface. Also present on the waves tower are a bivane anemometer to measure wind stress, a water temperature sensor, and wire wavegauge array. From the wire wave gauge array the two dimensional water surface spectrum can be calculated. These sensors are sampled at 10 Hz and stored on a separate 486 PC.

3.6 Summary

In this chapter a description of the Y-Scat system and the deployment location have been given. Since Y-Scat is deployed in a lake, it is suggested that σ^o measurements may be different than those of the open ocean, particularly with respect to the long wave field. This chapter has also described Y-Scat's experiment plan, which is that σ^o measurement are collected at frequencies of 2.0, 3.05, 5.30, 10.02, and 14.0 GHz and at incidence angles of 30°, 40°, and 50°.

CHAPTER 4

DATA ANALYSIS

4.1 Introduction

Since the emphasis of this thesis is on empirical results, the data analysis methods are very critical in interpreting the results. The analysis methods used include standard statistical techniques such as averaging, linear regression and confidence intervals. In addition to statistical methods, determining a valid data set and proper binning of the data are essential. The remainder of this chapter discusses these concepts.

4.2 Data Editing

Approximately 3 months of data, collected from May 6 - August 1st, are analyzed. However, not all the data collected can be used. This occurs because either measurements are not taken at the right incidence and relative azimuth angle, significant rain occurred during the measurements, or the radar exhibited anomalous operation.

4.2.1 Measurement Binning

During the 3 month data set, many different measurements are available during various weather conditions. Figure 4.1 illustrates the wind speeds, directions, and rain rates encountered. Note that the wind blows from all directions, while the wind speed is typically less than 14 m/s. The air and water temperatures and significant wave heights are given in Figure 4.2. The air temperature varies from 10° to 30° C and the water temperature changed from 9° C to a high of approximately 20° C during the deployment. Generally, the significant wave height is less than 0.5 m with the exception of three days. Note that the water temperature and wave gauge sensors are only available after June 15 (Day 44).

To investigate the wind speed sensitivity of σ^o, it is desirable to eliminate other possible weather effects on σ^o. It is well known that σ^o is function of the

19
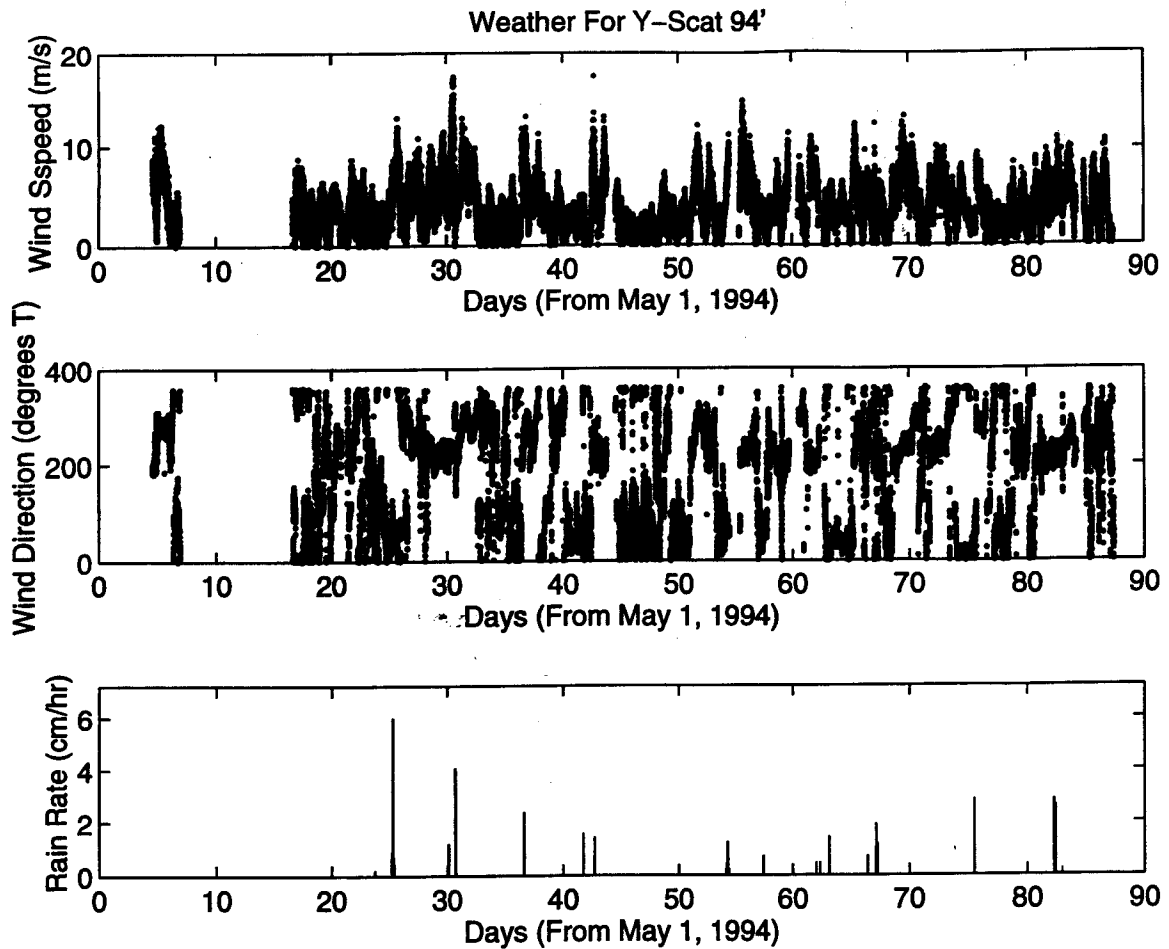
Figure 4.1: Wind speed, direction and rain rate during Y-Scat 94 deployment.

relative azimuth angle between the radar look direction and the wind direction. It has been shown that σ^o varies as $\cos(2\chi)$ [3] with maximums occurring near upwind and downwind (0°, 180°) and minimums near crosswind (90°, 270°). Therefore, the data is binned according to relative azimuth angle in 20° increments. However, only the upwind and downwind bins are used in this analysis. To facilitate this, Y-Scat is always pointed in either upwind or downwind directions if possible. In addition to relative azimuth angle, previous research has suggested that σ^o is also a function of air-sea temperature difference [6, 7], water temperature [18], and long wave field [6]. However, the importance of these affects is still a matter of debate. During the deployment the air-sea temperature difference is always positive or neutral and the long wave field is usually small. Therefore, the current data set does not allow an

adequate comparison between the different cases of air-sea temperature difference and long wave field.

An additional factor to consider is the use of wind speed versus wind friction velocity. Experiments suggest that σ^o is correlated more with wind friction velocity than with wind speed [9]. A bivane anemometer capable of measuring wind stress is deployed on the CCIW tower, but at the present time, the algorithm to convert the bivane voltage measurements to friction velocity is not available. Therefore, the results of this research rely on wind speed measurements. Past experiments have used neutral wind speeds at either 19.5 m or 10 m which are convenient ship board anemometer heights. The anemometers on the CCIW tower are located approximately 10 m above the water surface so that results using wind speed can be compared directly to other experiments using a 10 m reference height.

In summary, all the data are binned according to frequency, incidence angle, and relative azimuth direction. Only data at upwind and downwind are used. Lastly, wind speeds at 10 m are used as the reference for analysis of σ^o versus wind speed.

4.2.2 Effects of Rain on σ^o Measurements

As noted above, significant rain fell during some days of the deployment, while light rain occurred on some others. Rain attenuates the radar signal and also affects the sea surface. Both of these effects can alter the σ^o measurements, potentially contaminating the results. For this study measurements with appreciable effects due to rain are discarded. To identify these measurements, σ^o versus wind speed graphs are generated for data collected during days with and without rain. Then the plots are generated for the same data minus data suspected to be corrupted by rain. The two sets of graphs are then subjectively compared to determine if the rain has a perceptible effect on σ^o.

Figure 4.3 gives an example of 5.3 GHz data collected during times with and without rain. Figure 4.4 shows the corresponding plot for the same time period without data from days with excessive rain. Note from the graphs without the excessive rain, that the remaining points fall within the expected scatter of σ^o. It is expected that the higher frequencies (10, 14 GHz) are more affected by rain
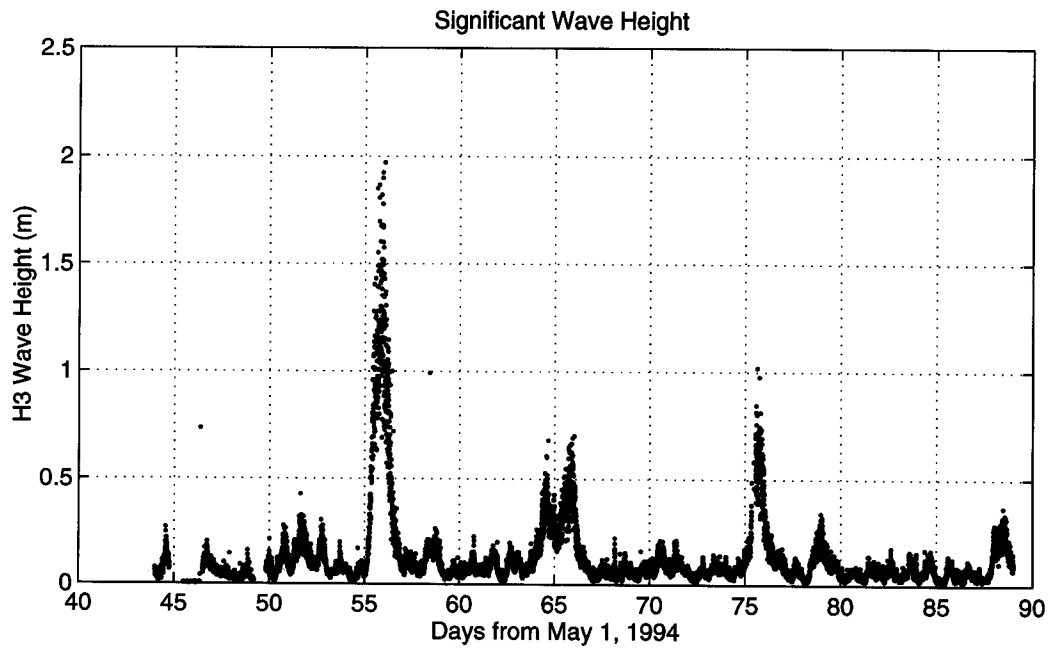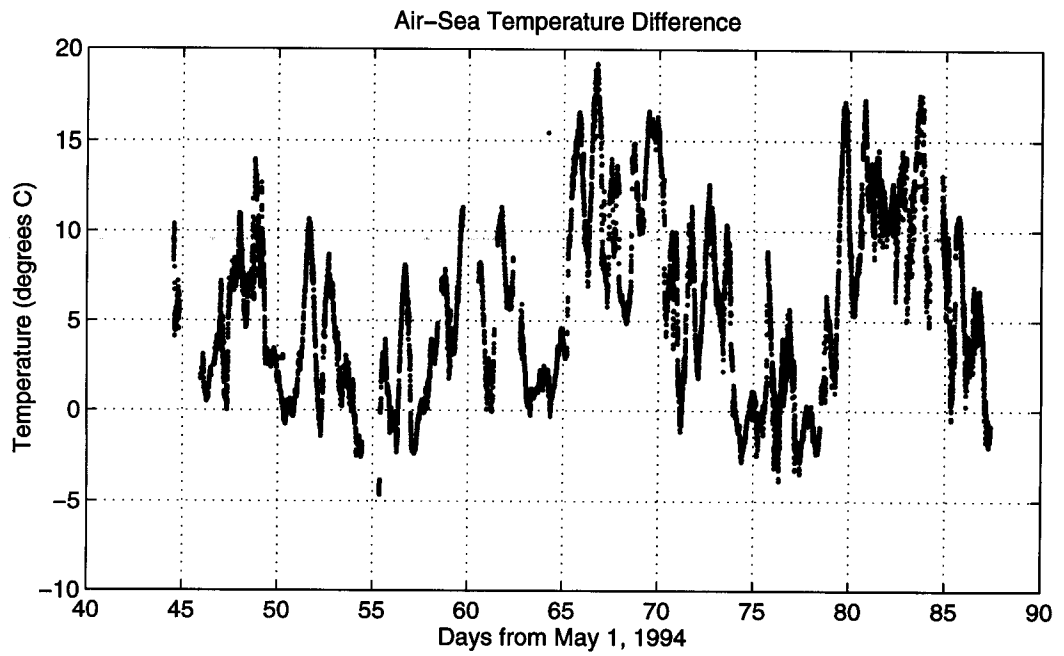
Figure 4.2: Air, water temperature and significant wave height during Y-Scat 94 deployment.

than lower frequencies (2, 3 GHz).

4.2.3 Y-Scat Hardware Anomalies

In addition to measurements corresponding to the wrong measurement bin (i.e., incidence and relative azimuth angle) or rain periods, hardware problems with the Y-Scat instrument reduce the useable data set. Other than power failure, the key problems are saturation and the internal RF power levels.

As mentioned in Chapter 3, programmable filters amplify the received signals by 0 to 60 dB. The gain setting can be different for each measurement and is chosen so that the power level will range from -5 to -10 dB. The appropriate gain is determined by checking the average power of the last measurement at the same frequency and incidence angle. If the power level is below -20 dB the gain is increased 10 dB, and if the power level is above 0 dB the gain is decreased by 10 dB. This dynamic gain control should prevent measurements from being saturated or falling in the noise floor. However, in some instances, the environmental conditions change drastically in between measurements. In an extreme case, the wind speed can increase from 1-2 m/s to 9-10 m/s. As a result, the gain setting determined by the previous measurement may be too high, saturating the receiver. The A/D card saturates at +10 dB, and therefore, the validity of measurements near 10 dB are suspect. To avoid this problem, a +8 dB threshold value is used, and all measurements above this threshold are discarded. Only a very small percentage of the measurements are above this threshold.

During the deployment occasional problems occurred with the RF generator. During a particular measurement mode the YIG filter settings appear to have been wrong. As a result, the RF power levels were attenuated. Primarily 14 GHz measurements were affected, but low levels at all frequencies were observed. In the data analysis, these faulty measurements are flagged by examining the internal calibration value. During normal operation, the internal calibration measurements vary from approximately -2.5 dB at 2 GHz to -6 dB at 14 GHz. A -10 dB threshold value is used to check for anomalous power levels. Measurements with internal calibration power levels below the threshold are discarded.

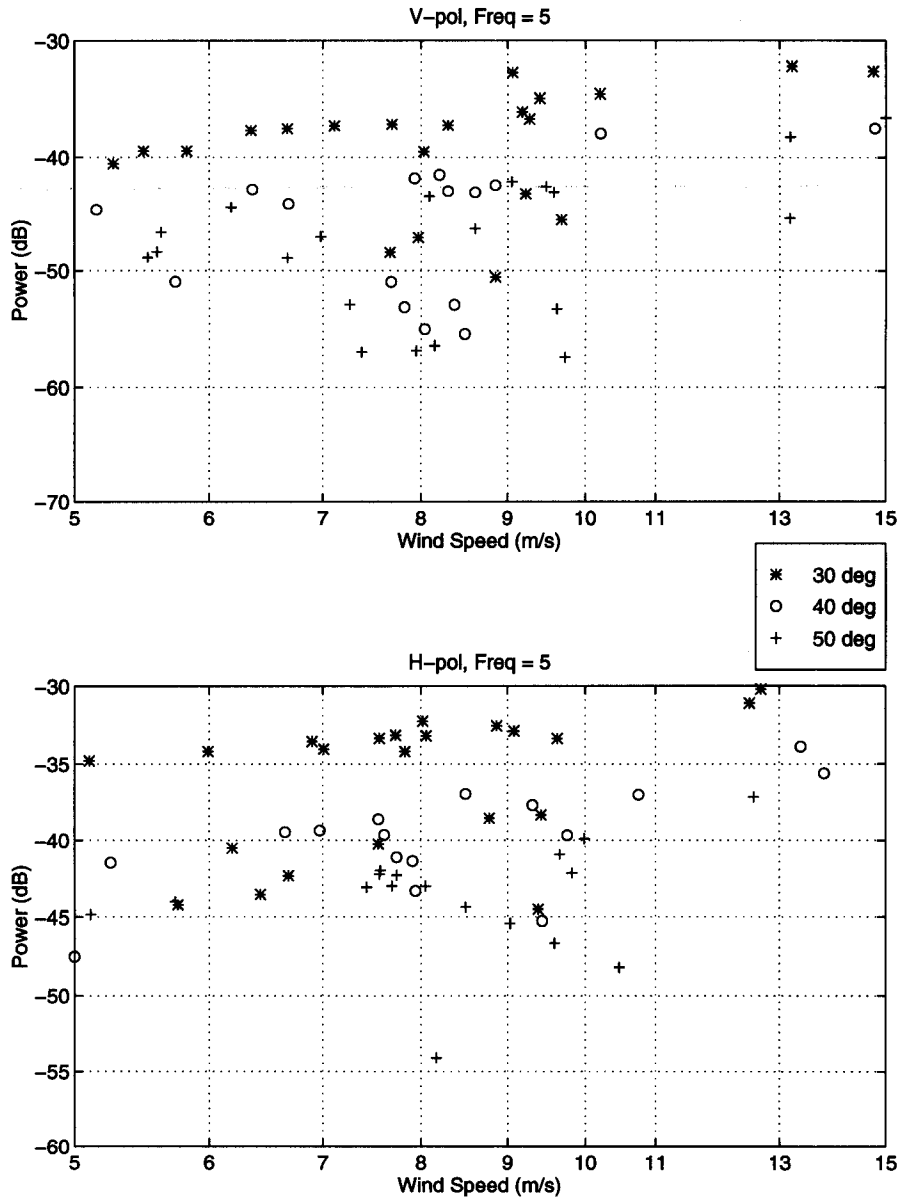Figure 4.3: σ^o versus wind speed (m/s) for all measurements with and without rain at 5.3 GHz. The top plot is for V-pol data, while the bottom plot is for H-pol data.
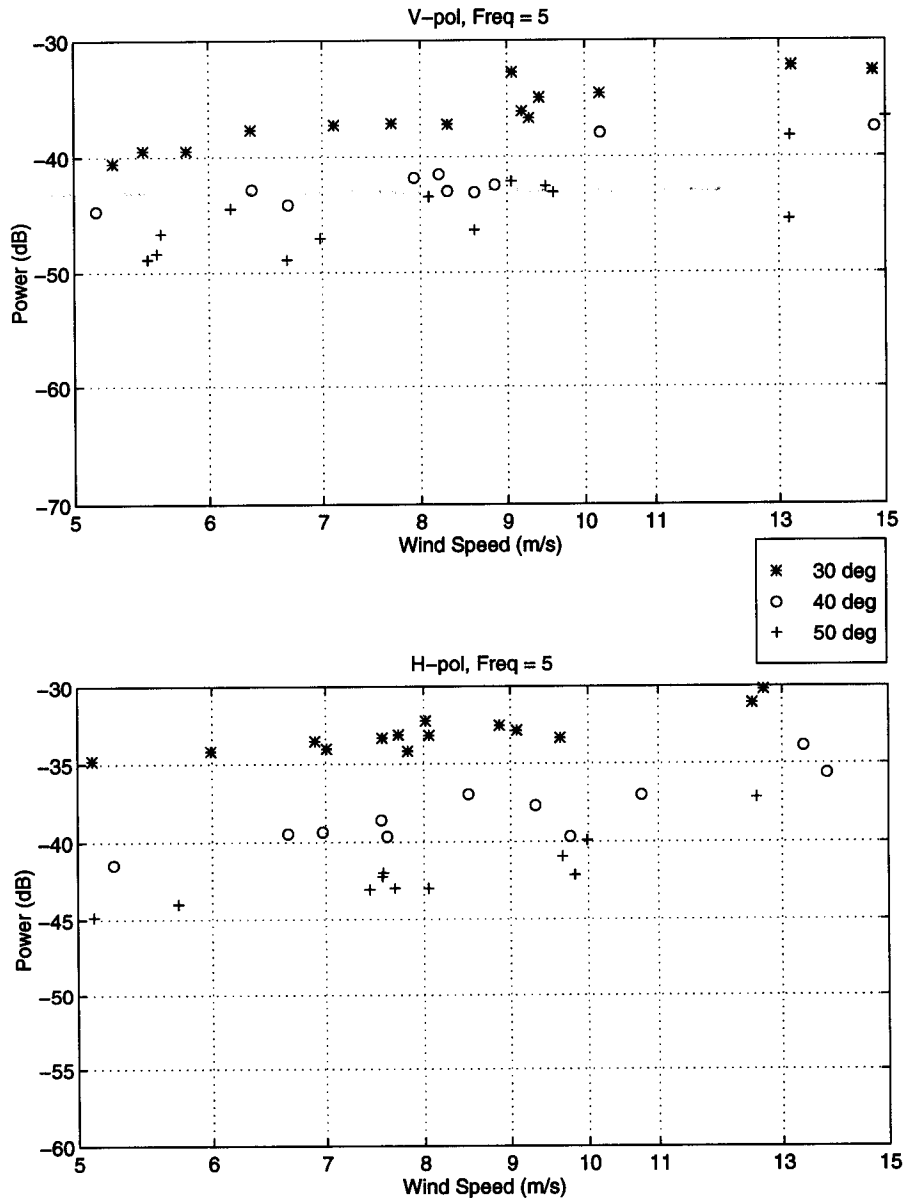
Figure 4.4: σ^o versus wind speed (m/s) for measurements for all points except those occuring during excessive rain at 5.3 GHz. The top plot gives V-pol data and the bottom plot shows H-pol data. Compare this figure to Figure 4.3.

4.2.4 Data Set Summary

The data set is edited both manually and automatically. Manual editing is used to check for data files corrupted by rain, while automatic editing is implemented to throw out saturated and low RF power measurements. The edited data set consists of 21,123 V-pol measurements and 17,516 H-pol measurements. Binning these measurements by relative azimuth angle, using only upwind and downwind, and only keeping measurements corresponding to wind speeds greater than 4.5 m/s reduces the number of V-pol measurements to 3,669 and the H-pol measurements to 2,814.

4.3 Data Analysis

As stated previously two different lengths of measurements are considered. The first consists of 600 .1 second samples. The second measurement length contains either 12,000 .1 sec or 4,800 .25 sec samples. Normal measurements are 60 second records, while the Doppler measurements are 20 minute records. To investigate the sensitivity σ^o at different frequencies, the measurements in each record are averaged and a linear regression fit to the data is performed. Two important considerations for averaging are how many samples should be averaged, and whether they are averaged in log or linear space. For normal measurements, all 600 samples are averaged together to obtain one data point. The Doppler measurements can be averaged into 20 one minute measurements. However, when computing a least squares linear regression, having 20 data points at essentially the same conditions weights the measurement conditions unjustifiably high. Therefore, for Doppler measurements, all samples are averaged into one 20 minute data point. To compute power values for the 60 second or 20 minute measurements, all averaging is done in linear space. This is because averaging in log space will cause the value to be too low, resulting in errors up to 3 or 4 dB [8].

4.3.1 Regression Analysis

Previous experiments suggest that for mid-range wind speeds (5 - 16 m/s), plots of σ^o versus the log of wind speed display a linear trend. Allowing for environmental conditions and measurement variability, Y-Scat 94 data also show

the same trend. Figure 4.5 gives an example of V-pol and H-pol data at downwind, 3.05 GHz, and 30° incidence. To quantify the slope of the linear fit, the simple regression model

$$\sigma_i^o = \beta_0 + \beta_1 10log(U_i) + e_i \qquad (4.1)$$

is used, where β_0 is the y-axis intercept, β_1 is the slope, U is the wind speed in m/s, and e_i represents the random error term which is assumed to be normally distributed. Least squares regression minimizes the residual sum of squares which is defined as

$$R_{ss} = \sum(\hat{\sigma_i^o} - \sigma_i^o)^2 \qquad (4.2)$$

where $\hat{\sigma_i^o}$ is the estimate of σ_i^o. In this model, σ^o is assumed to be the random process and the wind speed is assumed to be deterministic. This isn't the only assumption that can be made. If both σ^o and wind speed are assumed to be random, then an orthogonal regression can be employed. According to Chaudhry and Moore, the slopes calculated by regressing σ^o vs log(U) will generally be higher than those computed with orthogonal regression, and that orthogonal regression will generate higher values than regressing log(U) vs σ^o [4].

Standard statistical tests can be used to examine the applicability of a regression model [26]. To quantify the fit of the data to a power law model, three parameters are analyzed. These are the standard deviation of the error between the data points and the linear fit $(std(R_{ss}))$, the standard error of the slope se(β_1), and the coefficient of determination (R^2). R^2 is found by the following equation

$$R^2 = 1 - \frac{R_{ss}}{S_{\sigma^o\sigma^o}} = r_{U\sigma^o}^2 \qquad (4.3)$$

where R_{ss} is the residual sum of squares, and $S_{\sigma^o\sigma^o}$ is sum of squares of the σ_i^o's. Note that R^2 is also equal to the square of the sample cross correlation coefficient between U and σ^o values. R^2 can be interpreted as the proportion of variability in σ^o explained by the regression on U [26]. Note that an R^2 of one is a perfect fit.

Figure 4.6 shows the result of regression on the data presented in 4.5. Note that for the V-pol case R^2 is $< .5$, which suggests that the variability in σ^o is not explained any more by changes in wind speed than it is by measurement
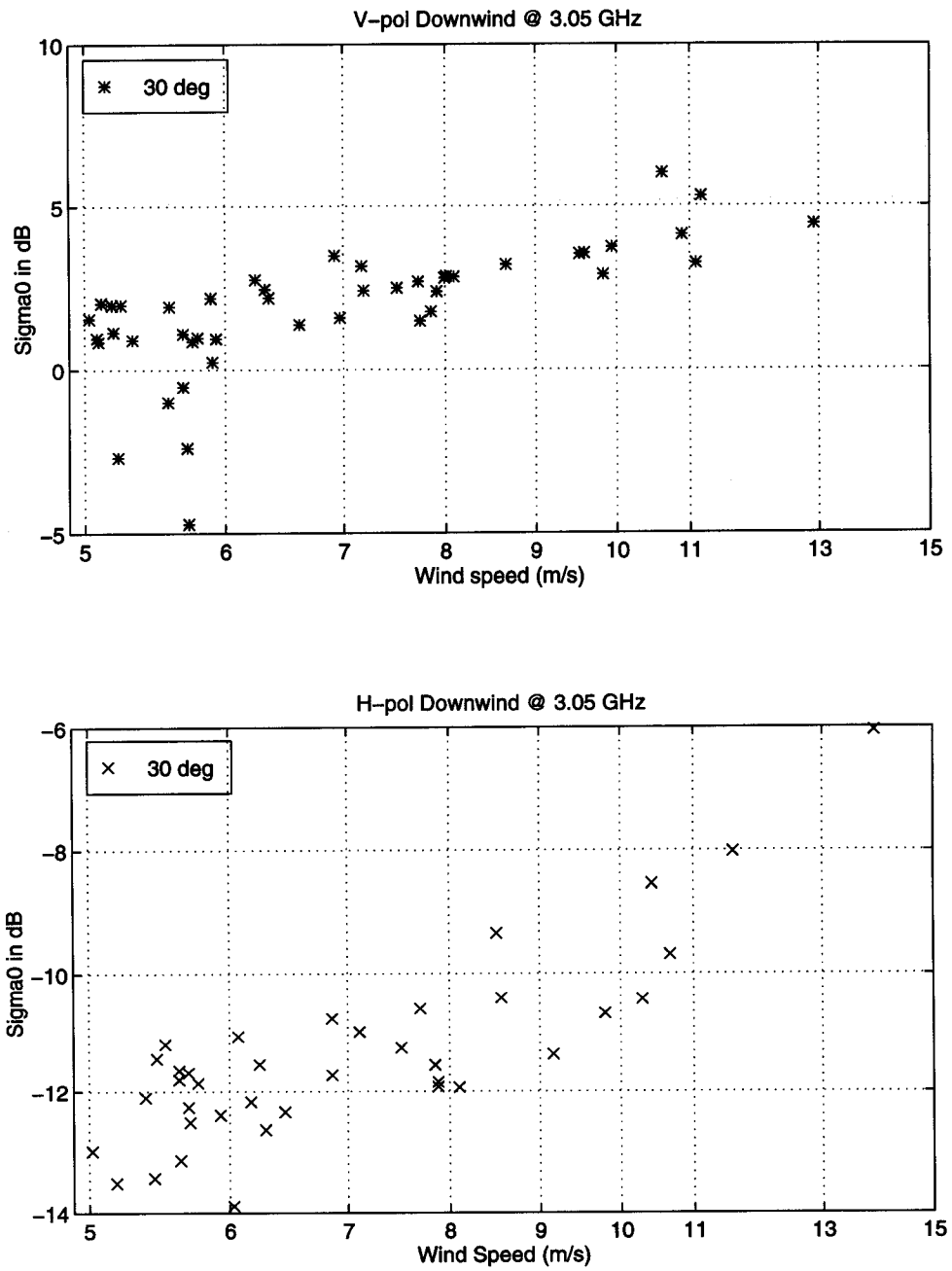
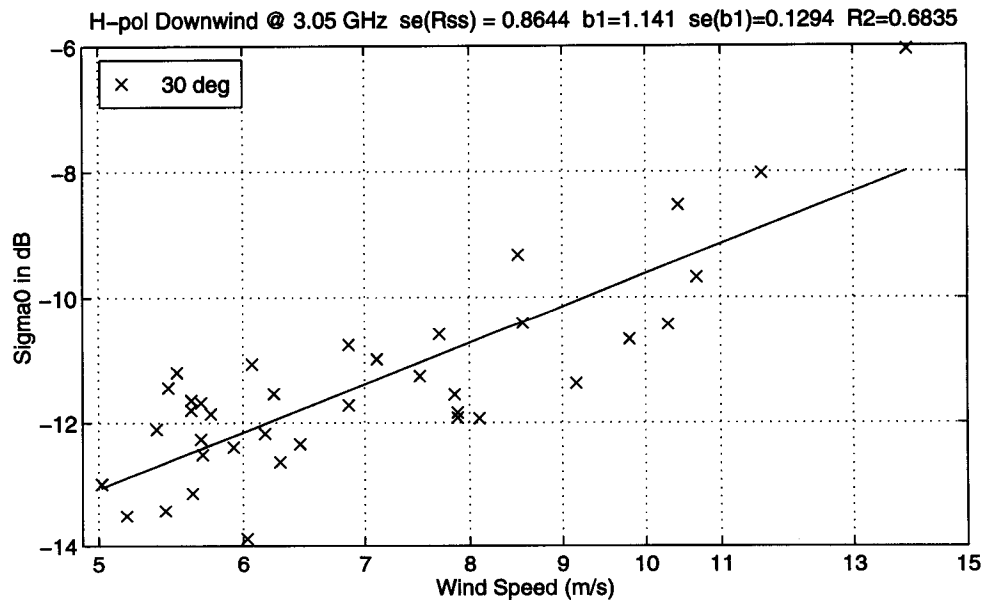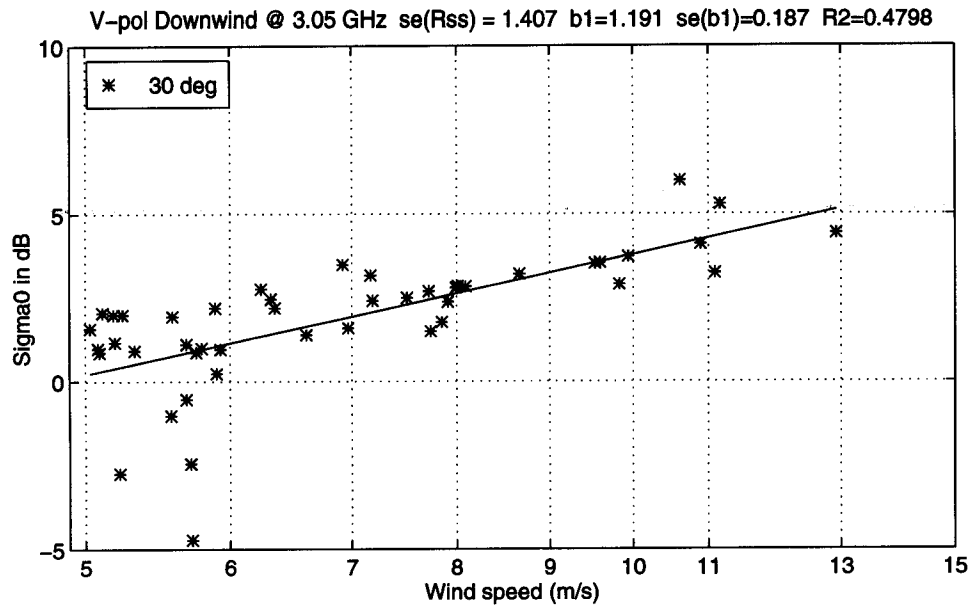Figure 4.5: Data points for 3.05 GHz at downwind and 30° incidence.

Figure 4.6: Linear regression fit to data shown in Figure 4.5 using all points.

noise. However, visual inspection shows that there is a definite linear trend to the data. The low value of R^2 is likely a result of the data variability. One method to improve the regression fit is outlier correction. It appears that low σ^o values from 5-6 m/s are causing the greatest error. Discarding these outliers results in a better fit (see Fig. 4.7). Outliers are defined as points that are more than $+/-$ 2σ from the initial regression fit. Using this method, improves R^2 to 0.63, while decreasing the slope from 1.2 to .96. The difficulty with outlier correction is determining where to set the threshold, since a "truth value" is not available. Particularly, at higher wind speeds where the data are scarce, deciding which points are accurate becomes difficult. A comparison is done by computing the regression with 1.5, 2, and 2.5 σ as the outlier criteria. The results are given in Table 4.1. Note that with the exception of H-pol upwind 10 GHz and 14 GHz, the values of slope do not change significantly between the three cases. Further results will use the $+/-$ 2σ as the outlier criteria.

As an alternative to outlier correction, binning the measurements by wind speed and averaging can be implemented. Some data points in each wind speed bin represent different environmental conditions such as fetch length, long wave field, or possibly tower shadowing effects. Averaging the measurements within a wind speed bin into one data point will help remove these additional dependences. The size of the wind speed bin is determined by analyzing the variance of the wind measurements. Figure 4.8 illustrates the variance of some 30 second wind speed measurements plotted against wind speed. The mean of all the variances plotted is 0.492 resulting in a standard deviation of 0.702. Choosing the bin size to be commensurate with the standard deviation of the wind speed measurements, a wind speed bin of 1 m/s is selected. Figure 4.9 displays the resulting fit applied to the averaged σ^o values. Note that R^2 improves for both the V-pol and H-pol cases, while the slopes change slightly. This result indicates that averaging data into wind speed bins removes measurement variability as would be expected. For the binning method, the measurements are averaged in log space, since averaging in linear space will unfairly weight the higher σ^o values. The drawback of averaging is that only a few points are used in the regression and therefore the 90% confidence error bars of the slope are much higher than in the outlier case. The complete results of the regression on all the data is presented in Chapter 5.

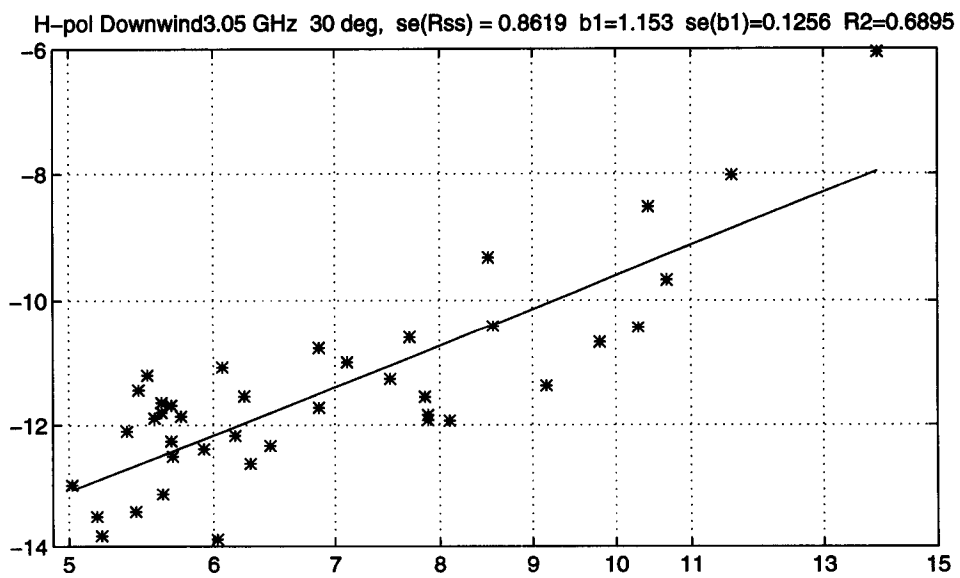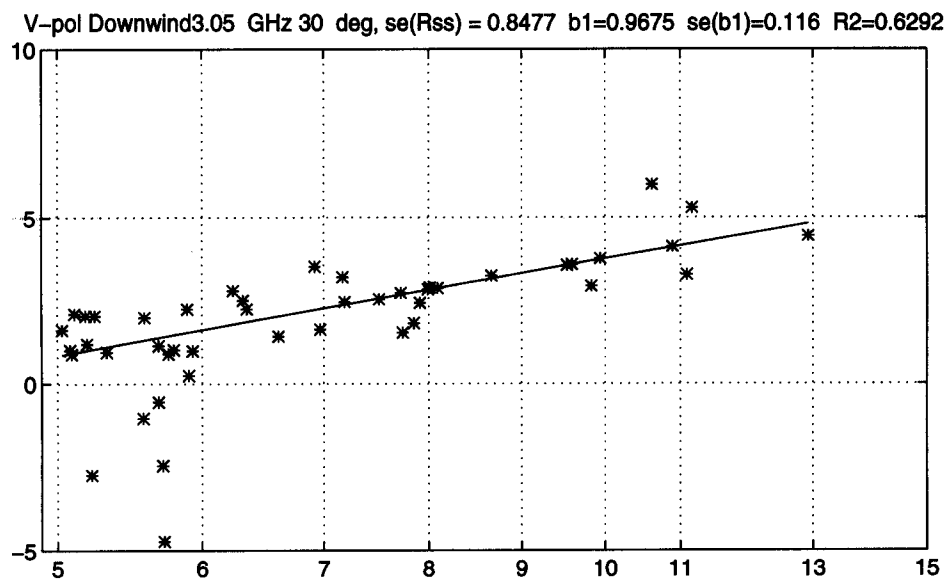V-pol Downwind3.05 GHz 30 deg, se(Rss) = 0.8477 b1=0.9675 se(b1)=0.116 R2=0.6292

H-pol Downwind3.05 GHz 30 deg, se(Rss) = 0.8619 b1=1.153 se(b1)=0.1256 R2=0.6895

Figure 4.7: Linear Regression fit to data shown in Figure 4.5 using $+/-$ 2σ outlier correction.

31

Wind Exponents Using +/- 1.5σ						
Frequency	V-Pol			H-Pol		
(Ghz)	30°	40°	50°	30°	40°	50°
2.0	.405	.774	.765	.225	.238	.354
3.05	.889	1.244	1.462	.686	.585	.360
5.30	1.536	2.212	2.701	.759	1.824	2.784
10.02	4.031	4.087	3.619	1.715	1.868	4.076
14.00	3.698	4.618	4.45	2.085	2.993	2.738

Wind Exponents Using +/- 2.0σ						
Frequency	V-Pol			H-Pol		
(Ghz)	30°	40°	50°	30°	40°	50°
2.0	.503	.798	.759	.703	.471	.596
3.05	.889	1.244	1.459	.801	1.610	.776
5.30	1.536	2.293	2.798	1.962	2.011	2.644
10.02	4.359	3.755	3.610	2.448	3.809	4.515
14.00	2.970	4.802	4.561	3.380	3.383	3.610

Wind Exponents Using +/- 2.5σ						
Frequency	V-Pol			H-Pol		
(Ghz)	30°	40°	50°	30°	40°	50°
2.0	.553	.895	.759	.704	.471	.619
3.05	.984	1.266	1.459	.944	1.610	.774
5.30	1.653	2.293	2.697	1.942	2.176	2.905
10.02	3.609	3.824	3.312	2.448	4.031	4.515
14.00	3.071	4.098	4.537	3.462	3.347	3.686

Table 4.1: Comparison of slopes calculated using different outlier threshold values.
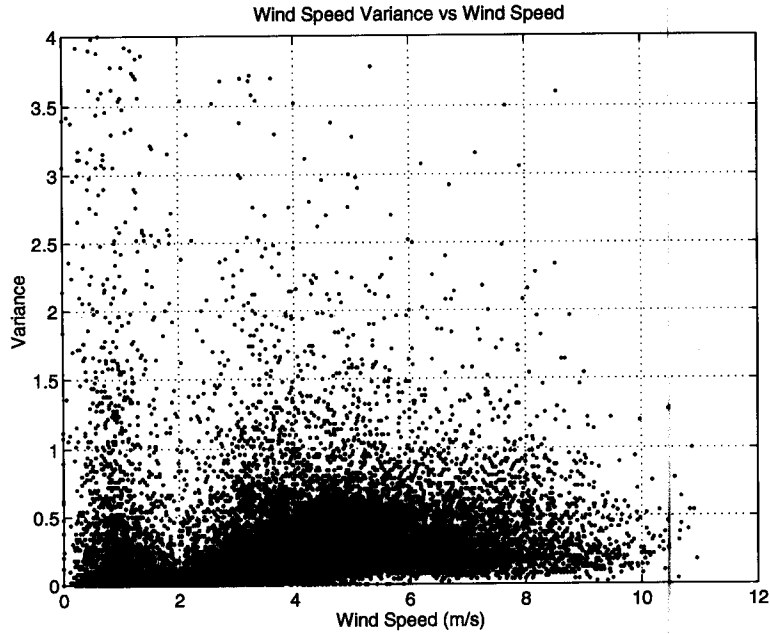
Figure 4.8: Variance of some 30 second wind speed averages plotted against wind speed.

4.3.2 Confidence Intervals

There are many sources of variability associated with each σ^o measurement including environmental conditions, noise, radar system fluctuations, and calibration uncertainties. As previously discussed, 60 second measurement lengths were chosen to average out effects of the background wave field. Averaging samples into one measurement reduces the statistical variance of each individual measurement. The variance of each average power measurement can be quantified by computing confidence intervals. As shown in [27], confidence intervals of sample means can be computed assuming the data are independent and normally distributed. With these assumptions, the sample mean follows a student-t distribution. For N+1 independent samples the confidence intervals are given by

$$\hat{\mu} - \frac{st_{\alpha/2,N}}{\sqrt{N}} \leq \mu \leq \hat{\mu} + \frac{st_{\alpha/2,N}}{\sqrt{N}} \tag{4.4}$$

where $\hat{\mu}$ is the sample mean, s is the estimate of the sample standard deviation, and $t_{\alpha/2,N}$ is percentile value of student-t distribution with a $(1 - \alpha)$ confidence level. The values of $t_{\alpha,N}$ are found in the appendices of most statistics books. To apply
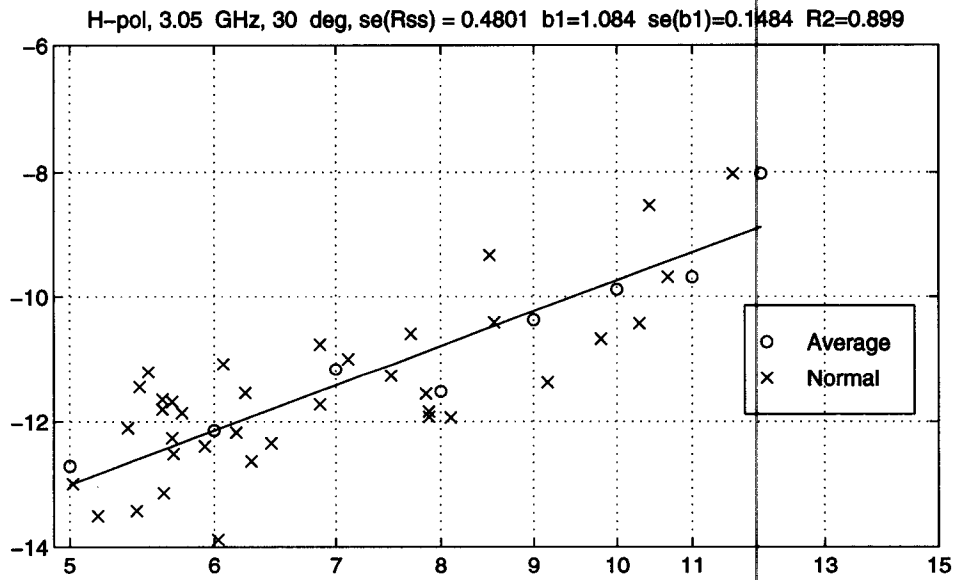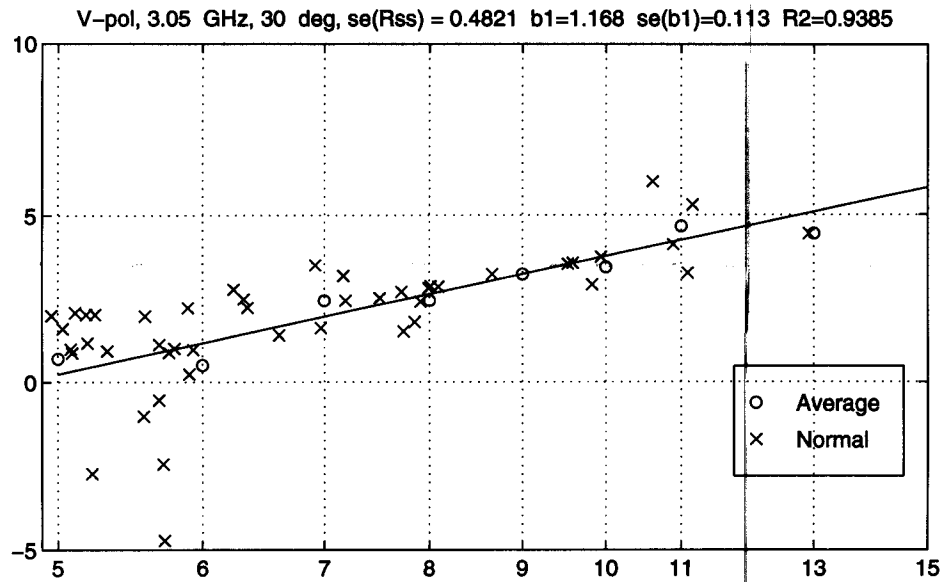
Figure 4.9: Linear regression fit to data shown in Figure 4.5 using 1 m/s wind speed bin averaging.

this equation to Y-Scat 94 data the assumptions of normality and independence need to be discussed. The assumption of normality is easily handled by applying the central limit theorem since the number of samples is large (several hundred). The notion of independence is more difficult to define and is discussed next.

The number of independent samples is related to the correlation times of the microwave backscatter signal. Assuming that the correlation function falls off as $e^{-a\tau}$, the correlation time is the is the time required for the correlation function to decay to $1/e$ of its maximum value. The correlation times are a function of frequency with higher frequencies corresponding to shorter values. Plant et. al. [28] state that at X-band the correlation time is approximately 10 ms. This suggests that at X-band, 0.1 sec power measurements are essentially uncorrelated. Following the methods of Plant et. al. the correlation times can be found from an estimate of the radial velocity spread which is given by

$$\delta_{v_r} = \frac{\lambda(\bar{f_2})^{1/2}}{2}. \tag{4.5}$$

In this equation δ_{v_r} is the radial velocity spread, λ is the microwave wavelength, and $\bar{f_2}$ is the 2nd moment of the Doppler spectrum. The value of $\bar{f_2}$ can be found from the Doppler bandwidth estimate that is included with each power measurement. Finally, the correlation time, t_0 is found from

$$t_0 = \frac{\lambda}{4\sqrt{\pi}\delta_{v_r}}. \tag{4.6}$$

Using Eq. (4.5) and (4.6), correlation times are computed for approximately 10,000 0.1 sec samples at each frequency and polarization. These samples consist of 18 one minute power measurements with incidence angles ranging from 30° to 50°, and mid-range wind speeds (5 - 9 m/s). The resulting average correlation times and standard deviations are shown in Table 4.2. Note that even for the largest correlation time (13.5 ms) at 3.05 GHz, $t_0 + \sigma$ is less than 20 ms. A 20 ms correlation time implies that one half of the .1 sec samples can be considered uncorrelated. Using 20 ms as a conservative estimate for all frequencies and incidence angles considered, confidence intervals are calculated assuming 300 independent measurements. Although assuming that uncorrelation implies independence is not completely correct, Plant el al. state that the resulting error in doing so is small.

Correlation Times for Each Frequency

Frequency (GHz)	V - Pol		H - Pol	
	t_0 (ms)	σ	t_0 (ms)	σ
2.00	11.9	5.7	12.2	5.9
3.05	13.5	5.8	10.0	4.4
5.30	11.6	5.8	12.0	5.4
10.02	7.20	3.5	11.0	5.0
14.00	6.10	3.2	7.8	3.5

Table 4.2: Average correlation times and standard deviations for 0.1 sec power measurements from 30° to 50° incidence.

Figures 4.10 and 4.11 display the 95% confidence level error bars for σ^o at 2 GHz assuming a 20 ms correlation time. In all cases the maximum error bar is less than 2 dB and the results are similar at the other frequencies. Since the error bars are so small compared to the scale of the plots, further results will not display them.

4.4 Summary

This chapter has described the data editing and analysis techniques employed in this thesis. The data are binned according to frequency, polarization, incidence angle, wind speed and relative azimuth angle. Only measurements which correspond to upwind or downwind and wind speeds higher than 4.5 m/s are analyzed. All data corrupted by heavy rain and hardware anomalies are discarded. A power law model relating σ^o to wind speed is adopted and three different linear regression techniques (using all points, +/- 2σ outlier removal, and 1 m/s wind speed bin averaging) are used to determine the wind speed exponents. It is shown that both outlier removal and 1 m/s wind speed bin averaging result in better data fits than using all points. Further comparison and the rationale for selecting the "best" method is given in the next chapter.
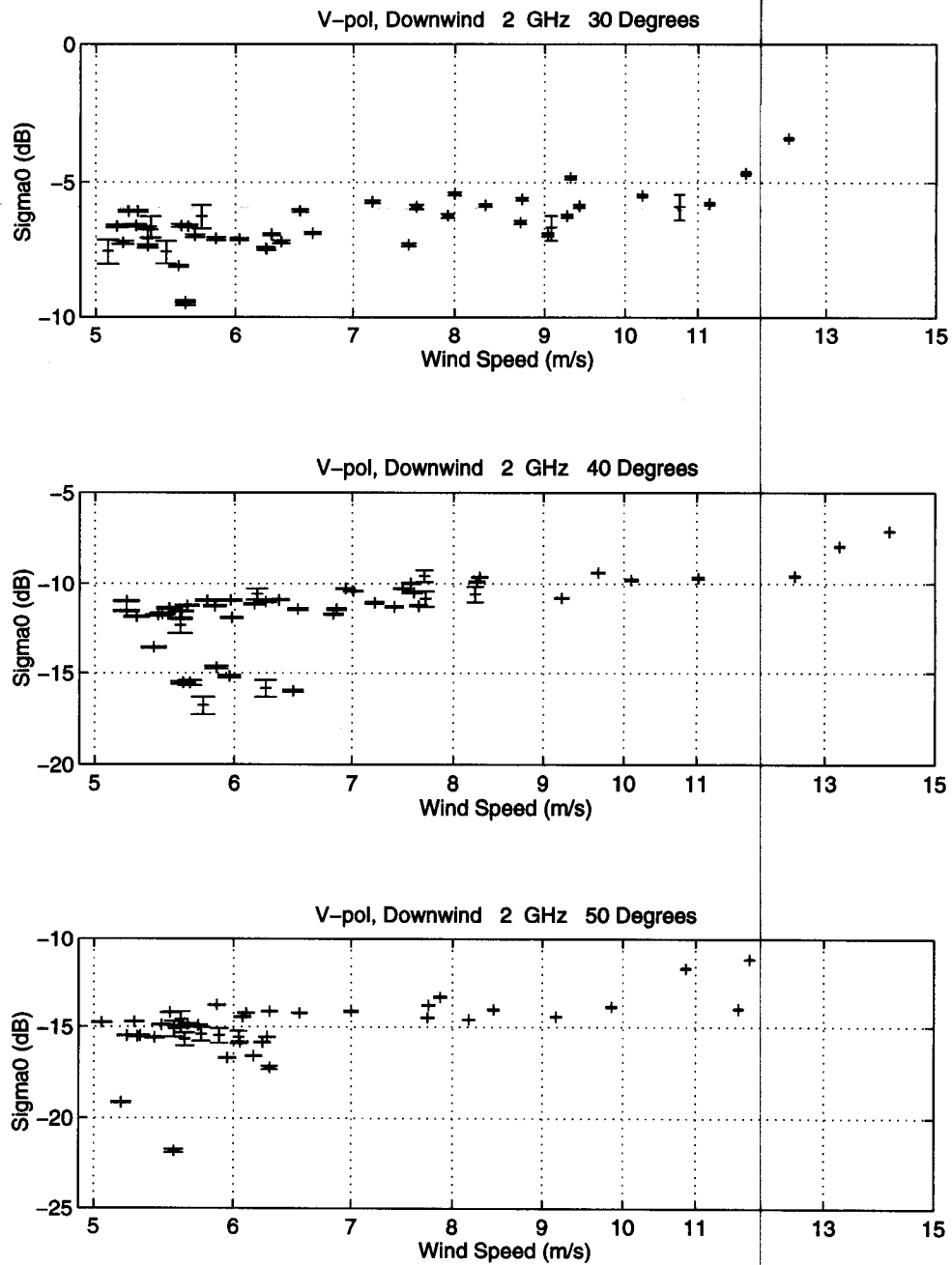
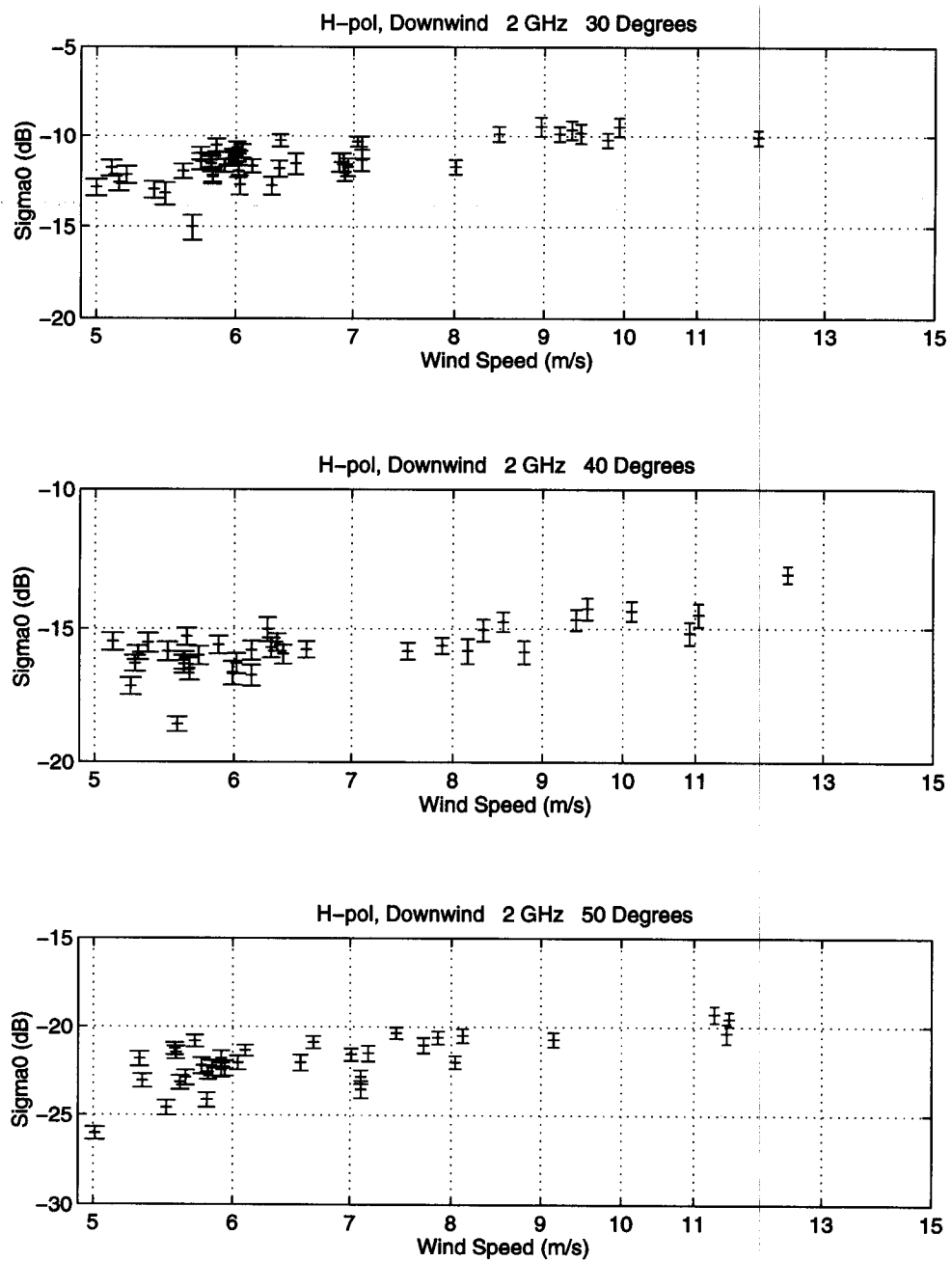Figure 4.10: 95% Confidence error bars of σ^o for 2 GHz downwind.

Figure 4.11: 95% Confidence error bars of σ^o for 2 GHz downwind.

CHAPTER 5

RESULTS AND DISSCUSSION

5.1 Introduction

As mentioned previously, a primary objective of this thesis is to investigate the sensitivity of σ^o to wind speed and direction. The sensitivity to wind speed is conveniently analyzed through the wind speed exponent (γ). The sensitivity to wind direction can be expressed in terms of the wind speed exponent and the y-intercept (A_0) of the regression fit. Both the wind speed exponent and A_0 are found with the power law model function.

Using a power law fit to the data, this Chapter analyzes 1) wind speed exponent (γ) as function of incidence angle, 2) γ as function of Bragg wavelength, 3) differences between γ for V-pol, H-pol, upwind, and downwind, and 4) upwind/downwind σ^o ratio as a function of Bragg wavelength and wind speed.

5.2 Wind Exponent (γ) Results

Recall the power law model function discussed in Chapter 2

$$\sigma^\circ \;=\; A_0 U^\gamma. \tag{5.1}$$

Using the three regression methods described in the previous chapter, the least squares linear fit is found for each frequency, incidence angle and polarization for both upwind and downwind cases. Tables 5.1 thru 5.4 give the values of relevant regression parameters, including slope (γ), 90% confidence levels (Conf), y - intercept (A_0), and coefficient of determination (R^2). The method column refers to +/-2σ outlier removal, 1 m/s wind speed bin averaging, and regression using all the measurements. The confidence value given is the 90% +/- offset value of the slope. The confidence values are large compared to the slope for the 2 GHz upwind case. Note that except in a few cases, γ does not vary significantly between the three methods. The largest variations occur for the V-pol 10 and 14 GHz cases where the measurements exhibit the most scatter. In general, the +/- 2σ outlier

removal method gives the smallest 90% confidence level error bars, while the average method produces the best R^2 value. Since the purpose of the regression is to characterize the slope, the smallest deviation of the slope (smallest error bars for the slope) is chosen as the optimization criteria in selecting which method's results to present. Therefore, the remainder of the chapter will present results obtained using the $+/-$ 2σ outlier removal method. To summarize these results, Figures 5.1 thru 5.5 display the linear fits for the V-pol, H-pol, upwind, and downwind cases.

The plots of σ^o versus log(U) for all frequencies, which show all the data along with the least squares linear regression fit, are presented in Appendix A. The slope (γ) of the fit is given at the top of each plot. As mentioned, the V-pol 10 GHz and 14 GHz measurements exhibit considerable scatter. This phenomena has also been observed by Plant et al. [6] who state that the data spread at X-band is always considerable when wind speed is used as the independent variable. Since there is much less scatter in the data at lower frequencies, it is suggested that σ^o at X and Ku band is more sensitive to other unmodeled geophysical parameters than it is at lower frequencies.

V-Pol 2.0 GHz									
Inci	Method	Upwind				Downwind			
(θ)		γ	Conf	A_0	R^2	γ	Conf	A_0	R^2
30	out	0.24	0.23	-8.68	0.10	0.50	0.14	-10.64	0.44
30	ave	0.24	0.49	-8.74	0.30	0.70	0.30	-12.41	0.77
30	all	0.24	0.31	-8.77	0.05	0.62	0.19	-11.77	0.37
40	out	0.09	0.27	-11.96	0.02	0.80	0.16	-17.57	0.60
40	ave	-0.23	1.00	-9.60	0.06	1.03	0.32	-19.89	0.84
40	all	-0.12	0.62	-10.48	0.01	0.95	0.31	-19.28	0.33
50	out	0.40	0.45	-18.28	0.09	0.76	0.20	-20.91	0.46
50	ave	0.37	0.70	-18.13	0.34	1.14	0.36	-24.32	0.84
50	all	0.40	0.45	-18.28	0.09	0.85	0.31	-21.84	0.30
V-Pol 3.05 GHz									
Inci	Method	Upwind				Downwind			
(θ)		γ	Conf	A_0	R^2	γ	Conf	A_0	R^2
30	out	0.85	0.28	-5.05	0.49	0.89	0.17	-5.22	0.63
30	ave	1.30	2.07	-10.18	0.42	1.17	0.21	-7.92	0.94
30	all	2.04	1.20	-15.89	0.20	1.15	0.31	-7.72	0.44
40	out	0.58	0.36	-6.06	0.16	1.24	0.25	-12.06	0.51
40	ave	0.58	0.97	-6.67	0.29	1.43	0.41	-13.79	0.91
40	all	0.53	0.62	-6.09	0.05	1.44	0.50	-14.00	0.26
50	out	0.89	0.32	-11.52	0.44	1.46	0.20	-16.32	0.74
50	ave	1.42	1.37	-16.74	0.66	1.81	0.27	-19.64	0.96
50	all	1.67	0.85	-18.77	0.25	1.69	0.36	-18.56	0.51
V-Pol 5.30 GHz									
Inci	Method	Upwind				Downwind			
(θ)		γ	Conf	A_0	R^2	γ	Conf	A_0	R^2
30	out	1.29	0.41	-19.96	0.41	1.54	0.23	-21.97	0.70
30	ave	1.30	0.75	-19.97	0.77	1.65	0.79	-23.61	0.69
30	all	1.08	0.64	-18.39	0.16	2.10	0.49	-27.38	0.46
40	out	1.25	0.57	-25.02	0.37	2.29	0.36	-33.94	0.66
40	ave	1.61	1.07	-27.81	0.91	2.47	0.39	-35.99	0.96
40	all	1.61	0.79	-27.87	0.32	2.58	0.54	-36.81	0.50
50	out	3.07	0.97	-43.36	0.62	2.80	0.29	-41.81	0.83
50	ave	3.41	0.41	-46.21	0.99	2.92	0.36	-43.42	0.97
50	all	2.25	1.00	-37.29	0.44	2.76	0.36	-41.88	0.74

Table 5.1: V-pol regression Results at 2, 3, and 5 GHz.

V-Pol 10.02 GHz									
Inci (θ)	Method	Upwind				Downwind			
		γ	Conf	A_0	R^2	γ	Conf	A_0	R^2
30	out	2.57	0.87	-29.45	0.34	4.36	0.82	-44.68	0.57
30	ave	2.67	0.42	-30.55	0.98	3.12	1.19	-35.29	0.81
30	all	2.33	0.88	-27.68	0.28	3.61	0.81	-39.15	0.47
40	out	3.08	1.15	-40.10	0.46	3.76	0.57	-46.18	0.69
40	ave	3.72	1.55	-45.50	0.87	4.14	0.66	-49.75	0.96
40	all	3.08	1.15	-40.10	0.46	3.82	0.61	-46.98	0.66
50	out	3.64	1.11	-47.97	0.53	3.61	0.57	-48.58	0.69
50	ave	4.00	4.59	-51.74	0.58	2.71	1.34	-40.77	0.60
50	all	3.40	1.31	-46.14	0.40	3.31	0.59	-46.11	0.63
V-Pol 14.0 GHz									
Inci (θ)	Method	Upwind				Downwind			
		γ	Conf	A_0	R^2	γ	Conf	A_0	R^2
30	out	2.92	1.34	-32.33	0.25	2.97	0.84	-34.64	0.34
30	ave	3.73	1.57	-39.11	0.91	3.24	1.86	-36.09	0.57
30	all	3.16	1.40	-34.43	0.26	3.07	0.86	-35.56	0.34
40	out	4.30	0.99	-50.00	0.57	4.80	0.84	-53.53	0.61
40	ave	5.03	1.10	-56.21	0.96	3.60	2.02	-44.19	0.67
40	all	4.28	1.03	-50.05	0.54	4.10	0.84	-48.24	0.52
50	out	4.79	1.71	-56.67	0.48	4.56	0.85	-53.91	0.64
50	ave	5.66	6.03	-64.99	0.62	3.12	1.01	-42.08	0.92
50	all	4.08	1.91	-51.74	0.34	3.76	0.94	-47.46	0.48

Table 5.2: V-pol regression Results at 10 and 14 GHz.

H-Pol 2.0 GHz									
Inci (θ)	Method	Upwind				Downwind			
		γ	Conf	A_0	R^2	γ	Conf	A_0	R^2
30	out	0.22	0.30	-12.65	0.07	0.70	0.16	-17.00	0.52
30	ave	0.88	0.57	-18.26	0.82	0.86	0.23	-18.33	0.94
30	all	0.60	0.87	-16.06	0.05	0.73	0.19	-17.27	0.45
40	out	0.12	0.26	-15.92	0.03	0.47	0.12	-19.45	0.51
40	ave	0.19	0.99	-16.36	0.13	0.71	0.29	-21.54	0.78
40	all	0.18	0.29	-16.44	0.05	0.53	0.16	-20.05	0.43
50	out	0.39	0.36	-24.25	0.17	0.60	0.20	-26.53	0.37
50	ave	0.56	0.34	-25.97	0.75	0.82	0.20	-28.53	0.95
50	all	0.57	0.39	-25.83	0.26	0.68	0.25	-27.35	0.33

H-Pol 3.05 GHz									
Inci (θ)	Method	Upwind				Downwind			
		γ	Conf	A_0	R^2	γ	Conf	A_0	R^2
30	out	0.58	0.47	-15.52	0.21	0.80	0.18	-18.14	0.56
30	ave	0.37	0.74	-13.78	0.31	1.08	0.29	-20.58	0.90
30	all	0.58	0.47	-15.52	0.21	1.00	0.20	-19.78	0.62
40	out	0.58	0.43	-21.57	0.18	1.61	0.35	-30.71	0.60
40	ave	0.92	0.50	-24.60	0.86	1.83	0.18	-32.85	0.99
40	all	1.01	0.79	-25.37	0.16	1.96	0.49	-33.80	0.51
50	out	0.26	0.21	-20.57	0.23	0.78	0.16	-25.40	0.68
50	ave	0.26	0.37	-20.58	0.67	0.91	0.25	-26.61	0.89
50	all	0.22	0.24	-20.32	0.14	0.77	0.17	-25.43	0.63

H-Pol 5.30 GHz									
Inci (θ)	Method	Upwind				Downwind			
		γ	Conf	A_0	R^2	γ	Conf	A_0	R^2
30	out	0.68	0.47	-20.53	0.18	1.96	0.29	-32.01	0.77
30	ave	0.75	0.48	-20.98	0.73	2.04	0.49	-33.05	0.93
30	all	0.68	0.47	-20.53	0.18	2.20	0.50	-34.25	0.57
40	out	1.90	0.66	-36.40	0.56	2.01	0.27	-40.23	0.76
40	ave	2.08	0.61	-38.00	0.96	2.50	0.78	-44.91	0.87
40	all	1.90	0.66	-36.40	0.56	2.17	0.42	-42.03	0.58
50	out	2.72	0.56	-49.87	0.77	2.64	0.48	-52.23	0.70
50	ave	2.80	1.30	-50.55	0.90	3.35	0.82	-58.38	0.95
50	all	2.72	0.56	-49.87	0.77	2.94	0.61	-55.06	0.63

Table 5.3: H-pol regression results at 2, 3, and 5 GHz.

H-Pol 10.02 GHz									
Inci	Method	Upwind				Downwind			
(θ)		γ	Conf	A_0	R^2	γ	Conf	A_0	R^2
30	out	1.72	0.75	-24.80	0.38	2.45	0.41	-32.86	0.66
30	ave	1.88	1.97	-26.29	0.63	3.01	0.56	-37.66	0.94
30	all	2.56	1.42	-32.00	0.27	2.84	0.61	-36.39	0.54
40	out	1.68	0.62	-30.80	0.48	3.81	0.66	-51.44	0.70
40	ave	1.69	0.86	-30.96	0.82	3.89	0.71	-52.44	0.95
40	all	1.67	0.77	-30.75	0.36	4.16	0.77	-54.61	0.66
50	out	3.55	1.06	-53.06	0.61	4.52	0.67	-64.99	0.78
50	ave	4.29	1.06	-59.56	0.99	4.38	1.26	-63.72	0.91
50	all	4.00	1.13	-56.94	0.62	4.52	0.67	-64.99	0.78
H-Pol 14.0 GHz									
Inci	Method	Upwind				Downwind			
(θ)		γ	Conf	A_0	R^2	γ	Conf	A_0	R^2
30	out	2.17	0.65	-30.74	0.64	3.38	0.54	-43.71	0.74
30	ave	2.13	1.34	-30.35	0.82	3.39	0.72	-44.00	0.95
30	all	2.36	0.70	-32.37	0.63	3.55	0.68	-45.44	0.65
40	out	2.67	0.79	-41.81	0.56	3.38	0.56	-51.45	0.70
40	ave	3.50	0.77	-49.34	0.97	2.79	0.66	-46.50	0.92
40	all	3.28	1.07	-47.17	0.49	3.48	0.64	-52.31	0.63
50	out	2.55	0.96	-47.28	0.51	3.61	0.46	-59.05	0.81
50	ave	2.25	1.11	-45.09	0.82	3.39	0.88	-57.64	0.92
50	all	2.88	1.09	-50.12	0.49	3.76	0.52	-60.49	0.77

Table 5.4: H-pol regression results at 10 and 14 GHz.
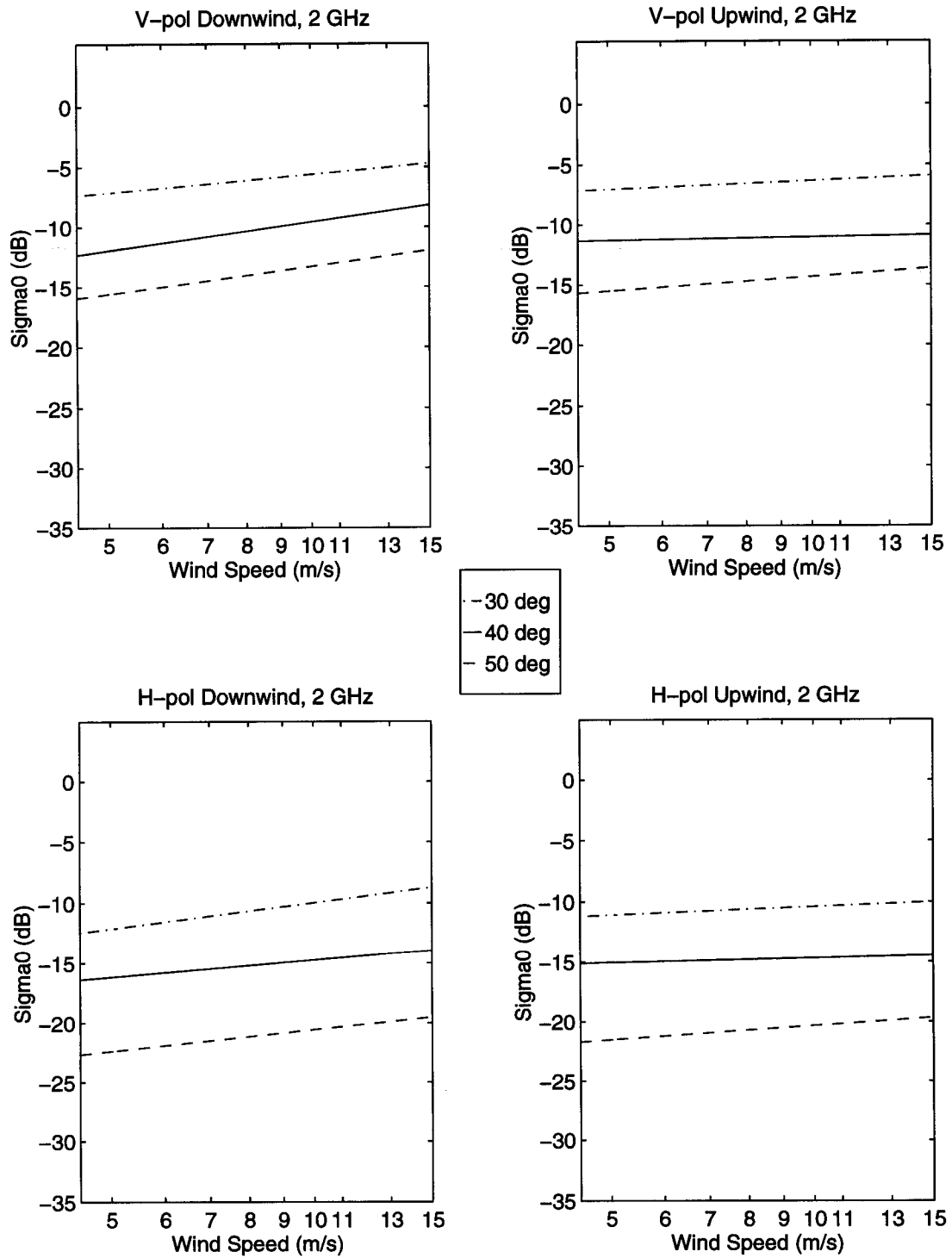
Figure 5.1: σ^o vs U(m/s) at 2.0 GHz for various incidence angles.
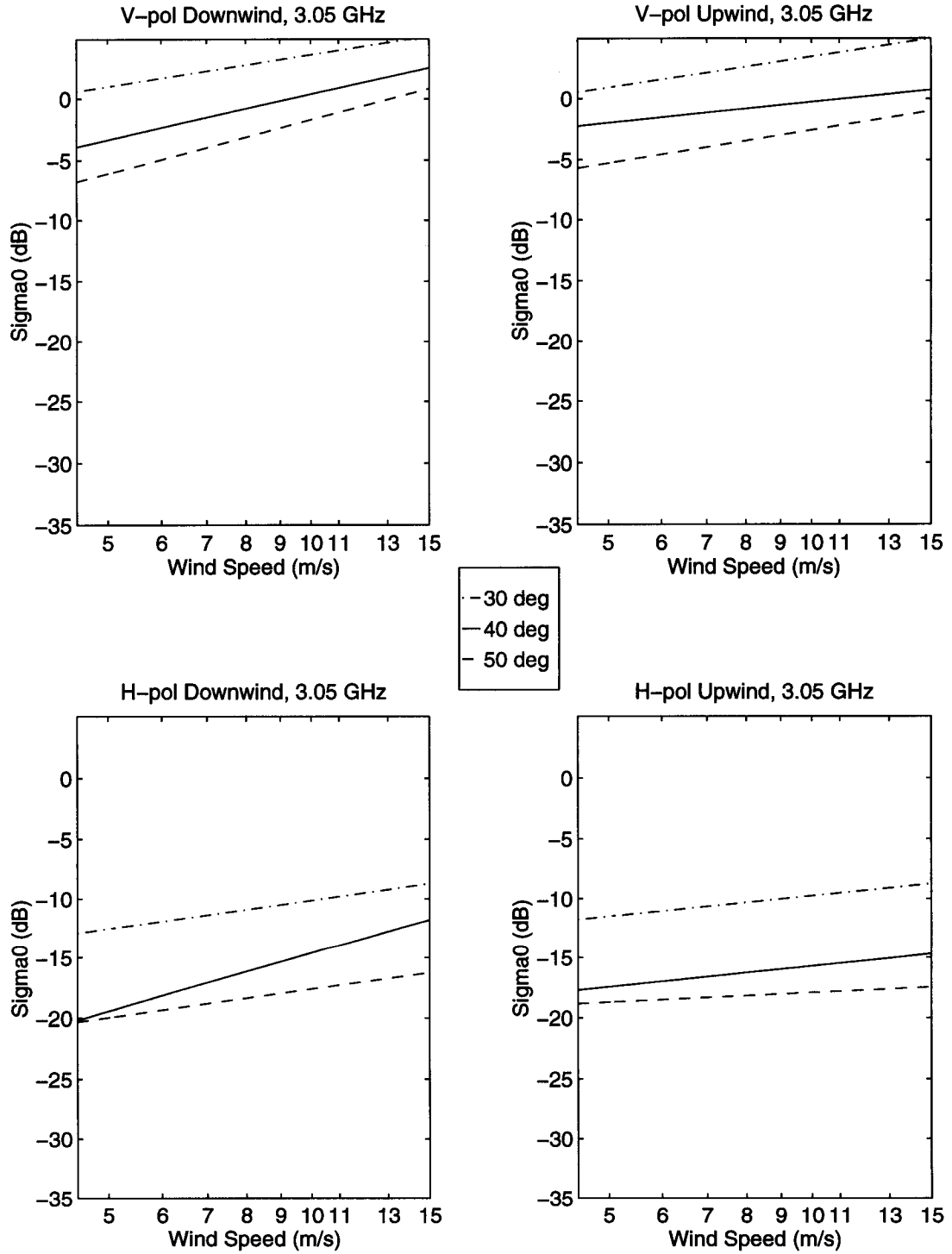
Figure 5.2: σ^o vs U(m/s) at 3.05 GHz for various incidence angles.
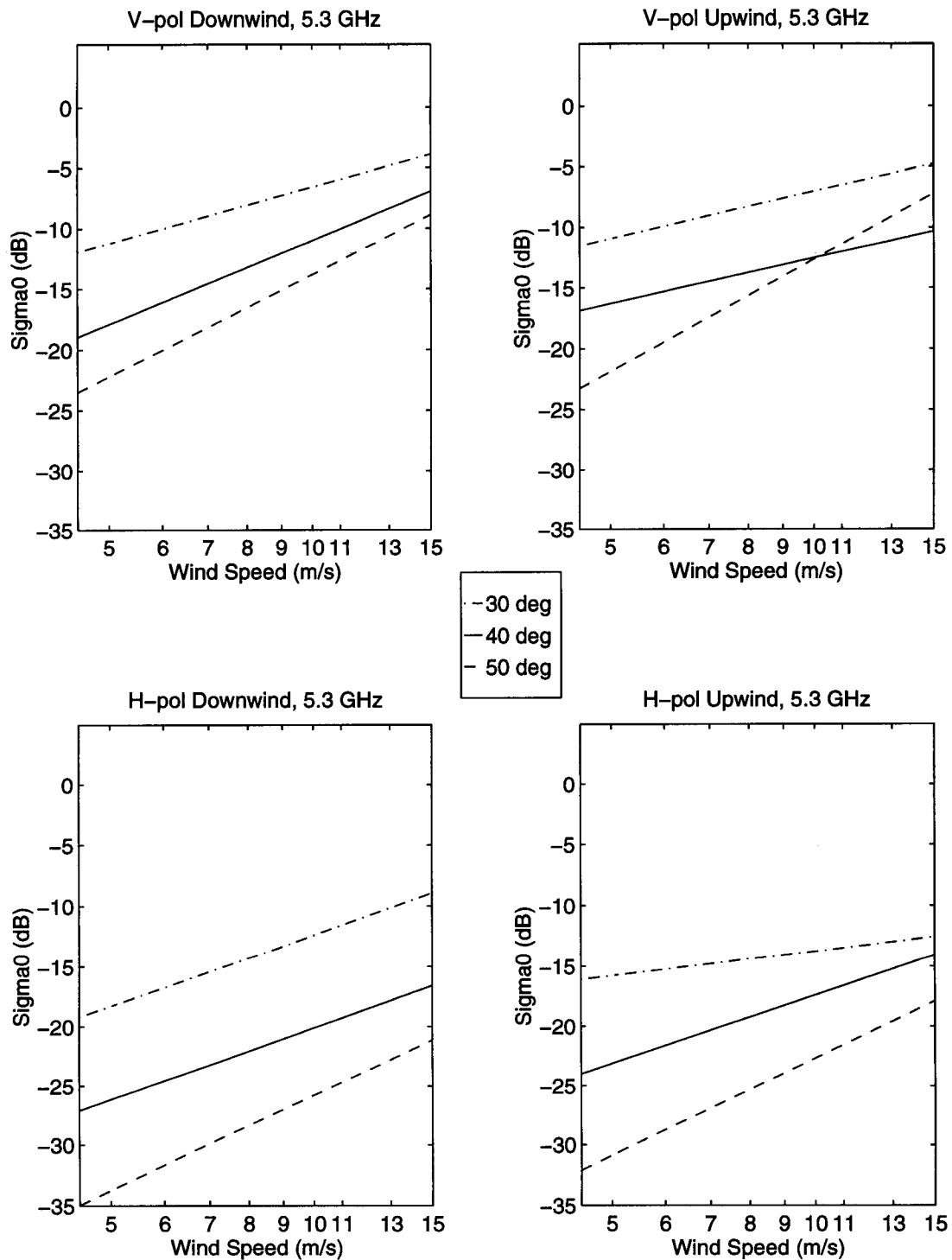
Figure 5.3: σ^o vs U(m/s) at 5.30 GHz for various incidence angles.
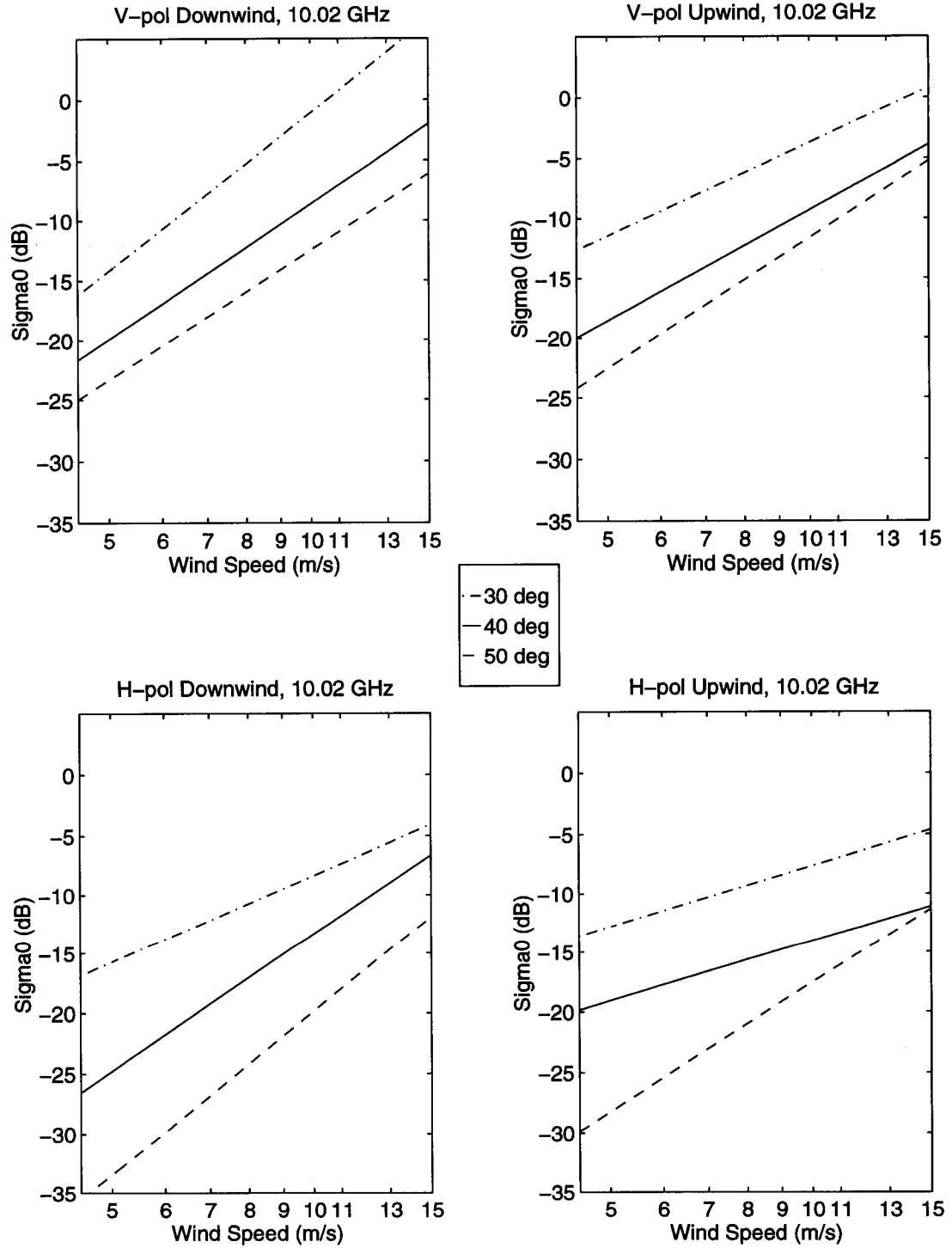
Figure 5.4: σ^o vs U(m/s) at 10.02 GHz for various incidence angles.
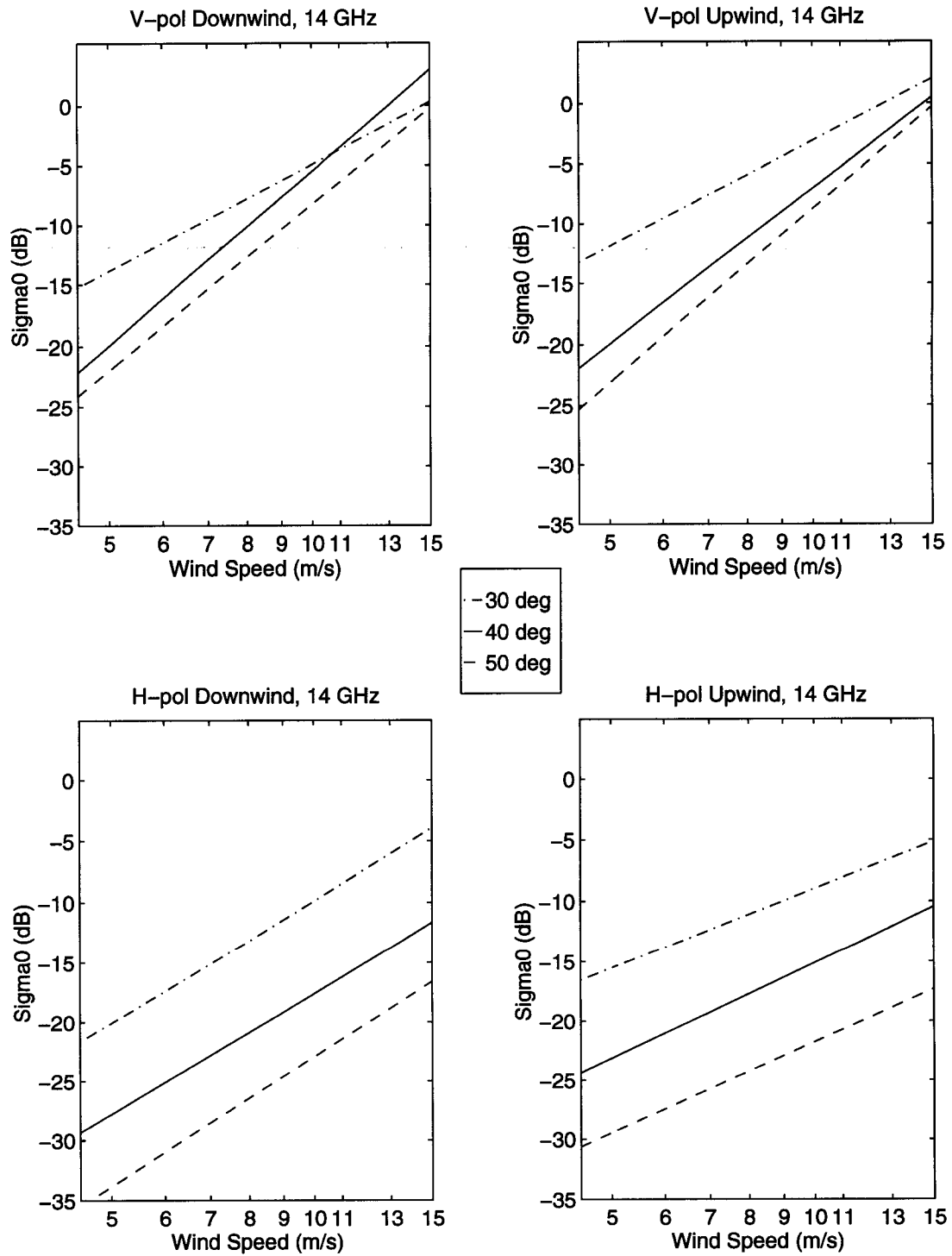
Figure 5.5: σ^o vs U(m/s) at 14.0 GHz for various incidence angles.

5.2.1 Effect of Incidence Angle on γ

Previous studies have suggested that γ increases with increasing incidence angle. Unal et al. [22] found that γ increases with incidence angle for H-pol, but that the trend is not as obvious at V-pol. Chaudhry and Moore [4] concluded that γ increased rapidly at lower incidence angles, but at larger angles ($\theta > 30°$) γ varied little. To see if Y-Scat data show similar results, the wind speed exponents are plotted against incidence angle in Figures 5.6 thru 5.10. The values at 20° and 60° have been included to give a wider range of incidence angles. The error bars represent 90% confidence limits determined from the standard error of the slopes.

In general, the data show that γ increases as θ goes from 20° to 50° and that the slopes are a function of frequency. With the exceptions of 2 GHz, V-pol downwind at 10 GHz, and H-pol upwind at 14 GHZ, the results suggest that γ peaks at 50° and then begins to decrease. This trend is more pronounced at higher frequencies. The results at 3 GHz suggest the same trend, although it is not as pronounced where γ is always less than one.

Since the wind speed exponents given by Chaudhry and Moore [4] (will be abbreviated as CM) were found at 10 GHz and 15 GHz, they can be compared to the Y-Scat X-band and Ku-Band exponents. Referring to Figures 5.9 and 5.10, notice that except at H-pol upwind, the values of γ vary little from 40° to 60°. Furthermore, the change in γ from 20° to 40° is typically large (approximately 2). Both of these observations are consistent with the results given by CM, which are stated in the first paragraph of this section.

The wind speed exponents reported by Unal et al. [22] were limited to upwind and incidence angles of 20° to 45°. At both polarizations for upwind from 20° to 40° the wind speed exponents found in this study increase with incidence angle except at 2 GHz. The increase with incident angle is consistent with the results found by Unal et al. However, the increasing trend is equally apparent at H-pol and V-pol. This is different than the results of Unal et al. who stated that V-pol did not have as large as an increase as H-pol.
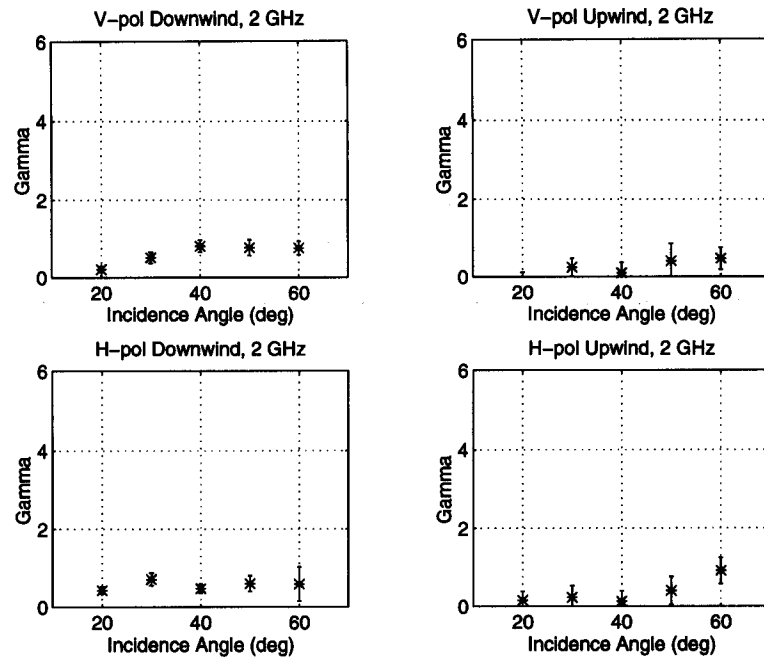
Figure 5.6: γ versus incidence angle (θ) at 2.0 GHz.
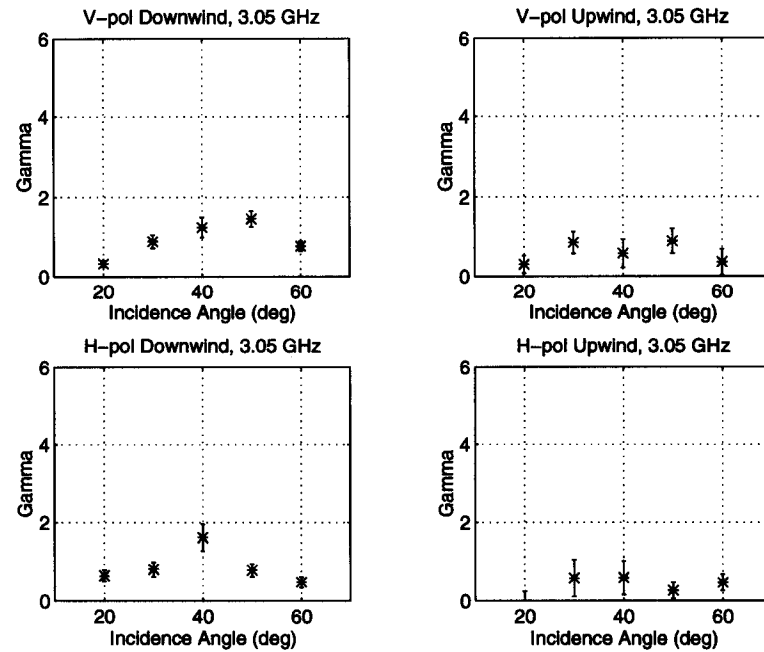
Figure 5.7: γ versus incidence angle (θ) at 3.05 GHz.
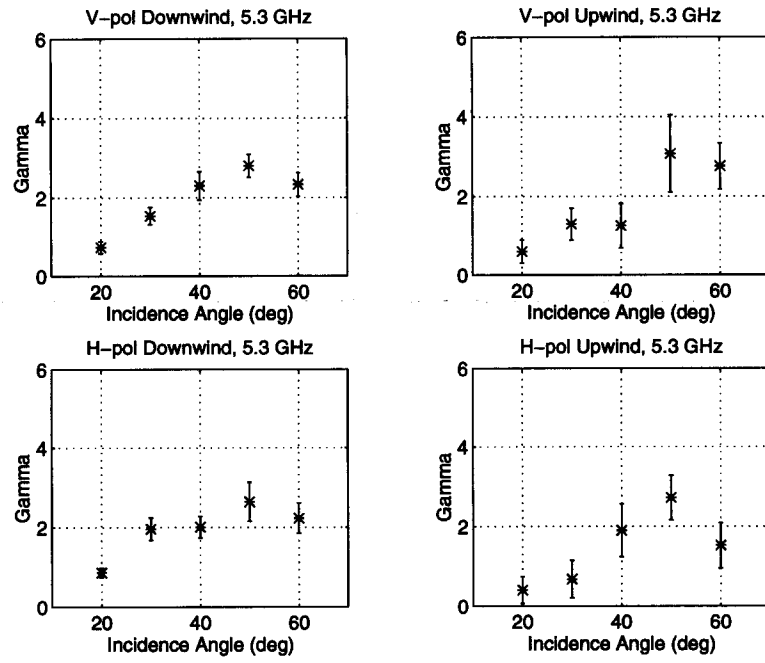
Figure 5.8: γ versus incidence angle (θ) at 5.30 GHz.
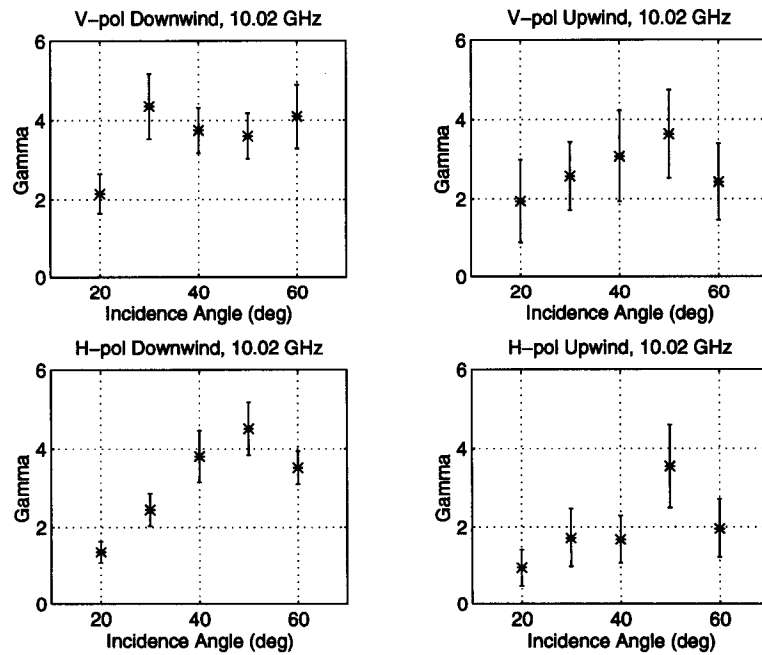
Figure 5.9: γ versus incidence angle (θ) at 10.02 GHz.
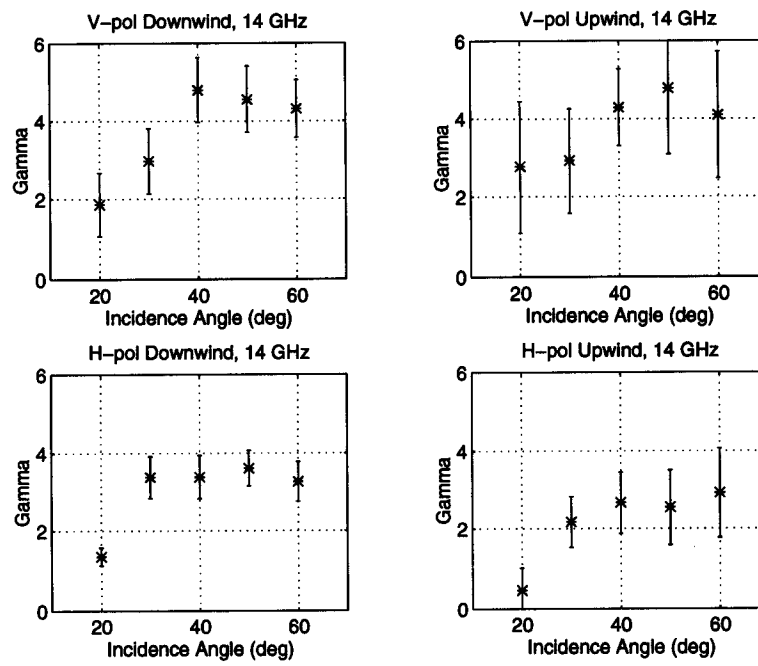
Figure 5.10: γ versus incidence angle (θ) at 14.0 GHz.

5.3 Analysis of Wind Exponent as Function of Bragg wavelength

The previous section shows that in addition to polarization and relative azimuth angle, γ is a function of both incidence angle and frequency. Assuming that σ^o is only a function of the Bragg scattering, the dependence of γ on frequency and incidence angle can be combined into a dependence on just Bragg wavelength. As stated earlier, in this thesis θ from 30° to 50° is assumed to be a purely Bragg scattering region. The following sections examine the behavior of γ as a function of Bragg wavelength.

5.3.1 Wind Speed Exponent versus Bragg wavelength

Using only incidence angles from 30° to 50°, the values of γ are plotted against Bragg wavelength. Figure 5.11 gives the result at downwind, while figure 5.12 is for the upwind case. Also shown on each plot is the least squares exponential fit to the data. The error bars display the 90% confidence levels of the γ estimates. The error bars are largest for the upwind cases as a result of the regression being computed with fewer data points compared to the downwind cases. These figures suggest that σ^o is much more sensitive to wind speed at smaller Bragg wavelengths ($\Lambda < 4cm$) than at longer wavelengths. In fact for $\Lambda > 8cm$, γ is less than one in all cases. The differences of γ between the V-pol, H-pol, upwind, and downwind cases are discussed later in the next section.

Surface ocean waves receive energy from the wind, either directly or indirectly through non-linear interactions with smaller waves. Smaller waves are generally in equilibrium with the wind and will respond quicker to changes in the wind than will larger waves. Higher wind exponents are indicative of this fact. The Bragg wavelengths of ocean waves which are very sensitive to changes in the wind speed will correspond to high wind exponents. The result that γ is less than one for $\Lambda > 8cm$, implies these waves receive their energy more from non-linear interactions with smaller waves than from the wind directly.

Figures 5.13 and 5.14 compare the wind exponents at 30° - 50° to those at 20° ('+') and 60° ('o'). The dashed lines are the same exponential fits shown before (i.e., without the 20° and 60° values). For the H-pol downwind case γ for both 20° and 60° is lower than the line, while for V-pol downwind the exponents
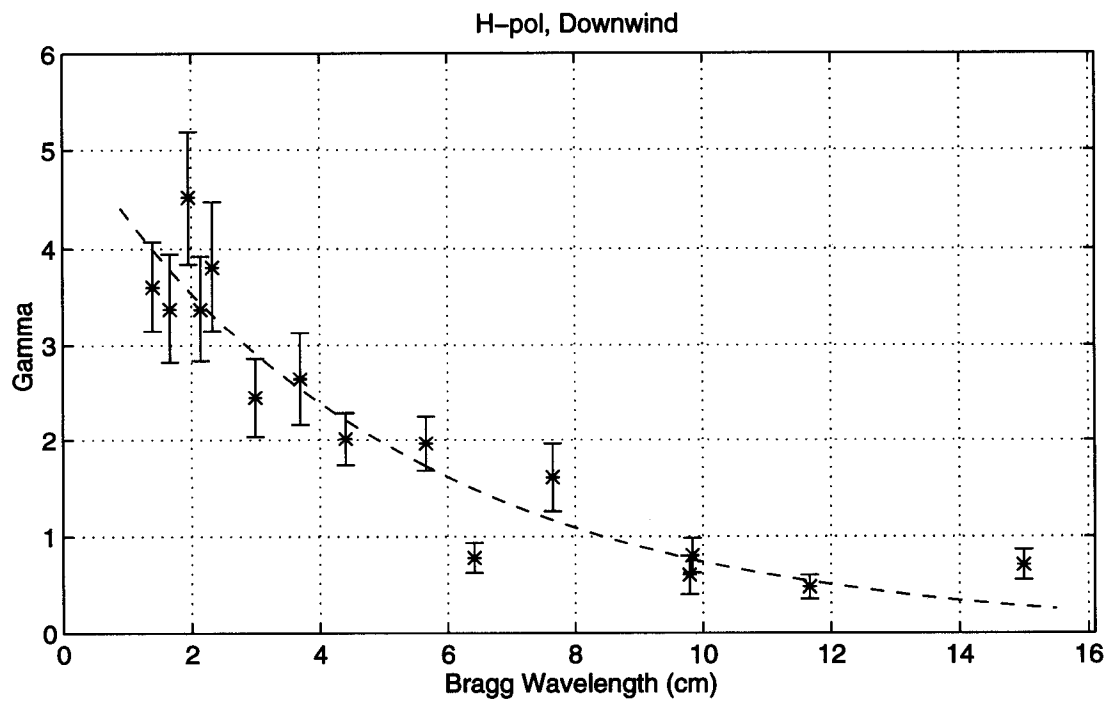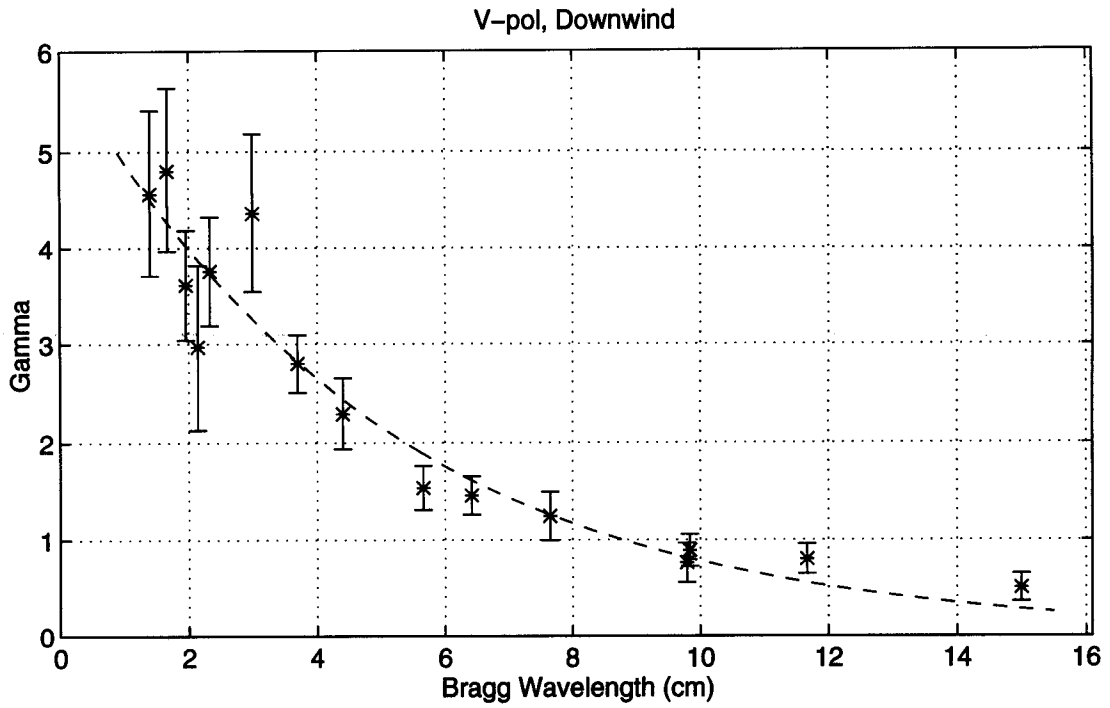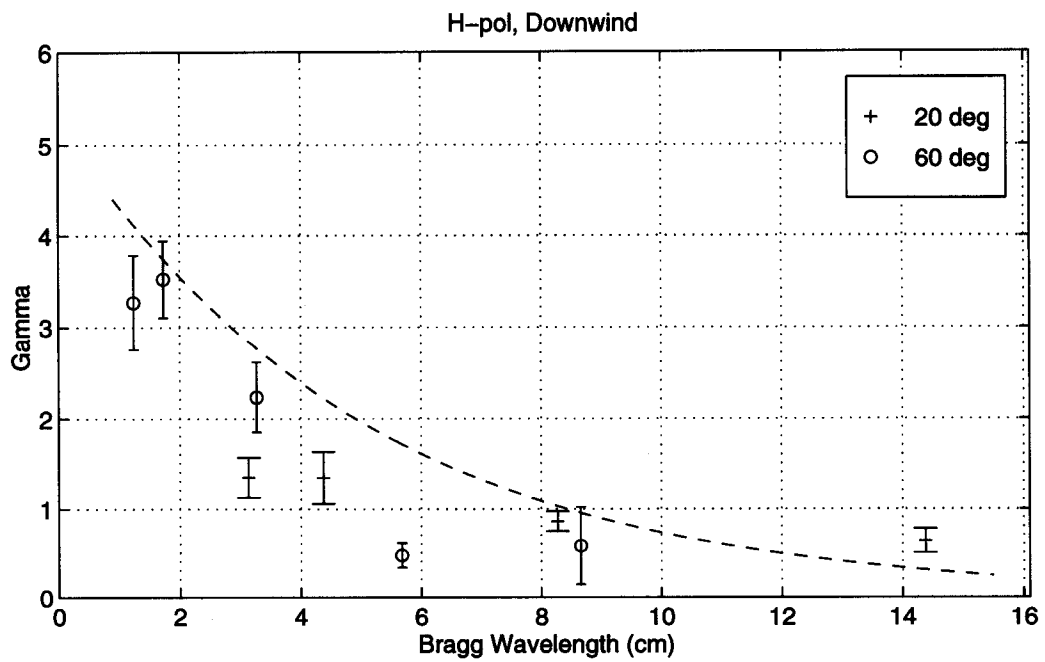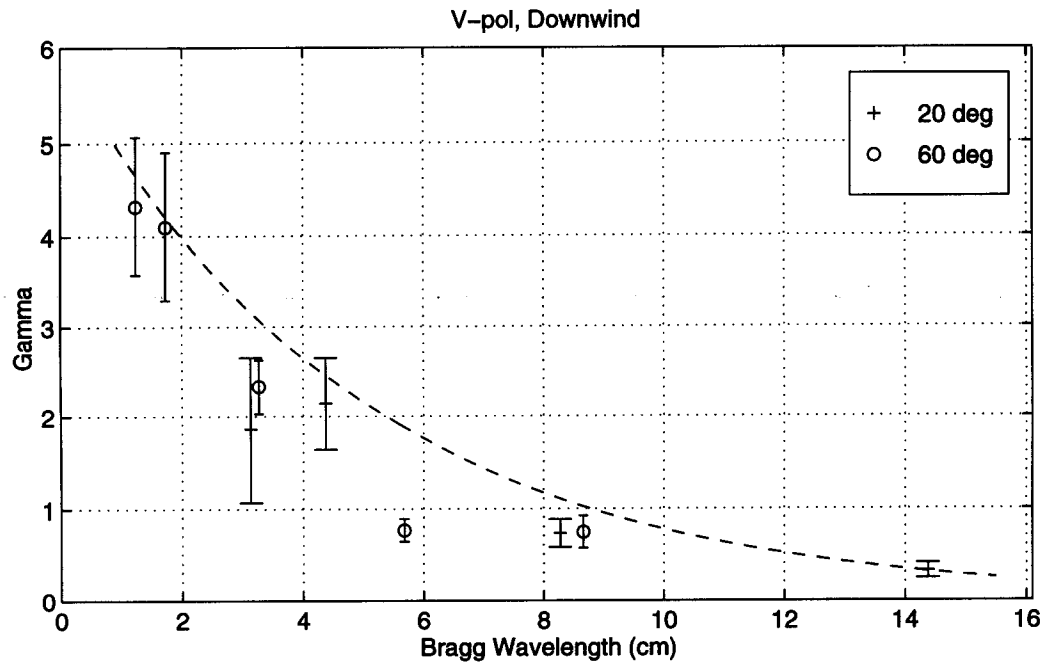
Figure 5.11: Wind Exponent (γ) as function of Bragg wavelength for downwind. The dashed line is the least squares exponential fit to the data. Only incidence angles from 30° to 50° are included.
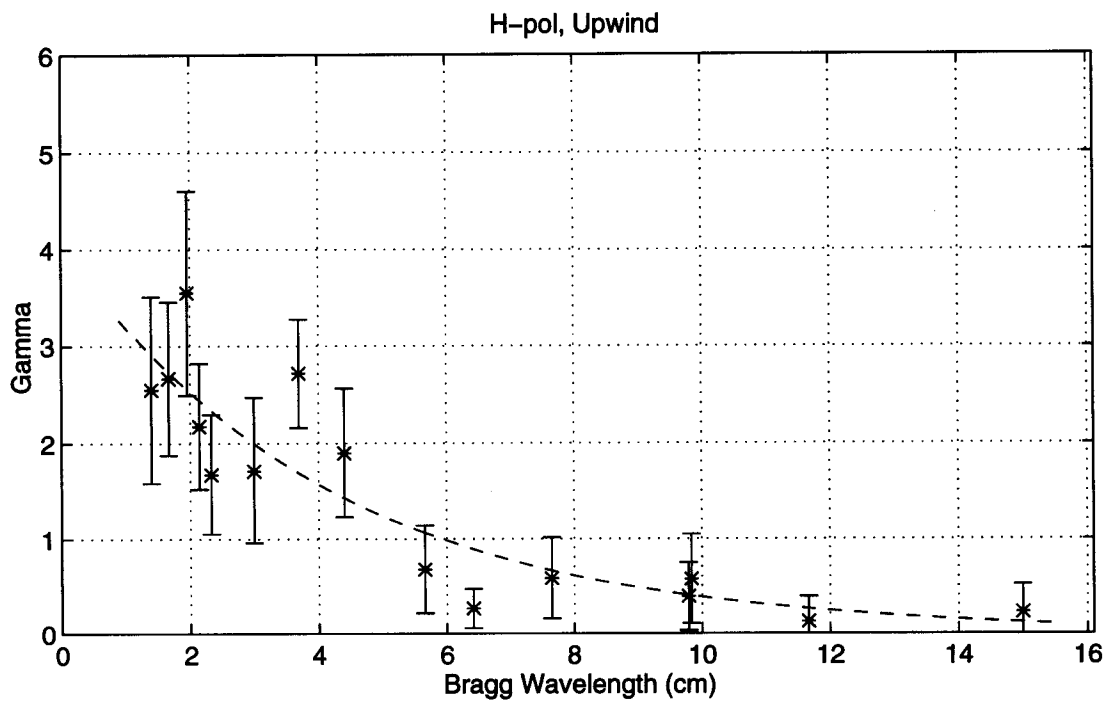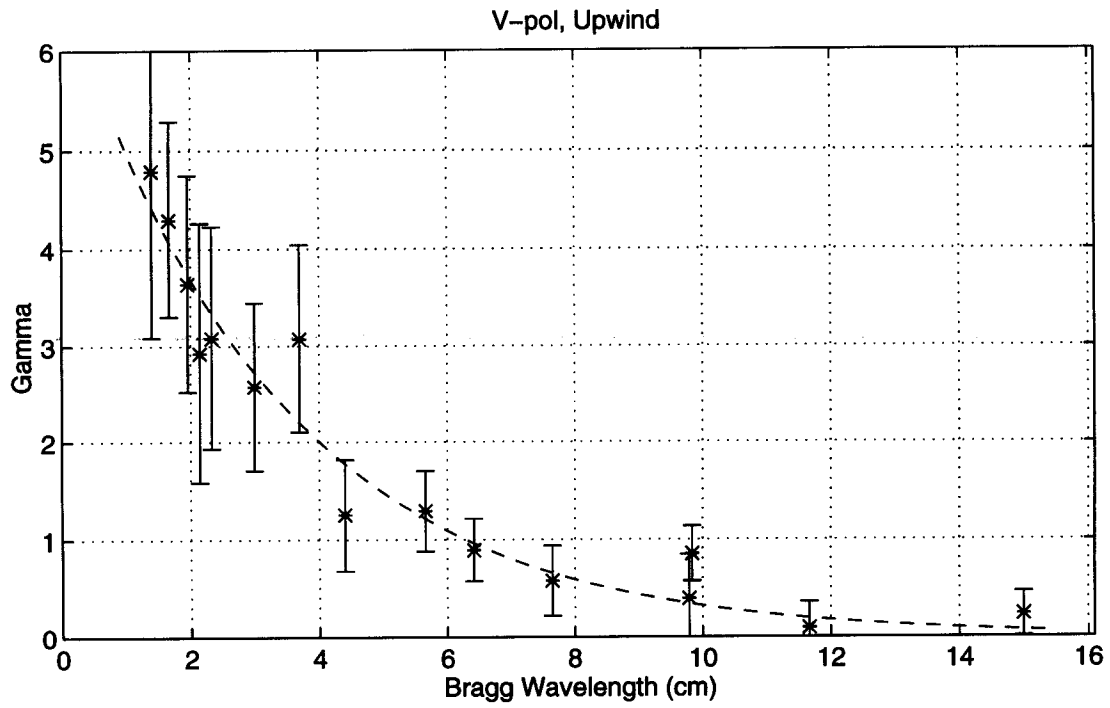
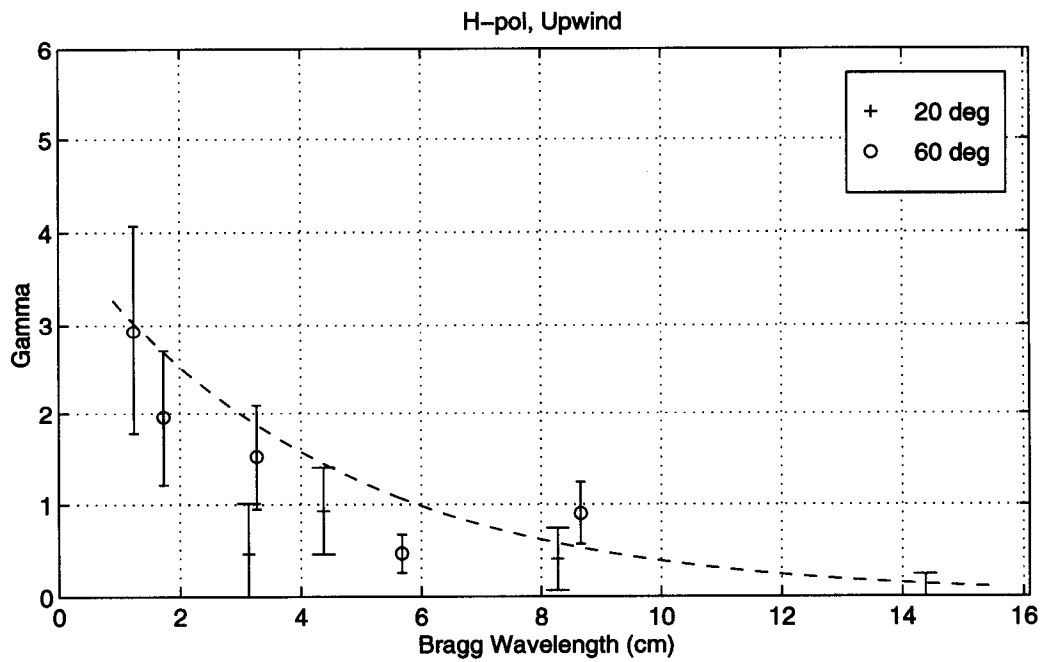Figure 5.12: Wind Exponent (γ) as function of Bragg wavelength for upwind. The dashed line is the least squares exponential fit to the data. Only incidence angles from 30° to 50° are included.

at 20° and 60° fall within the scatter of the other points. With the exception of V-pol upwind, the exponents for 20° do not rise as steeply with decreasing Bragg wavelength. This result supports the fact that the scattering mechanism at 20° is not purely Bragg.

Figure 5.15 displays the comparison between wind exponents calculated from Y-Scat data to those found with other experiments. Note that only an upwind comparison is shown, as only a few results from other experiments at downwind are available. In the V-pol case, Y-Scat values are greater than all others for $\Lambda < 4cm$. For H-pol the wind exponents are more comparable to the other results. The fact that Y-Scat measurements were taken in a fresh water lake rather than in the open ocean may explain why the exponents are higher. Not only are the water properties different, but in the lake the waves are developing, where as in the ocean they are more developed. A previous experiment on the CCIW Research Tower (WAVES 87) [12] found that σ^o measured at Lake Ontario had a higher wind speed dependence than previous results. Analyzing this data Colton [12] hypothesized that the higher wind speed exponents could be attributed to the difference between the drag coefficient of the open sea and that of Lake Ontario. The drag coefficient on the lake has a higher wind speed dependence because lake waves are often in an active growth stage and are steeper than waves in the ocean. Correcting for the assumed difference in drag coefficient, Colton showed that the wind exponents at 40° and 60° incidence angle decreased by almost a factor of 2. Since wind stress measurements are not currently available, the Y-Scat measurements can not be similarly rescaled. However, it is assumed that they would also decrease and be in better agreement with other results.

Both the data from Masako et al. [11] and Unal el al. [22] suggest that γ does not always increase as the Bragg wavelength decreases, but rather decreases as Λ becomes less than 2 cm. A previous deployment of Y-Scat [23] at higher incidence angles showed the same trend for γ . A drop in γ can possibly be explained physically by the fact that for very small waves (purely capillary) the viscous and dissipative effects become more important. As a result the waves are not as sensitive to changes in the wind speed [23]. For the present experiment, the H-pol data hint that γ decreases for $\Lambda < 2cm$. However, the V-pol data do not show any decrease. Therefore from just the current Y-Scat data, it is difficult to

Figure 5.13: Wind Exponent (γ) as function of Bragg wavelength for downwind. The dashed line is the least squares exponential fit to the data for 30° to 50°.
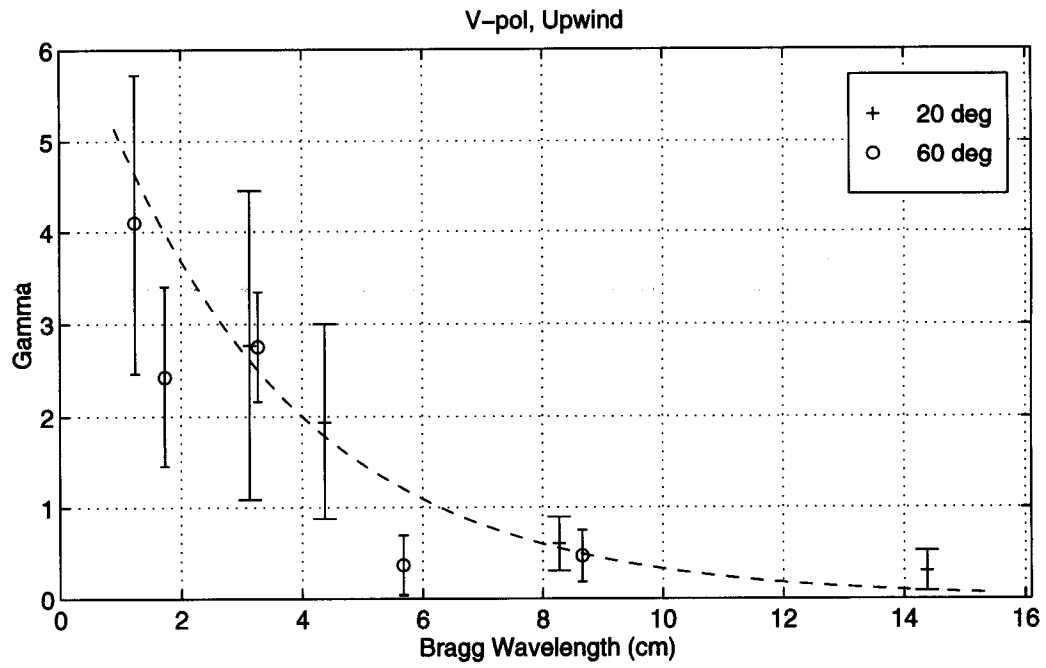
Figure 5.14: Wind Exponent (γ) as function of Bragg wavelength. The dashed line is the least squares exponential fit to the data from 30° to 50° only.
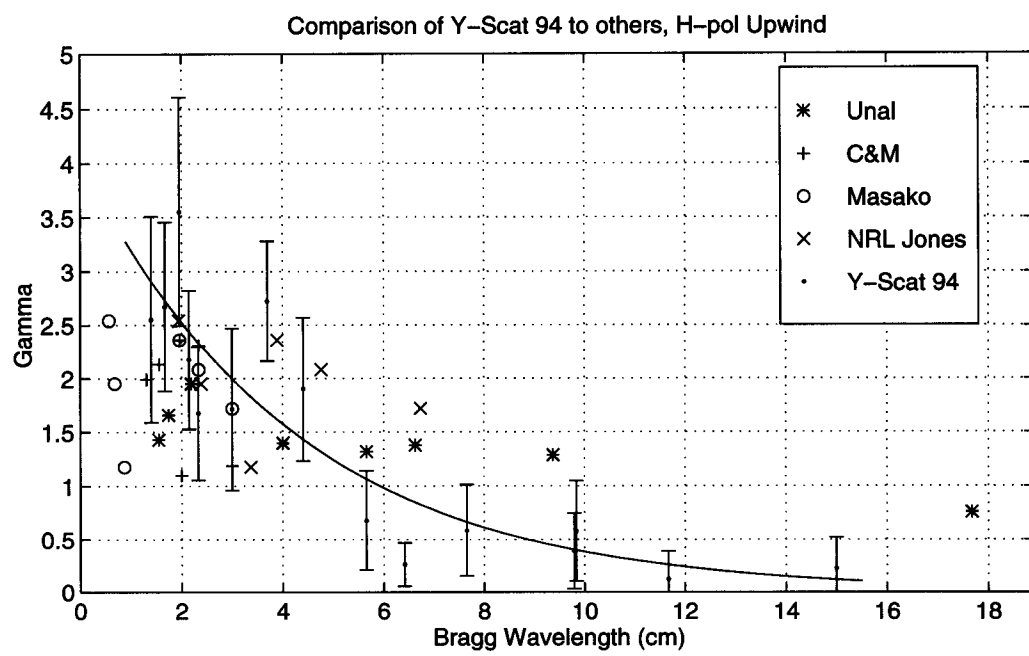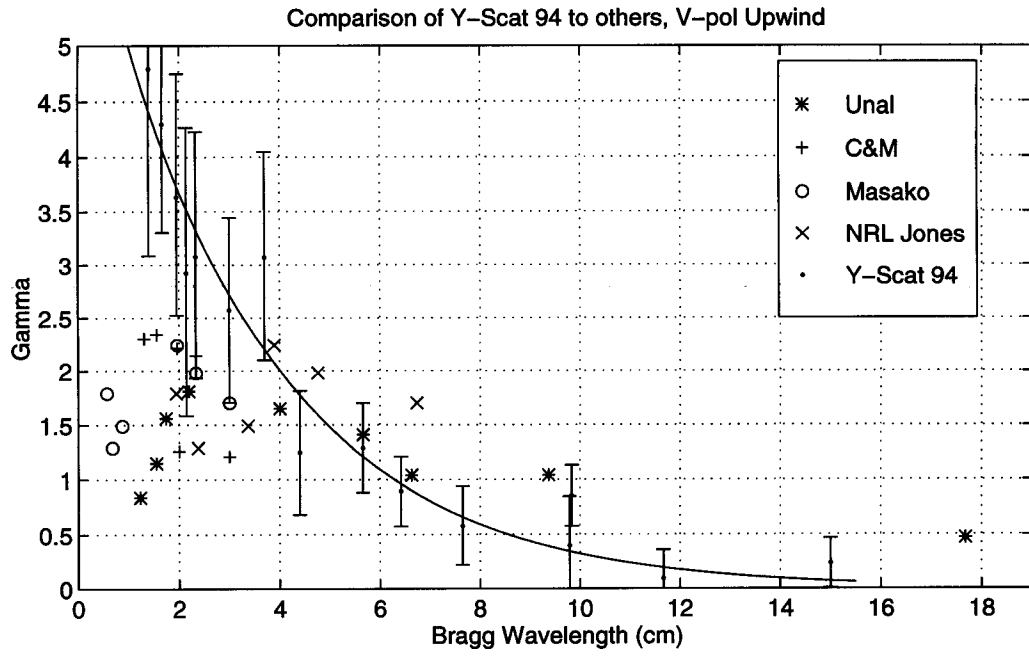
Figure 5.15: Comparison of Y-Scat wind speed exponents to others.

determine whether γ decreases for very short Bragg wavelengths. Nevertheless, it is assumed that the exponential least squares fit is only valid for Bragg wavelengths greater than 2 cm. Further research to resolve this question is needed.

5.3.2 Differences in γ for Upwind (γ_U), Downwind (γ_D), H-pol (γ_{HH}), and V-pol(γ_{VV})

To examine the dependence of γ on polarization, the H-pol γ (denoted γ_{HH}) is plotted against the V-pol γ (denoted γ_{VV}) for both upwind and downwind (see top 2 plots of Fig. 5.16). The dotted line represents a perfect agreement between the two polarizations, while the solid line is a least squares 2nd order polynomial fit. For low γ, the points are close to the 45° line. However, as γ increases, γ_{VV} dominates γ_{HH}. This trend is strongest at upwind, and suggests that V-pol is more sensitive to wind speed than H-pol.

The lower two plots of Figure 5.16 show the comparison between γ at upwind (denoted γ_U) and γ for downwind (denoted γ_D) for both V-pol and H-pol. The V-pol case suggests that γ_D is slightly larger than γ_U, while at H-pol γ_D is always larger than γ_U. As will be shown later, the difference between γ_U and γ_D has implications regarding the upwind/downwind ratio. In both cases γ_D is typically larger than γ_U. Since larger γ are associated with smaller Bragg wavelengths, this result suggests that for smaller Bragg wavelengths H-pol has a greater change in the upwind/downwind ratio than V-pol as a function of wind speed.

The ratios of γ_U to γ_D for both V-pol and H-pol as a function of Bragg wavelength are given in top plot of Figure 5.17. The dashed and solid lines are least squares fit to the data. Note that in both cases the γ_U/γ_D ratio is less than one, but increasing with decreasing Bragg wavelength. This implies that shorter Bragg wavelengths will produce a higher upwind/downwind ratios. The lower plot of Figure 5.17 illustrates the γ_{HH}/γ_{VV} ratio as function of Bragg wavelength. An important result is that for small Bragg wavelengths, V-pol is more sensitive to wind speed, particularly for upwind. As the Bragg wavelength increases the difference between the two is reduced.
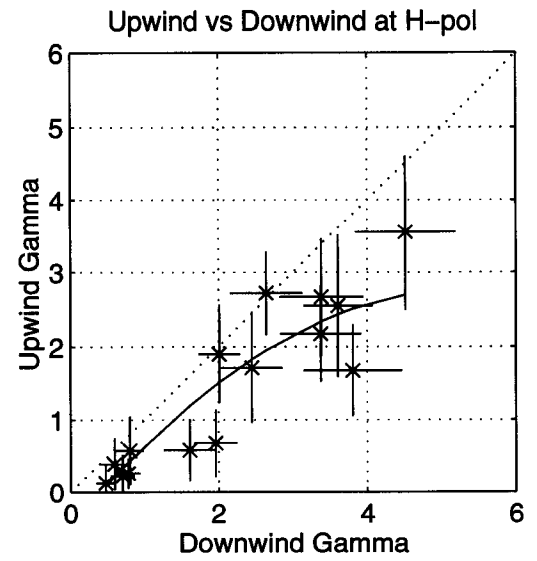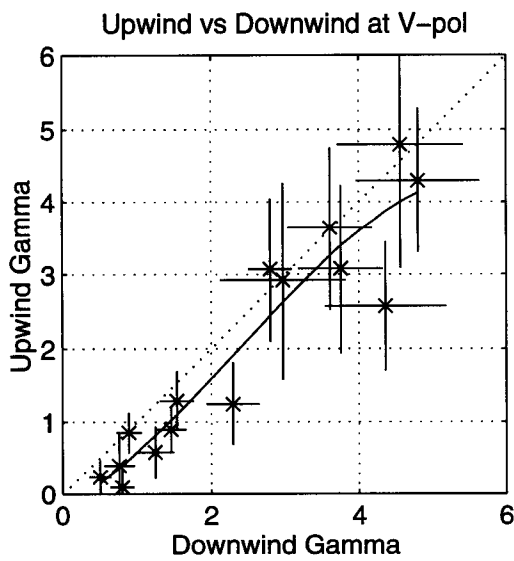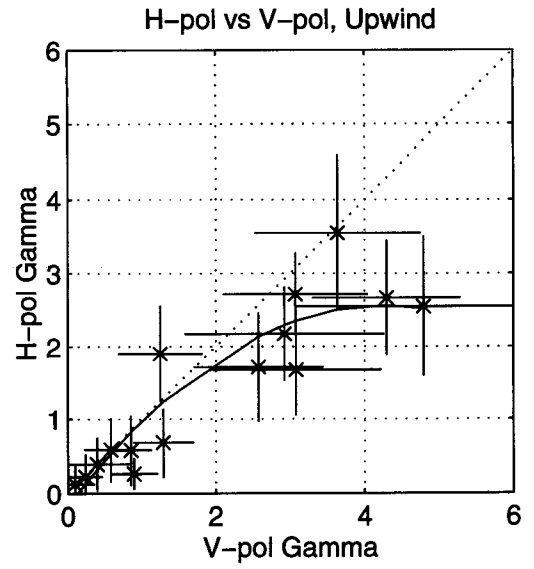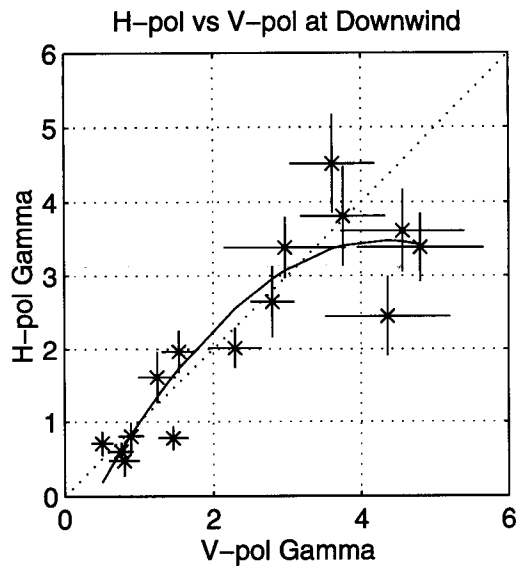
Figure 5.16: Comparison of γ_{HH} to γ_{VV} and γ_U to γ_D.
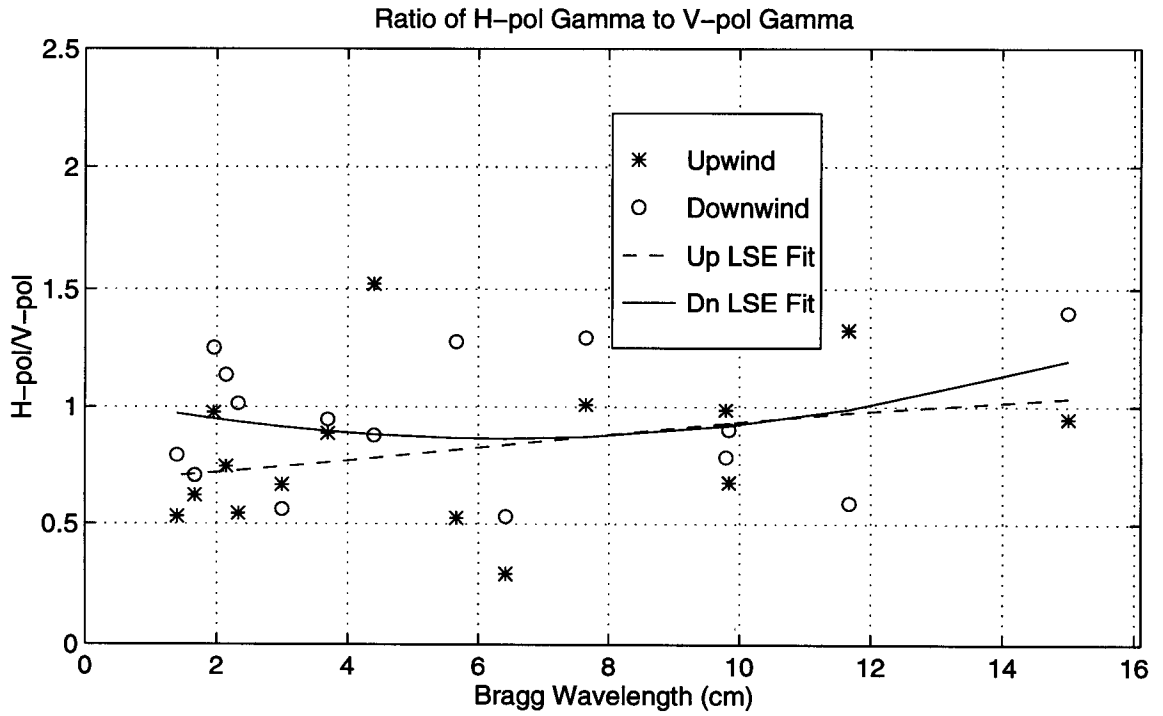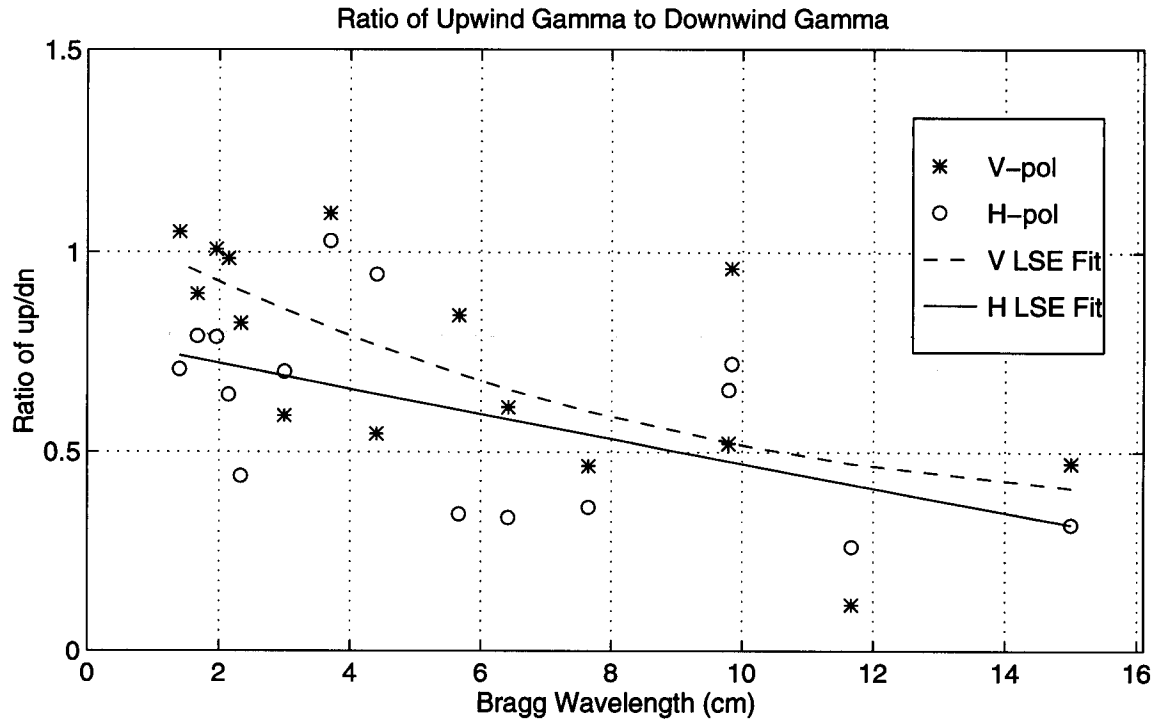
Figure 5.17: γ_{HH}/γ_{VV} ratio and γ_U/γ_D ratio as function of Bragg wavelength.

5.3.3 Upwind Downwind Ratio

Using the linear regression fit, the upwind/downwind (u/d) ratio of σ^o can be found for a given wind speed (U) from the following equation

$$(\sigma_U^o/\sigma_D^o)_{dB} = (\sigma_U^o)_{dB} - (\sigma_D^o)_{dB} = A_U - A_D + (\gamma_U - \gamma_D)10log(U) \qquad (5.2)$$

where A_U and A_D are the y-intercepts for upwind and downwind cases respectively. The u/d ratio is independent of the calibration accuracy. However the results are sensitive to the linear regression technique used. Note that the u/d ratio is a function of wind speed. Figures 5.18 thru 5.20 give the u/d ratio for U ranging from 5-10 m/s. The solid lines in each figure give the least squares polynomial fit to the data. A first order polynomial is used for the V-pol cases, while a third order polynomial is used for the H-pol cases. The H-pol results show a definite trend of increasing u/d ratio for decreasing Bragg wavelengths. Though the ratio is less than that for H-pol, the V-pol u/d ratios generally increase as Bragg wavelengths decrease. In all instances, the H-pol u/d ratios are higher than V-pol. For both the V-pol and H-pol cases, the u/d ratios decrease as the wind speed increases.

Other researchers have found similar results regarding the differences in H-pol and V-pol ratios as well as the increase in u/d with decreasing Bragg wavelength. A brief summary of these results are now presented. Using a C-band V-pol radar, Feindt et al. [5] found that u/d varies between 0 and 2 dB, but they found no systematic dependence on wind speed. However, using data from Jones and Schroeder [5], Feindt et al. did see a slight increase in u/d with decreasing Bragg wavelength. Masako et al. [11] at X-band reported that for V-pol, u/d varied from .42 to 2.01 over the incidence angle range of 32° to 52°. For H-pol over the same incidence range the u/d ratio was approximately 2.5 dB. Therefore, their results also show that H-pol u/d is larger than the V-pol case. These reported values of u/d are averaged over a wind speed range of 3 -17 m/s, but they state that above 7-9 m/s the u/d ratios appear to decrease with increasing wind speed and become less than unity (0 dB) for high wind speed cases. Unal et al. [22] reported u/d results for both V-pol and H-pol at a wind speed of 10 m/s and incidence angles of 30° and 45°. In summary, Unal et al. found that H-pol was larger than V-pol, and that u/d increased with incidence angle, which at a given

frequency, is equivalent to decreasing Bragg wavelength. They also reported that the difference between H-pol and V-pol u/d decreased with increasing wind speed.

A difference between Y-Scat results and those just mentioned is that some of the values of u/d ratios calculated with Y-Scat data for V-pol are less than unity. This mainly occurs at higher wind speeds and for longer Bragg wavelengths. Both of these factors are consistent with the trends of decreasing u/d with increasing Bragg wavelength and decreasing u/d with increasing wind speed. In summary, the behavior of the u/d ratio as a function of polarization, Bragg wavelength, and wind speed found with Y-Scat data is in good agreement with previous results.
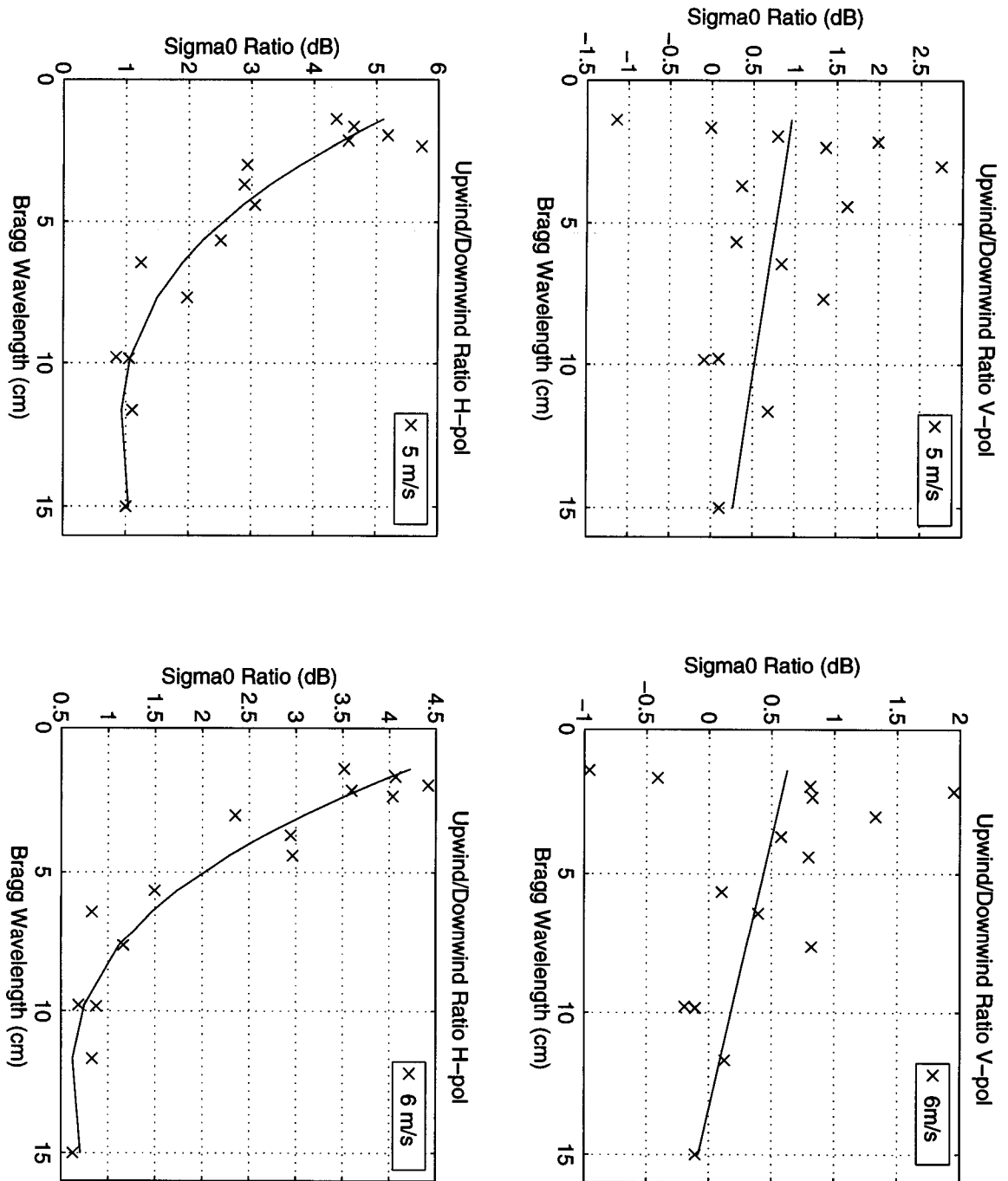
Figure 5.18: Upwind/Downwind ratio as function of Bragg wavelength for U = 5 and 6 m/s.
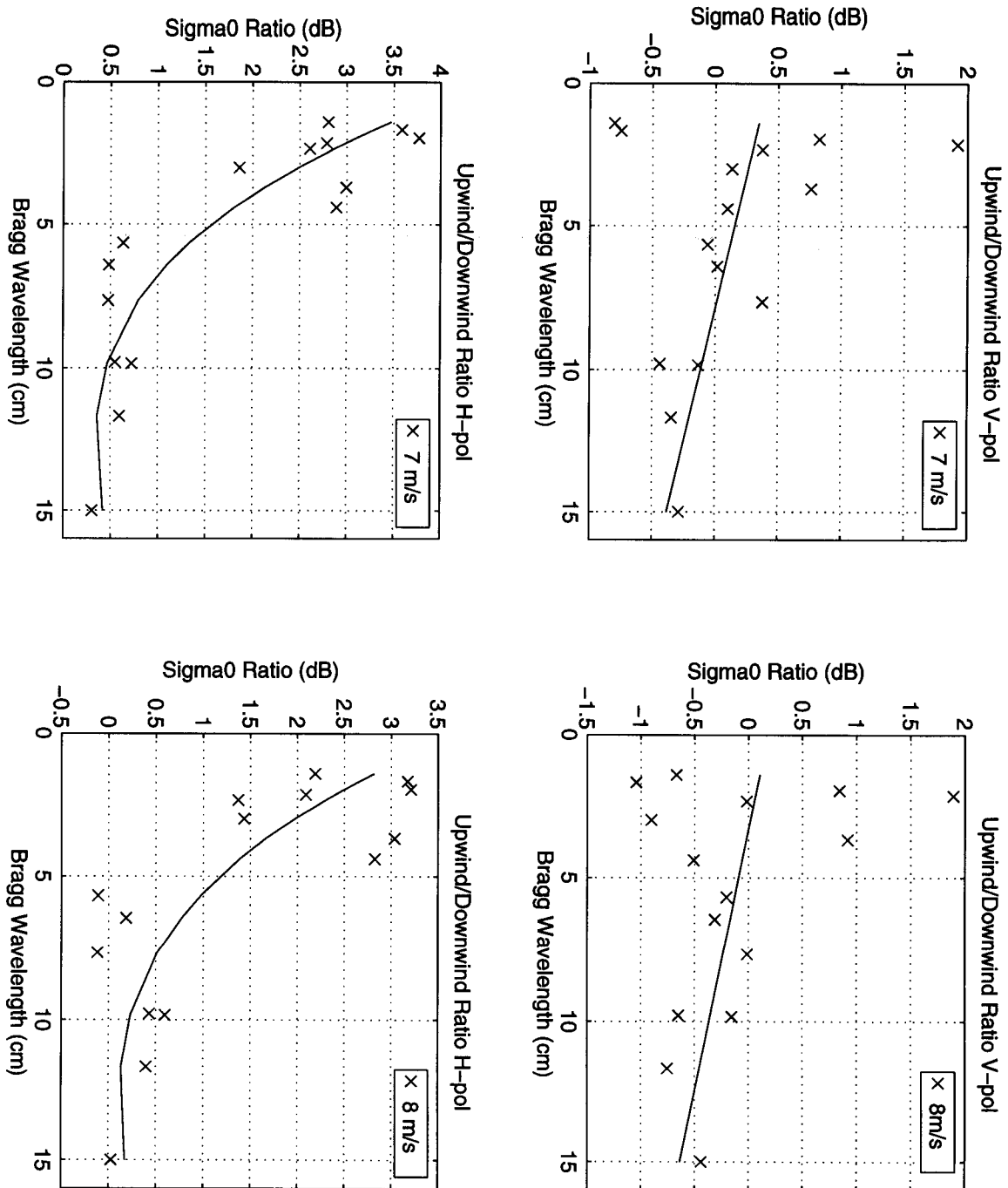
Figure 5.19: Upwind/Downwind ratio as function of Bragg wavelength for U = 7 and 8 m/s.
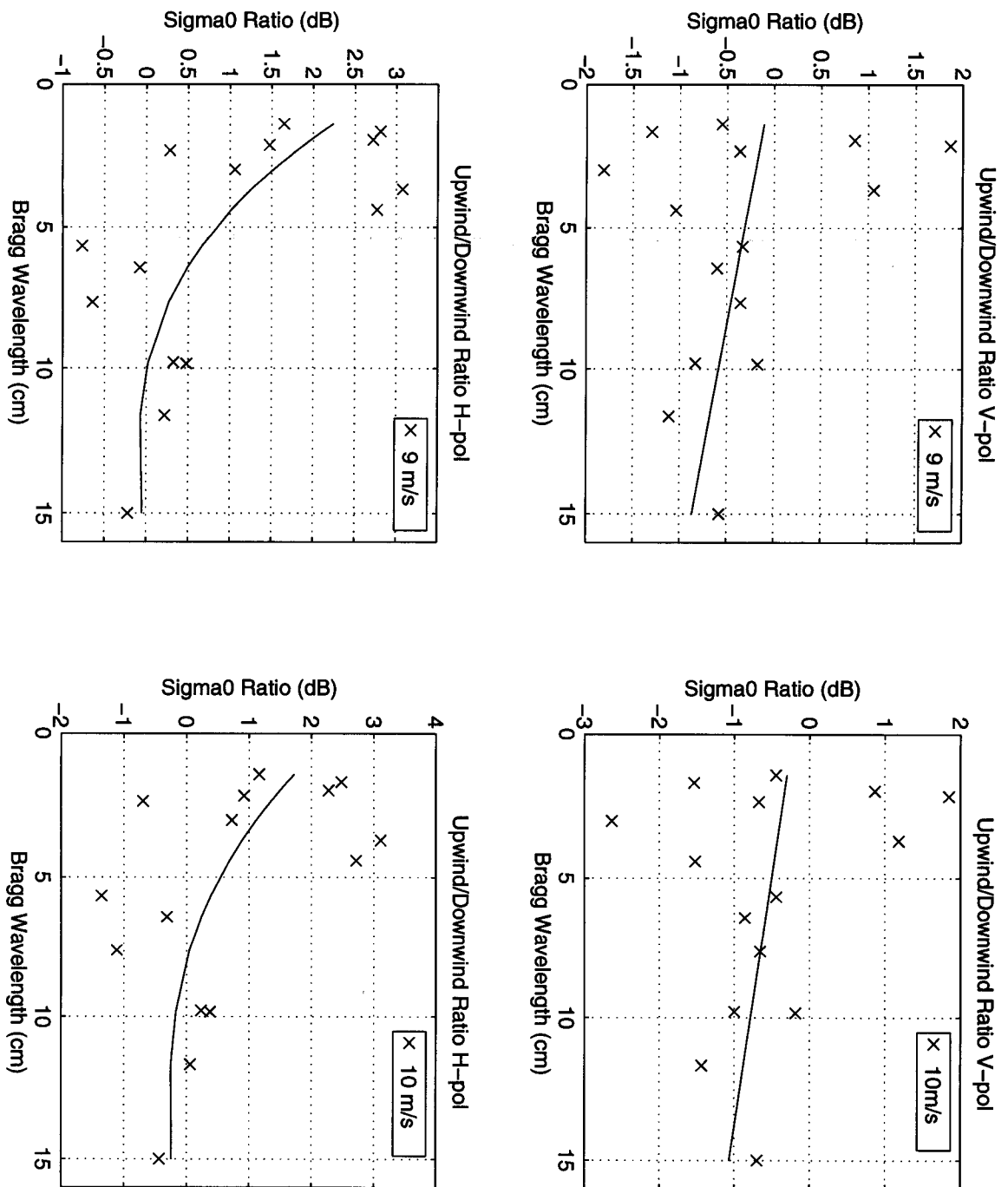
Figure 5.20: Upwind/Downwind ratio as function of Bragg wavelength for U = 9 and 10 m/s.

5.4 Summary of Results and Discussion

To summarize, this section presents the least squares fits derived in the previous section and discusses their implications to scatterometery.

The upper plot of Figure 5.21 gives γ as a function of Bragg wavelength for all cases previously analyzed. The results for all cases are similar, with the exception of the H-pol upwind case which deviates the most from the mean. The curves imply that σ^o_{VV} is more sensitive to wind speed than σ^o_{HH}. An additional conclusion is that smaller Bragg wavelengths (less than 4 cm) are much more sensitive to wind speed than are the longer ones. Other experimental results imply that the sensitivity begins to drop off for Bragg wavelengths somewhere less than 2 cm. However, Y-Scat data only provides limited samples of Λ less than 2 cm and can not support this conclusion.

The lower plot of Figure 5.21 displays the γ_U/γ_D and γ_{HH}/γ_{VV} ratios as a function of Bragg wavelength. The γ_{HH}/γ_{VV} ratios exhibit a decreasing trend with decreasing Bragg wavelength. For the wind speed sensitive wavelengths (2 - 4 cm), γ_{HH}/γ_{VV} ratio is less than unity which suggests that γ_{VV} is more sensitive to wind speed. Both the γ_U/γ_D ratios increase with decreasing Bragg wavelength. Notice that for Λ less than 4 cm, γ_U/γ_D for V-pol approaches unity while γ_U/γ_D for H-pol is lower. This result implies that the upwind/downwind ratio of σ^o for H-pol will have a greater change as a function of wind speed.

Figure 5.22 presents u/d ratios for V-pol (denoted u/d_{VV}) and H-pol (denoted u/d_{HH}) at 4 different wind speeds. In both cases two trends are apparent. The first is that the u/d ratio increases with decreasing Bragg wavelength, and the second is that the u/d ratio decreases with increasing wind speed. The first result implies that shorter Bragg wavelengths are more sensitive to relative azimuth (wind direction) than are longer wavelengths. Another important observation is that u/d_{HH} is higher at all wind speeds than u/d_{VV}. This suggests that σ^o_{HH} is more sensitive to wind direction than σ^o_{VV}.

Now consider a spaceborne scatterometer. Practical reasons such as cost and complexity imply that it should be a single frequency radar. Moreover, the incidence angle covers moderate Bragg scattering regions. Given this system, what should the operating frequency be? The top plot of Figure 5.23 illustrates
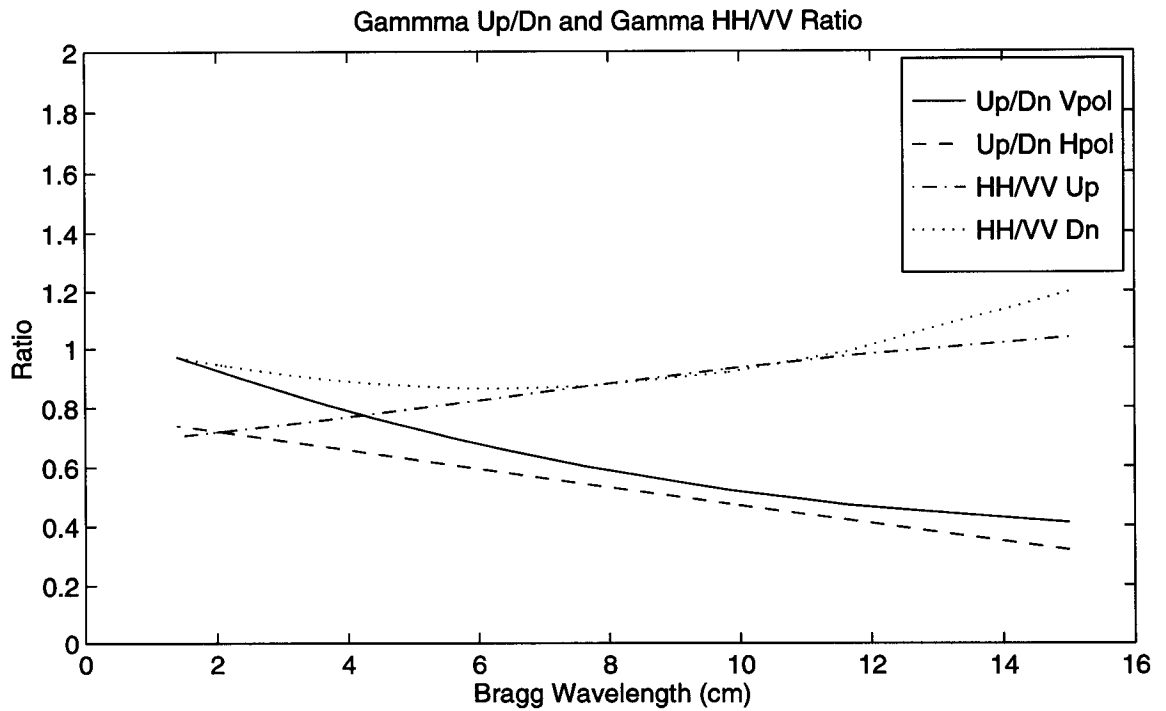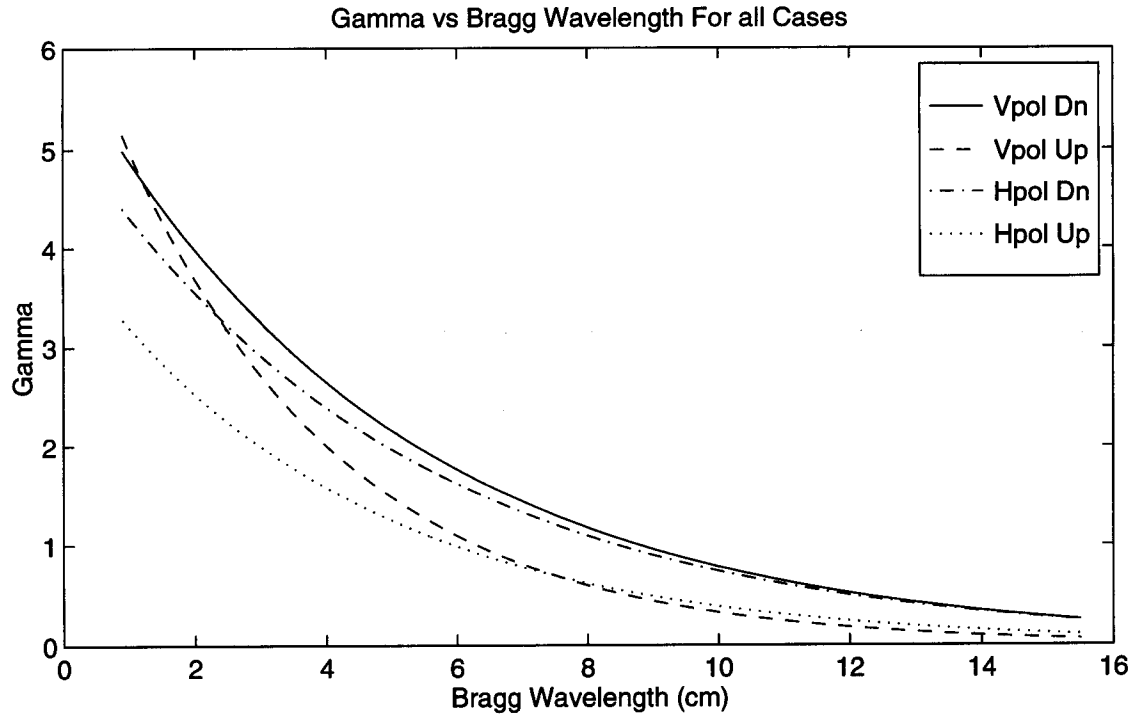
Figure 5.21: Top: Wind speed exponents (γ) as a function of Bragg wavelength. Bottom: Ratios of γ_U/γ_D and γ_{HH}/γ_{VV} as a function of Bragg wavelength.
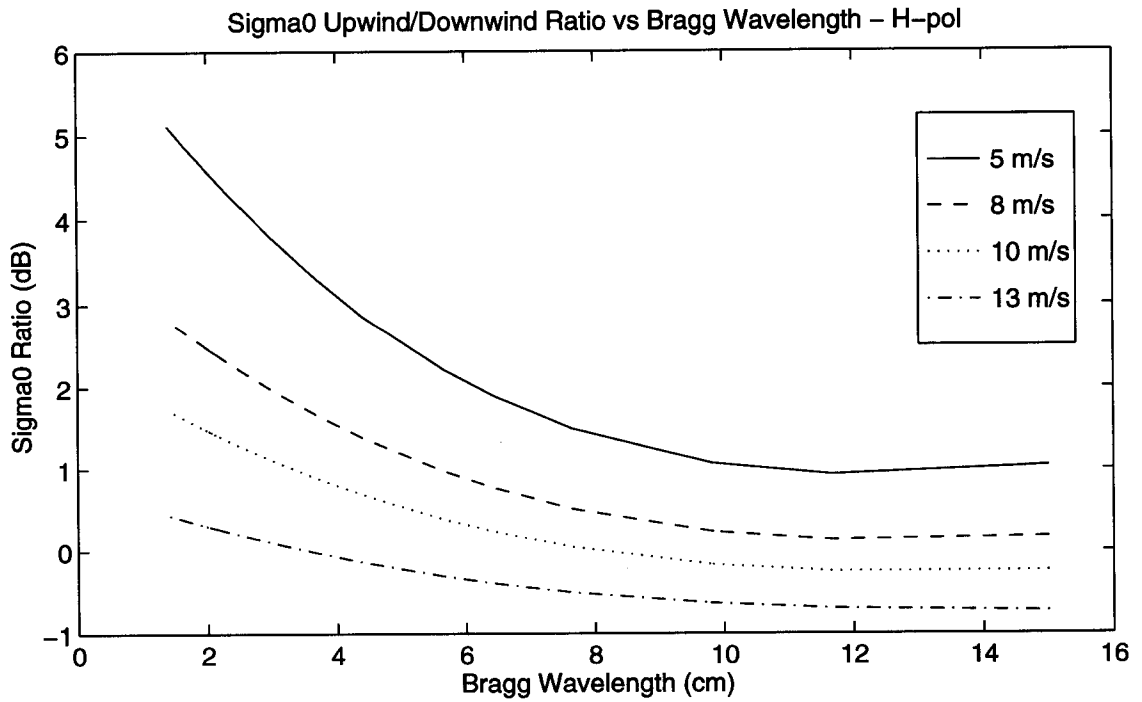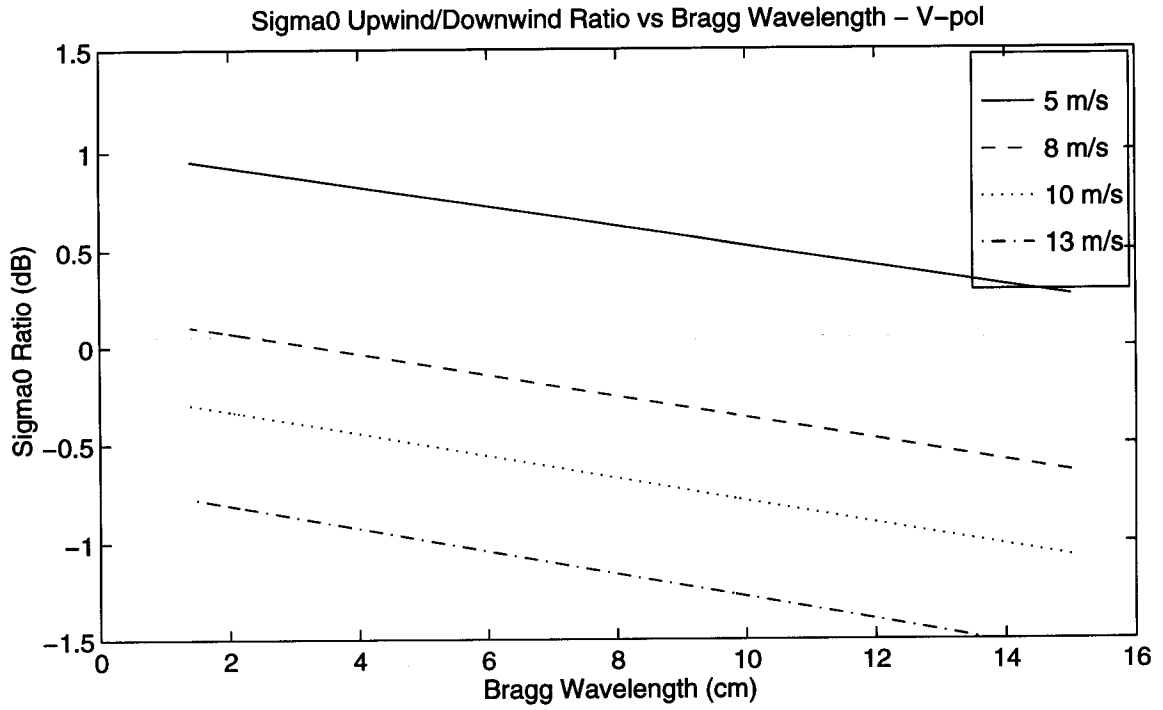
Figure 5.22: σ^o upwind/downwind ratio as function of Bragg wavelength for wind speeds of 5, 8, 10, and 13 m/s.

graphically which Bragg wavelengths are attainable at moderate incidence angles for a range of frequencies. Notice that only frequencies higher than C-band produce Bragg wavelengths less than 5 cm. The bottom plot shows the most common scatterometer frequencies at C-band, X-band, and Ku-band. In this plot horizontal dotted lines ($\Lambda = 2, \Lambda = 4$) have been added to emphasize the region where σ^o is most sensitive to wind speed, while the vertical dotted lines ($\theta = 30, \theta = 50$) highlight the incidence angle range used in this study. The results presented in this chapter have shown that σ^o is most sensitive to wind speed and has a higher u/d ratio for short Bragg wavelengths. Given this, Figure 5.23 suggests that either Ku-band or X-band is a better operational frequency than C-band. From the results of this study, it is difficult to further distinguish between X-band and Ku-band.

Although σ^o at X-band and Ku-band appears to be more sensitive to wind speed and direction than at C-band, the values of σ^o at the higher frequencies also exhibit much higher variability. This variability may be due to other unmodeled parameters such as air-sea temperature difference and long wave fields. In this respect, C-band is a better operational frequency since the measurements appear to be less sensitive to other environmental parameters. Accounting environmental parameters such as air-sea temperature differences and long wave fields on a global scale may be very difficult in an operational system and would require a better understanding of these effects than is presently available.

Regarding polarization, V-pol appears to be slightly more sensitive to wind speed, but H-pol is much more sensitive to wind direction. In addition the measurement variability at 10 GHz and 14 GHz is lower for the H-pol cases. These results suggest that H-pol is better than V-pol in determining both wind speed and direction, while V-pol appears superior in measuring wind speed only. It should be noted that these conclusions are based only on Y-Scat 94 data. However, such data is generally consistent with results published by other researchers.
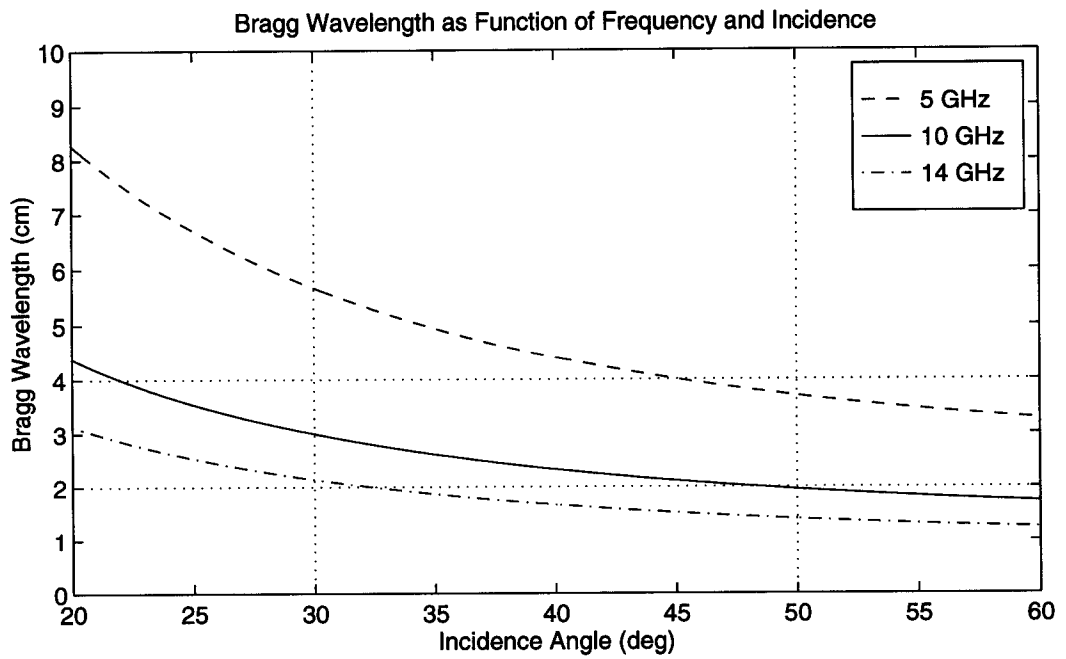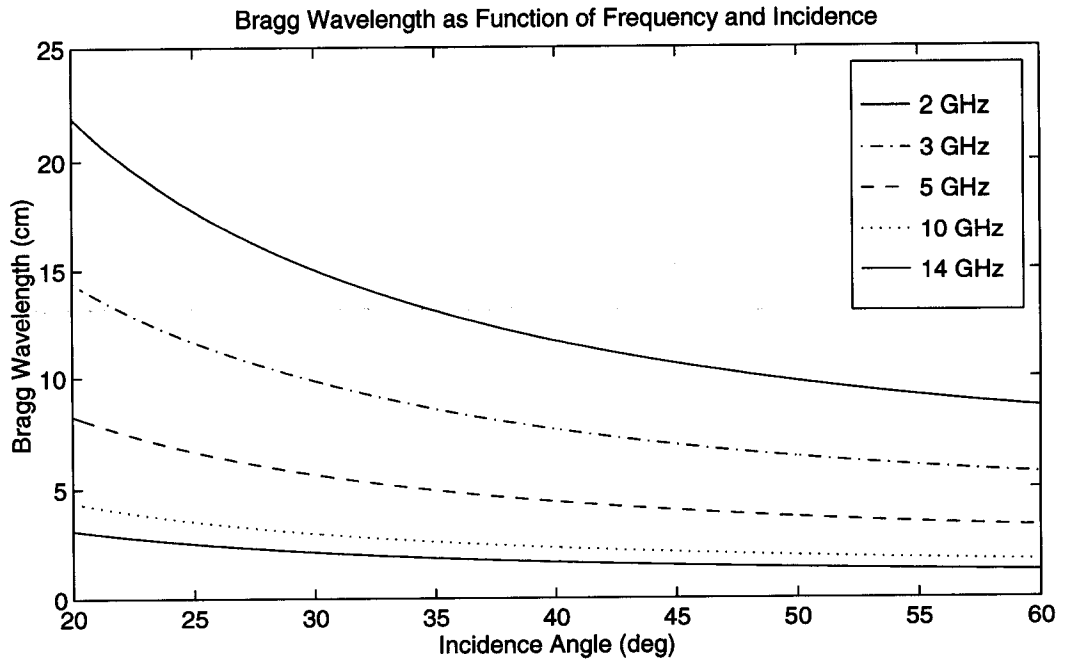
Figure 5.23: Bragg wavelengths as a function of both frequency and incidence angle. In the bottom plot the dotted lines have been added to emphasize regions of Bragg wavelengths and incidence angles.

CHAPTER 6

CONCLUSIONS

6.1 Experiment Summary

An ultra-wideband scatterometer, Y-Scat, has been developed, tested, and is currently deployed on the CCIW Research Tower. Also deployed on the tower are an array of environmental sensors including 2 anemometers, a bivane anemometer, an air temperature sensor, a water temperature sensor, a rain gauge, a humidity gauge, and a wave staff array. Together with the weather sensors data, Y-Scat data is being collected to support a variety of ocean scattering studies. Using the data set currently available, this thesis investigates the wind speed and direction sensitivity of the normalized radar cross section (σ^o).

6.2 Data Analysis Summary

The data set taken from approximately May 6th - Aug 1st is edited to eliminate data corrupted by rain and radar system anomalies. Both manual and automated data editing techniques are implemented. Using the edited data set, the measurements are binned according to frequency, polarization, and incidence angle. The data are further binned by relative azimuth in 20° increments and wind speed. Only measurements corresponding to upwind or downwind directions and wind speeds higher than 4.5 m/s are analyzed in this thesis.

Assuming a power law relation between σ^o and wind speed, least squares linear regression is computed to determine the wind speed exponent (γ) for each frequency, polarization, incidence angle, and relative azimuth direction. To improve the regression fit, statistical outliers are removed. Outliers are defined as points that are +/- 2σ away from the initial regression fit. It is shown that the resulting slopes are not heavily dependent on the outlier criteria chosen.

Each data point consists of a minimum of 600 .1 sec measurements which are averaged together in normal space. Averaging reduces the statistical uncertainty. This uncertainty is quantified by calculating 95% confidence intervals

assuming that half of the .1 sec measurements are independent. In most instances the error bars are less than +/-1 dB.

6.3 Results Summary

The wind speed exponent (γ) is examined as both a function of incidence angle and Bragg wavelength. The plots of γ versus incidence angle (θ) show that γ typically increases with increasing θ from 20° to 50°. Most cases display a peak in γ at 50°, however, the results at 2 GHz do not show any apparent dependence on θ. As a function of Bragg wavelength (Λ), all results show that γ increases with decreasing Λ. In comparison to previous studies, γ is much higher for small Λ especially at V-pol. This difference may be attributed to differences in the drag coefficient of Lake Ontario and that of the open ocean.

Using the regression fits, the upwind/downwind (u/d) ratio of σ^o is determined as a function of wind speed and Bragg wavelength. The data display two important trends. First, the u/d ratio increases with decreasing Λ and second, the u/d ratio decreases with increasing wind speed. These trends are consistent with results published by other researchers.

Using a least squares exponential or polynomial fit the behavior of γ and u/d are compared. Analysis of these comparisons gives the following conclusions:

- V-pol σ^o is slightly more sensitive than H-pol σ^o to wind speed.

- H-pol σ^o is more sensitive than V-pol σ^o to wind direction.

- Bragg wavelengths less than 4 cm are the most sensitive to wind speed and direction.

- H-pol u/d ratio is larger than the u/d ratio at V-pol.

- For small Λ the H-pol u/d ratio has a greater change as a function of wind speed than V-pol u/d ratio.

Based on the sensitivity analysis, it is concluded that X-band and Ku-band are better operating frequencies than C-band. However, the data also suggest that in addition to wind speed and direction, X-band and Ku-band are more affected more

by other unmodeled environmental parameters than is C-band. In this respect C-band may be a better operating frequency.

6.4 Suggestions For Further Research

In this thesis only 3 months (May - July) of data currently available are analyzed. The remainder of the deployment will provide approximately 3 additional months of data. This will provide an excellent opportunity to confirm or extend the conclusions presented in this thesis. Furthermore, wind stress measurements will be available for analysis along with wind speed. Given the expanded data set, suggestions for further research are:

- Re-analyze the complete data set according to the methods presented in this thesis.

- If possible, further stratify the data according to air-sea temperature difference and long wave field to see if these parameters account for the higher variability at X-band and Ku-band.

- Using the wind stress measurements rescale the wind speed exponents to the drag coefficient of the open ocean.

- Compute the regression of σ^o against wind friction velocity instead of wind speed and compare the R^2 coefficients to determine which method gives a better fit to the data.

- Using a higher operating frequency of Y-Scat (e.g. 17 GHz), determine if γ does drop off for small Bragg wavelengths.

BIBLIOGRAPHY

[1] N. B. Ingelby and R. A. Bromley, "A Diagnostic Study of the Impact of Seasat Scatterometer Winds on Numerical Weather Prediction," *Monthly Weather Reveiw*, vol. 119, pp. 84–103, January 1991.

[2] W. J. P. Jr., "Examples of, Reasons for, and Consequences of the Poor Quality of Wind Data From Ships for the Marine Boundary Layer: Implications for Remote Sensing," *Journal of Geophysical Research*, vol. 95, pp. 13,313–13,340, August 1990.

[3] F. Naderi, M. H. Frelich, and D. G. Long, "Spaceborne Radar Measurement of Wind Velocity Over the Ocean–An Overview of the NSCAT Scatterometer System," *Proceedings of the IEEE*, vol. 79, pp. 850–866, June 1991.

[4] A. H. Chaudhry and R. K. Moore, "Tower-Based Backscatter Measurements of the Sea," *IEEE Journal of Oceanic Engineering*, pp. 309–316, December 1984.

[5] F. Feindt, V. Wismnn, W. Alpers, and W. C. Keller, "Airborne Measurements of the Ocean Radar Cross Section at 5.3 GHz as a Function of Wind Speed," *Radio Science*, vol. 21, pp. 854–856, September-October 1986.

[6] W. C. Keller, W. J. Plant, and D. E. Weissman, "The Dependence of X Band Microwave Sea State Return on Atmospheric Stability and Sea State," *Journal of Geophysical Research*, vol. 90, pp. 1019–1029, January 1985.

[7] W. C. Keller, V. Wisman, and W. Alpers, "Tower-Based Measurements of the Ocean C Band Radar Backscattering Cross Section," *Journal of Geophysical Research*, vol. 94, pp. 924–930, September 1989.

[8] M. R. Keller, W. C. Keller, and W. J. Plant, "A Wave Tank Study of the Dpendence of X Band Cross Sections on Wind Speed and Water Temperature," *Journal of Geophysical Research*, vol. 97, pp. 5771–5792, April 1992.

[9] D. E. Weissman, K. L. Davidson, R. A. Brown, C. A. Friehe, and F. Li, "The Relationships Between the Microwave Radar Cross Section and both Wind Speed and Stress - Model Function Development Using Fasinex Data," *Journal of Geophysical Research*, vol. 94, pp. 924–930, September 1992.

[10] W. C. Keller and W. J. Plant, "Cross Sections and Modulation Transfer Functions at L and Ku Bands Measured During the Tower Ocean Wave and Radar Dependence Experiment," *Journal of Geophysical Research*, vol. 95, pp. 16,277 – 16,289, September 1990.

[11] H. Masuko, K. Okamoto, M. Shimada, and S. Niwa, "Measurement of Microwave Backscattering Signatures of the Ocean Surface Using X Band and Ka Band Airborne Scatterometers," *Journal of Geophysical Research*, vol. 91, pp. 13,605–13083, 1986.

[12] M. C. Colton, *Dependence of Radar Backscatter on the Energetics of the Air-Sea Interface*. PhD thesis, Naval Postgraduate School, Monterey, CA, 1989.

[13] I. Tsanis and M. A. Donlean, "The WAVES Programme on the CCIW Research Tower," Tech. Rep. 87-65, National Water Research Institute (NWRI) Report, 1987.

[14] C. A. Ballanis, *Advance Engineering Electromagnetics*. New York, NY: John Wiley and Sons, 1989.

[15] F. T. Ulaby, R. K. Moore, and A. K. Fung, *Microwave Remote Sensing, Active and Passive*, vol. 2. Norwood, MA: Artech House Inc., 1981.

[16] F. J. Wentz, S. Peteherych, and L. A. Thomas, "A Model Function for Ocean Radar Cross Sections at 14.6 GHz," *Journal of Geophysical Research*, vol. 89, p. 3689, May 1984.

[17] W. L. Jones, L. C. Schroeder, D. H. Boggs, E. M. Bracalente, R. A. Brown, G. J. Dome, W. J. Pierson, and F. J. Wentz, "The SEASAT-A Satellite Scatterometer: The Geophysical Evaluation of Remotely Sensed Wind Vectors Over the Ocean," *Journal of Geophysical Research*, vol. 87, pp. 3297–3317, April 1982.

[18] M. A. Donlean and W. J. Pierson, "Radar Scattering and Equilibrium Ranges in Wind-Generated Waves With Application to Scatterometery," *Journal of Geophysical Research*, vol. 92, pp. 4971–5021, May 1987.

[19] P. M. Woicheshyn, M. G. Wurtele, D. H. Boggs, L. F. McGoldrick, and S. Peterherych, "The Necessity for a New Parameritization of an Empirical Model for Wind/Ocean Scatterometery," *Journal of Geophysical Research*, vol. 91, pp. 2273–2288, February 1986.

[20] S. L. Durden and J. F. Vesecky, "A Physical Radar Cross-Section Model for a Wind-Driven Sea with Swell," *IEEE Journal of Oceanic Engineering*, vol. 10, pp. 445–451, June 1985.

[21] W. J. Plant, "A Two-Scale Model of Short Wind-Generated Waves and Scatterometry," *Journal of Geophysical Research*, vol. 91, pp. 10,735–10,749, September 1986.

[22] C. M. H. Unal, P. Snoeji, and P. J. F. Swart, "The Polarization-Dependent Relation Between Radar Backscatter from the Ocean Surface and Surface Wind Vector at Frequencies Between 1 and 18 GHz," *IEEE Transactions on Geoscience and Remote Sensing*, vol. 29, pp. 621–626, July 1991.

[23] R. Reed, D. G. Long, D. V. Arnold, and R. S. Collyer, "Initial Results From the Deployment of an Ultra-Wide Band Scatterometer," in *Internationl Geoscience and Remote Sensing Symposium* (T. I. Stien, ed.), (Piscataway, NJ), pp. 799–801, IEEE, 1994.

[24] W. J. Plant, "A Relationship Between Wind Stress and Wave Slope," *Journal of Geophysical Research*, vol. 87, pp. 1961–1967, March 1982.

[25] A. T. Jessup, *Detection and Characterization of Deep Water Wave Breaking Using Moderate Incidence Angle Microwave Baclscatter from the Sea Surface.* PhD thesis, Massachusetts Intsititute of Technology, Cambridge, MA, 1990.

[26] S. Weisberg, *Applied Linear Regression.* New York, NY: John Wiley and Sons, 1980.

[27] J. S. Bendat and A. G. Piersol, *Random Data*. New York, NY: John Wiley and Sons, 1986.

[28] W. J. Plant, E. A. Terray, R. A. Petitt, and W. C. Keller, "The Dependence of Microwave Backscatter from the Sea on Illuminated Area: Correlation Times and Lengths," *Journal of Geophysical Research*, vol. 99, pp. 9705–9723, May 1994.

APPENDIX A

DATA AT UPWIND AND DOWNWIND

The figures on the following pages display plots of σ^o versus wind speed. The first five pages show all data at downwind with each page corresponding to a different frequency. The last five pages show the results at upwind. The linear fit is computed using the $+/- 2\sigma$ outlier removal technique as discussed in Chapter 4.
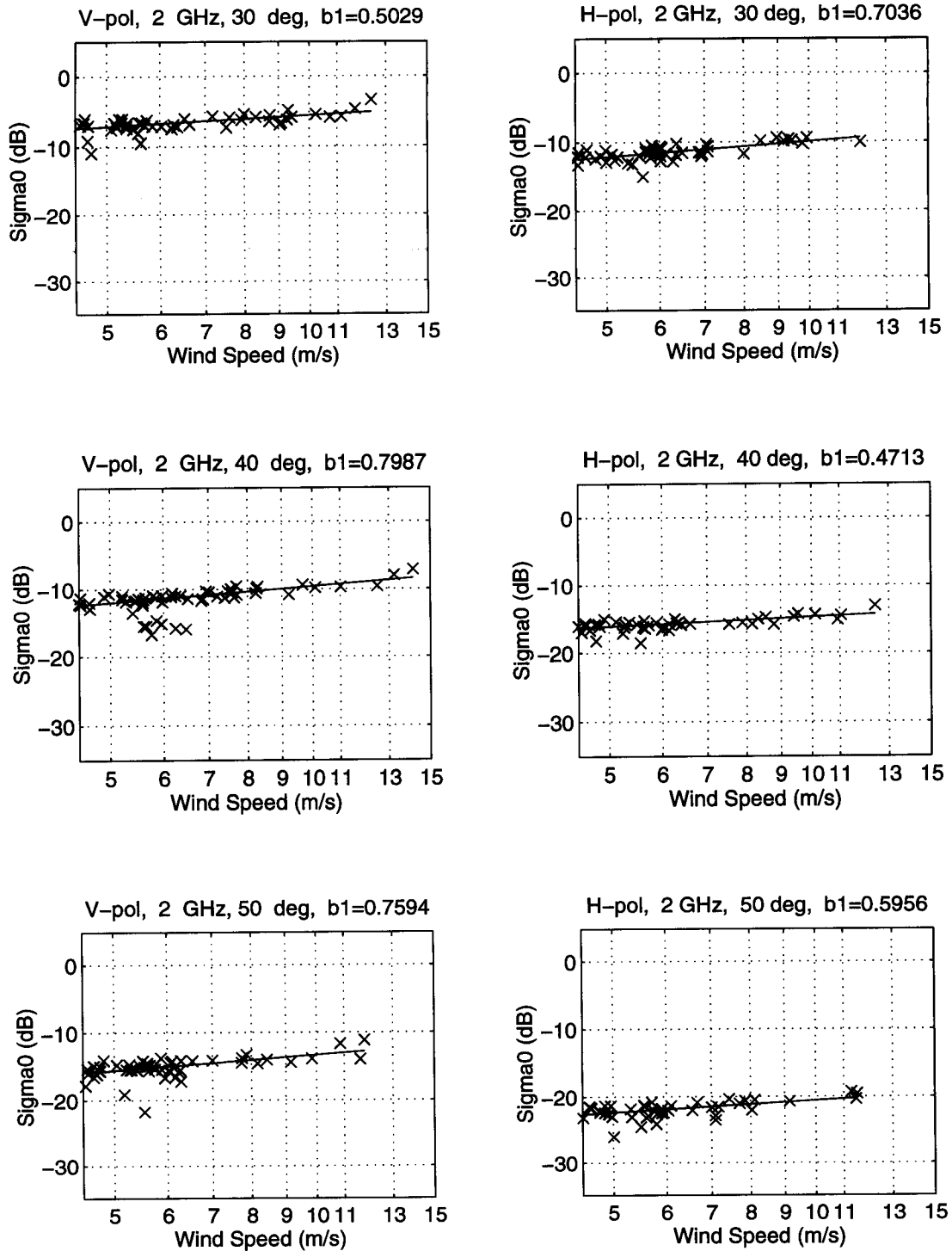
Figure A.1: σ^o vs U(m/s) at 2.0 GHz downwind
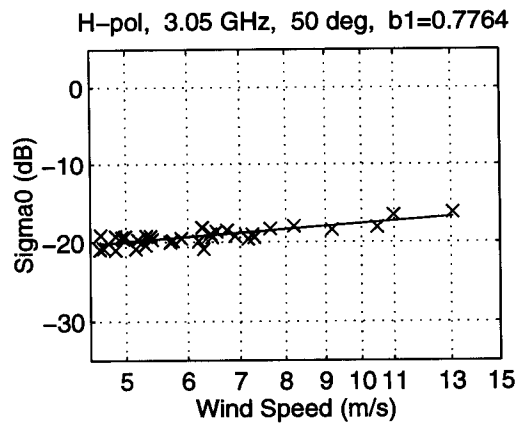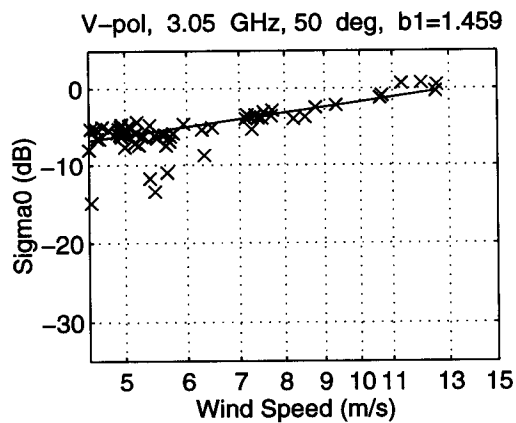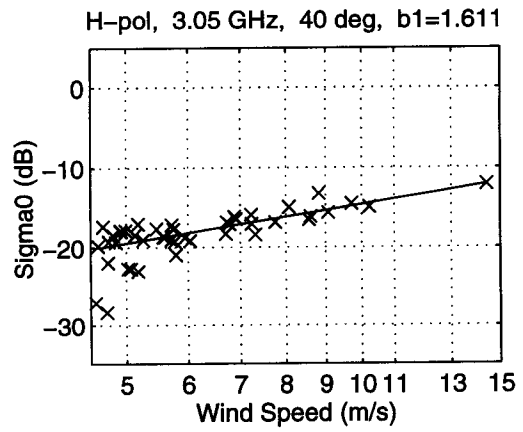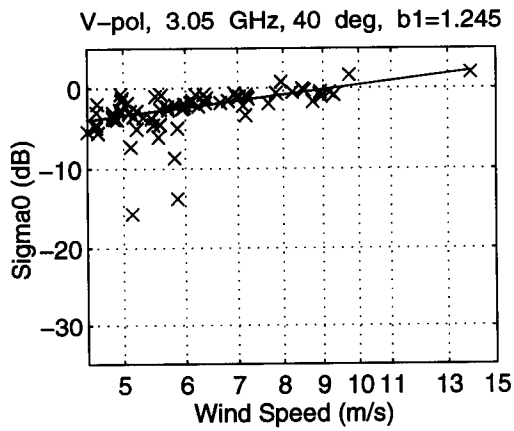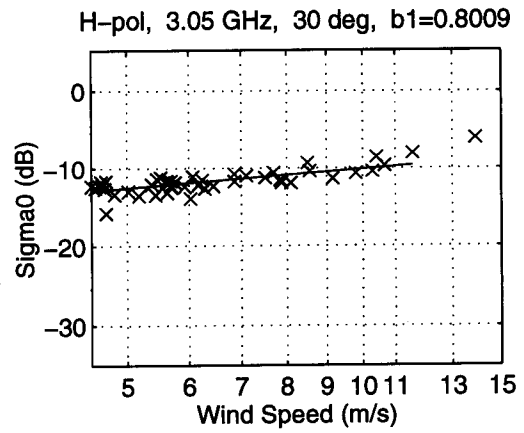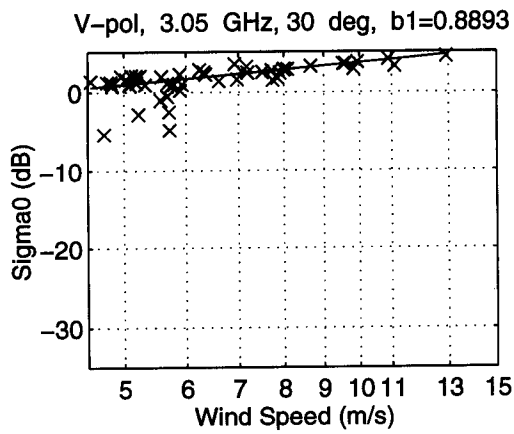
Figure A.2: σ^o vs U(m/s) at 3.05 GHz downwind
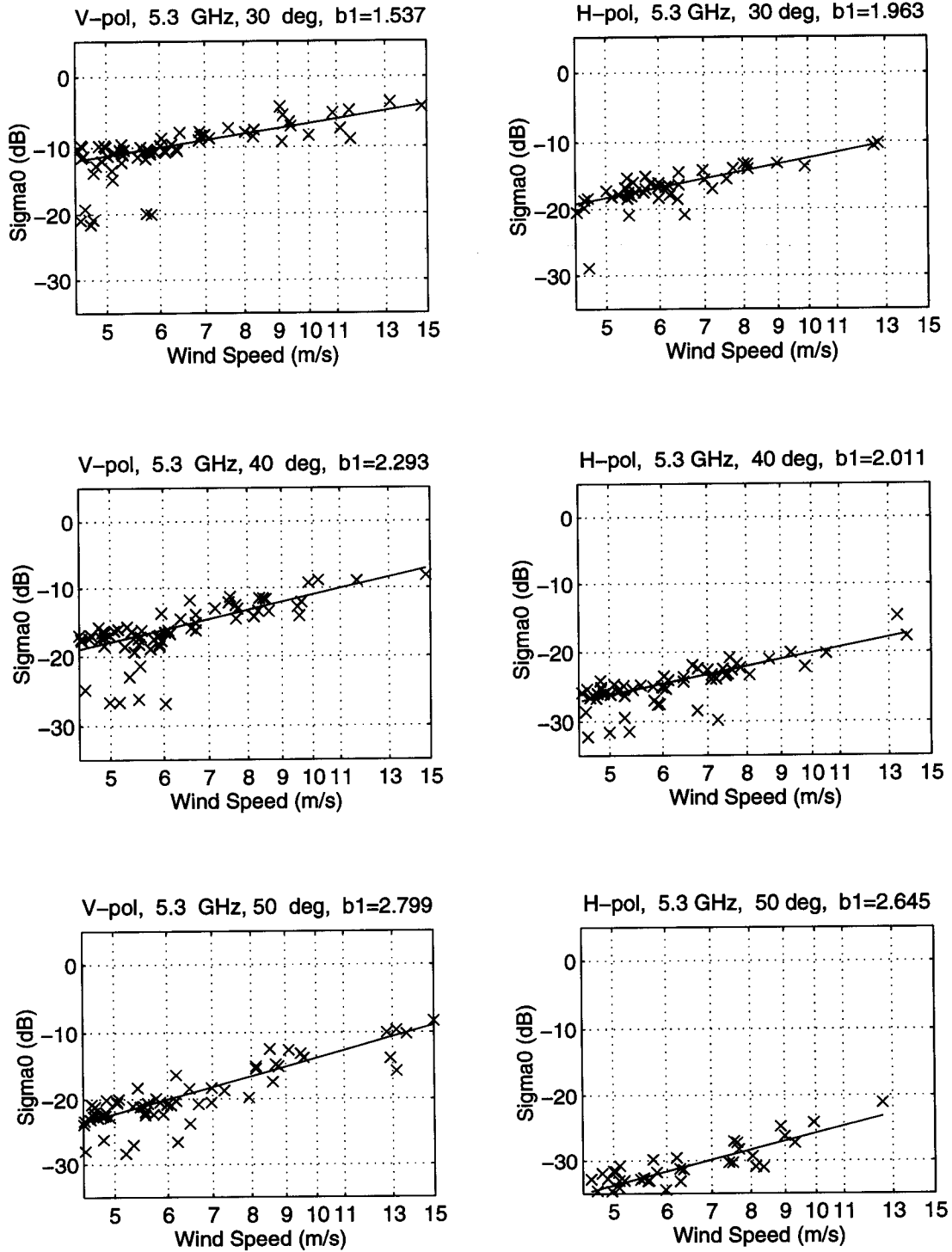
Figure A.3: σ^o vs U(m/s) at 5.30 GHz downwind
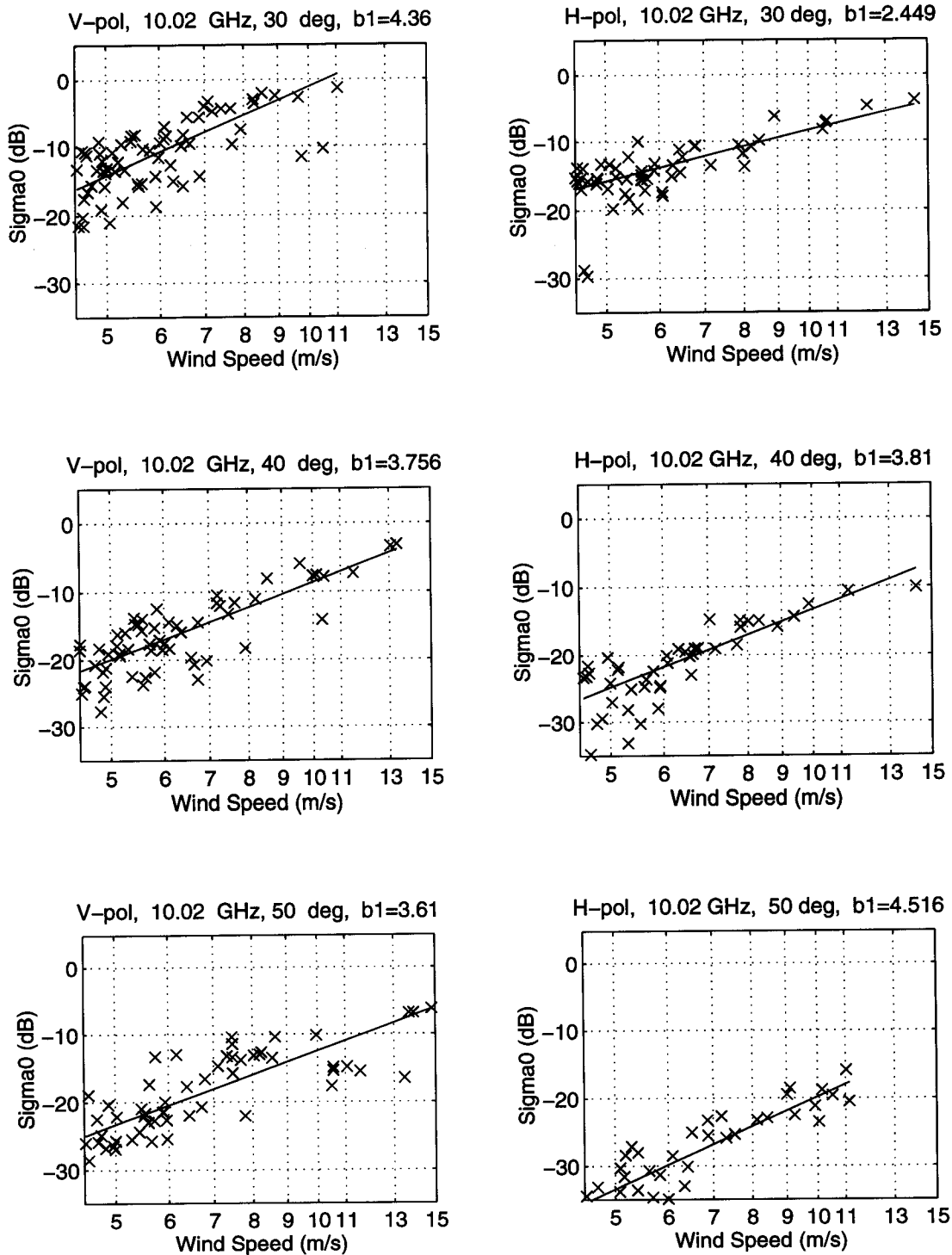
Figure A.4: σ^o vs U(m/s) at 10.02 GHz downwind
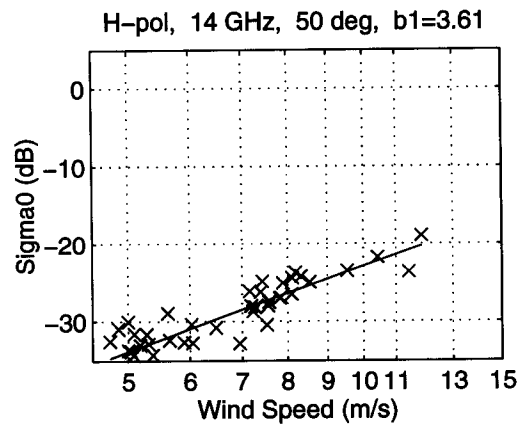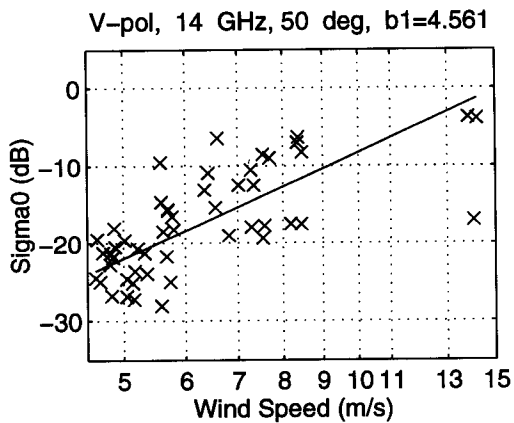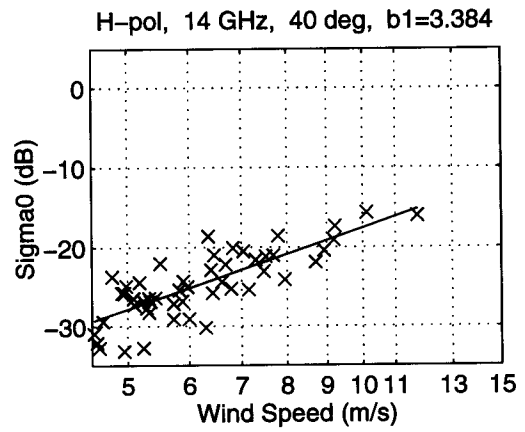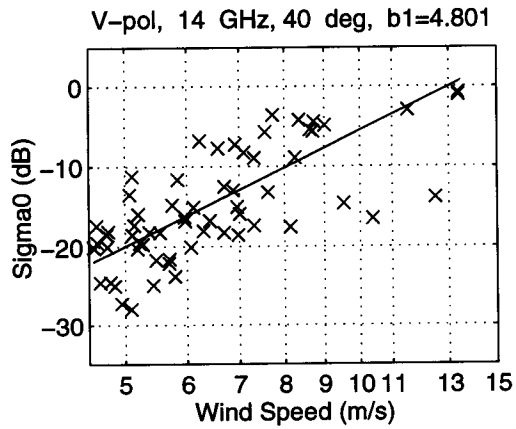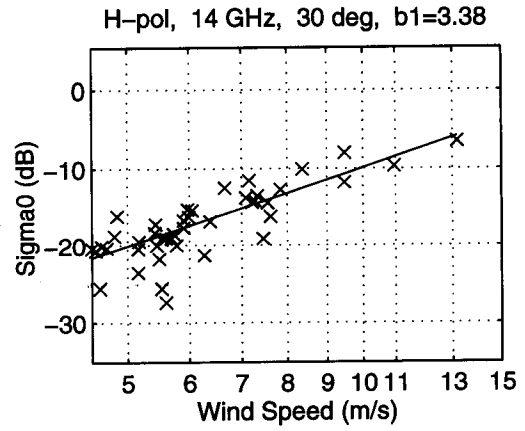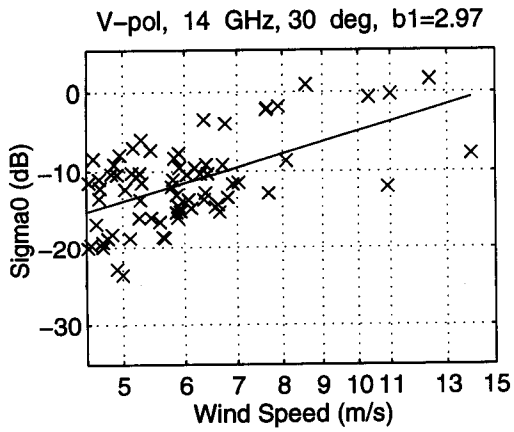
Figure A.5: σ^o vs U(m/s) at 14.00 GHz downwind
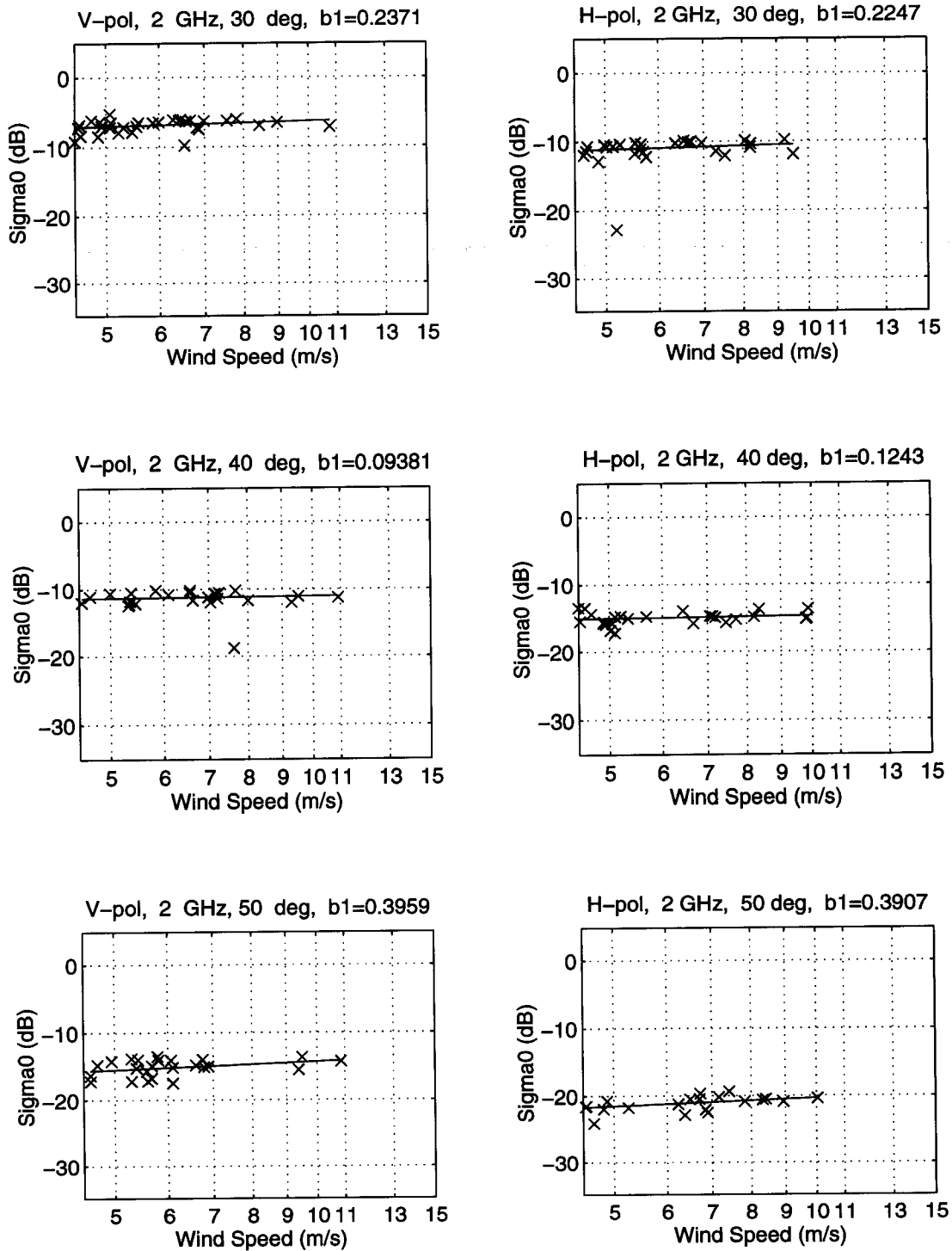
Figure A.6: σ^o vs U(m/s) at 2.00 GHz upwind
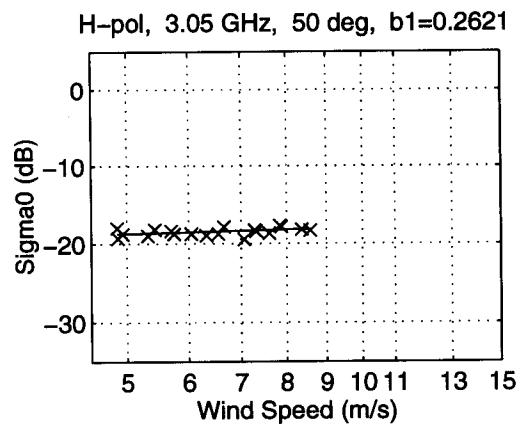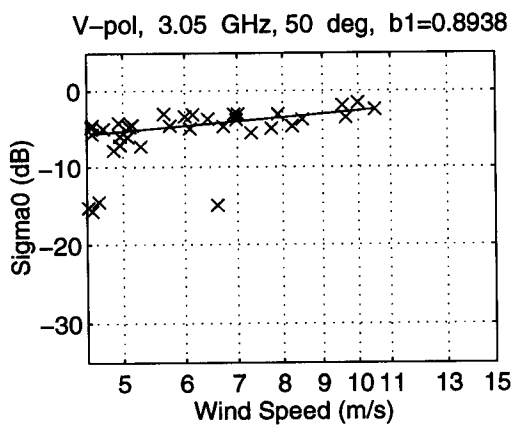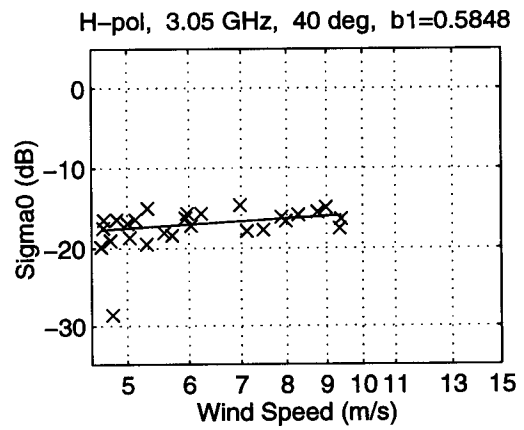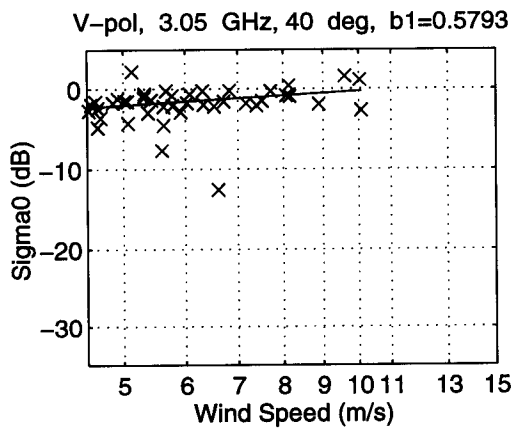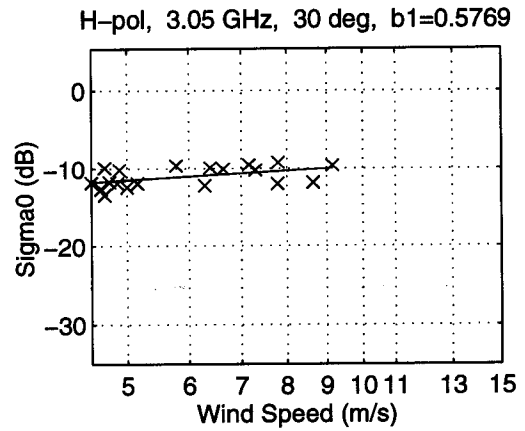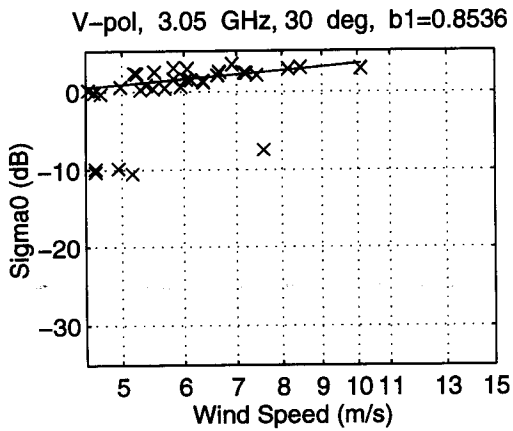
Figure A.7: σ^o vs U(m/s) at 3.05 GHz upwind
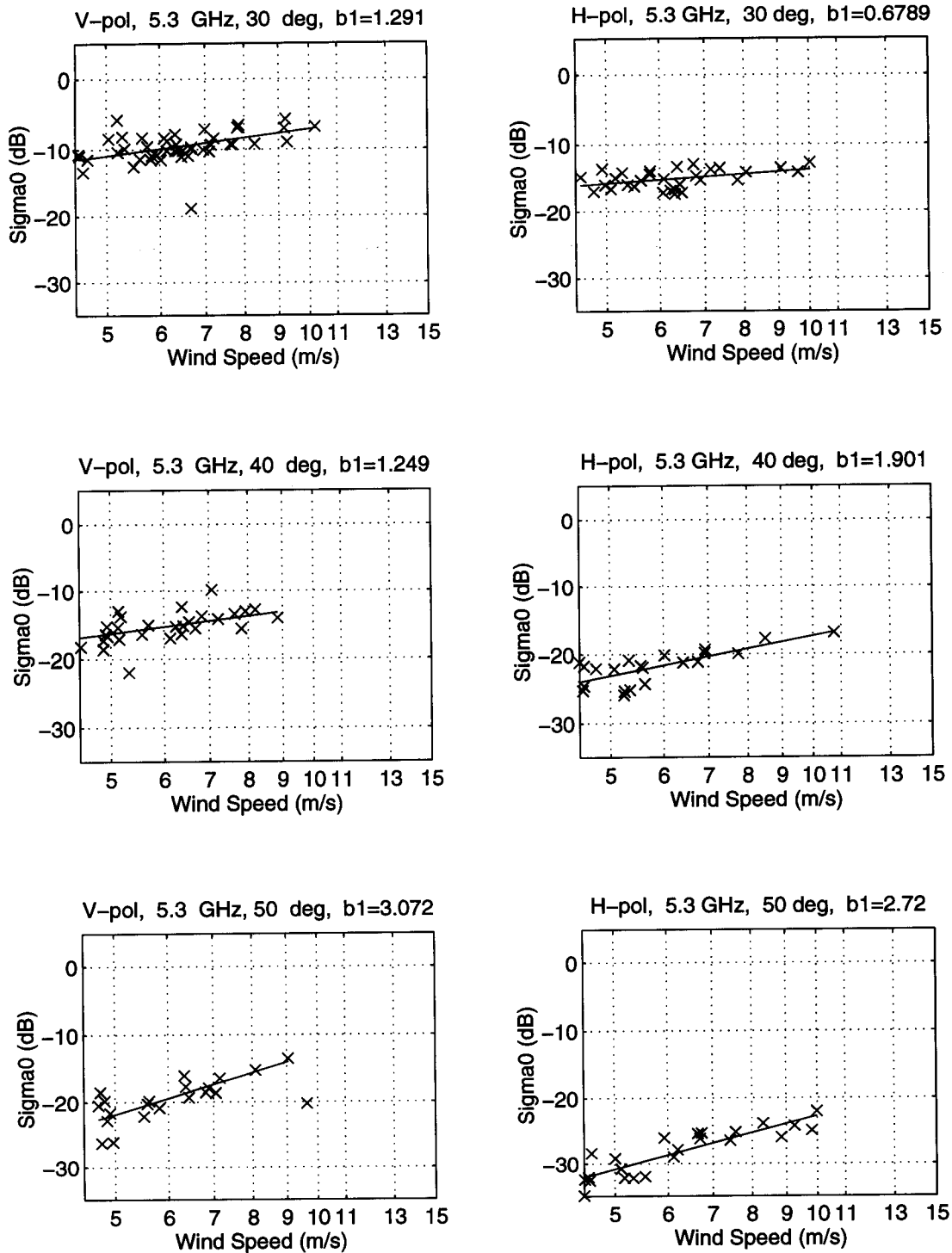
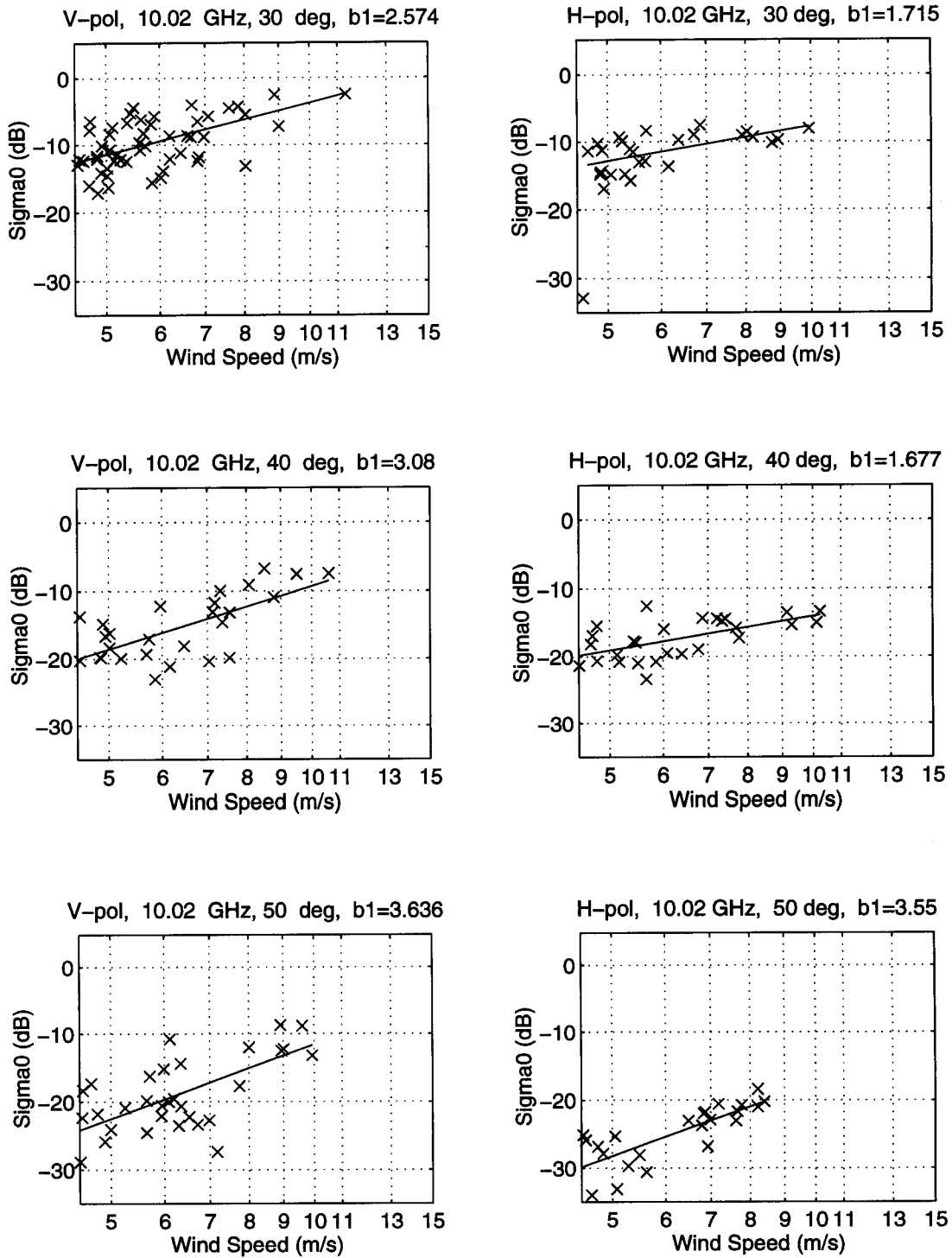Figure A.8: σ^o vs U(m/s) at 5.30 GHz upwind

Figure A.9: σ^o vs U(m/s) at 10.02 GHz upwind

Figure A.10: σ^o vs U(m/s) at 14.00 GHz upwind